ÉCOLE POLYTECHNIQUE
FÉDÉRALE DE LAUSANNE

Atomic Scale Observations of Large Organic Molecules at Metal Surfaces : Bonding, Ordering and Supramolecular Self-Assembly

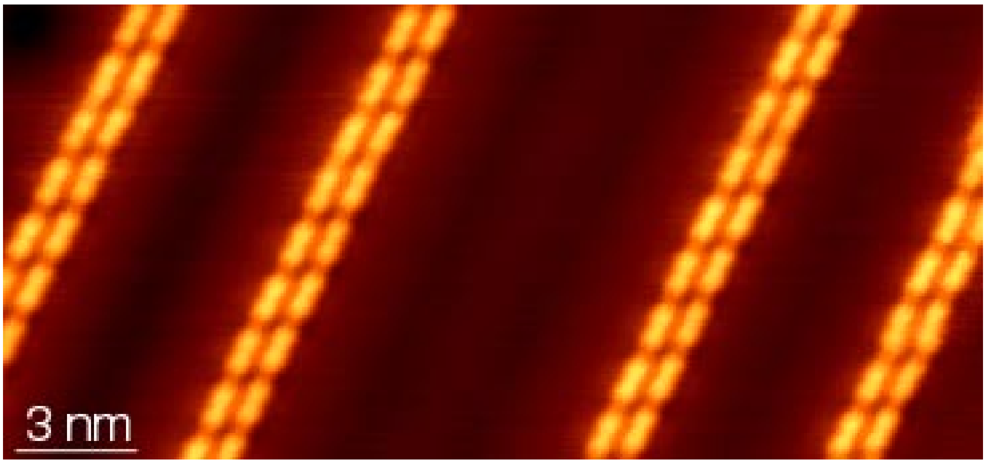

THÈSE N° 2180 (2000)

PRESENTÉE AU DÉPARTEMENT DE PHYSIQUE

ÉCOLE POLYTECHNQIE FÉDÉRALE DE LAUSANNE

POUR L´OBTENTION DU GRADE DE DOCTEUR ÈS SCIENCES

PAR

Jens WECKESSER

Version abrégée

La liaison, l'ordre et la mobilité de grandes molécules organiques sur des surfaces métalliques bien définies sont étudiés à l'échelle atomique. Leur diffusion de surface est caractérisée de manière directe pour la première fois. Un objectif majeur est l'investigation systématique de l'auto-organisation moléculaire sur des surfaces, qui est gouvernée par l'équilibre subtile entre les interactions intermoléculaires et molécule-surface. Cette dernière peut être ajustée par le choix approprié du matériel et de la symétrie du substrat, grâce auxquels une grande variété de structures supramoléculaires peuvent évoluer. Toutes les structures présentées dans cette thèse sont préparées par croissance épitaxiale en jet moléculaire organique et caractérisées *in situ* par microscopie à effet tunnel.

La partie principale se concentre sur deux espèces moléculaires, i.e. 4-[*trans*-2-(pyrid-4-yl-vinyl)]benzoic acid (PVBA) et 4-[(pyrid-4-yl-ethynyl)]benzoic acid (PEBA). Chacune de ces molécules est de forme allongée et planaire, et leur groupe terminal identique est désigné spécifiquement pour former des liaisons hydrogène fortes. L'étude de molécules de la même famille sur différentes surfaces cristallines métalliques met en évidence comment la nature et la symétrie du substrat, ainsi que les effets stériques influencent la liaison et l'ordre.

Sur le Pd(110), l'adsorption et la croissance de PVBA sont dominées par de fortes liaisons π avec le substrat. Les molécules s'adsorbent à plat avec deux orientations distinctes, conférant aux sous-unités moléculaires une coordination optimale avec les atomes de Pd de la surface. La diffusion de surface des molécules est strictement unidimensionnelle le long des directions $[1\bar{1}0]$ et obéit à une loi d'Arrhenius avec une barrière d'activation de (0.83 ± 0.03) eV et une fréquence d'essai de $10^{(10.3\pm0.4)}$ s^{-1}.

Pour le système PVBA/Ag(111), les interactions intermoléculaires et molécule-substrat sont bien équilibrées. A basse température (125 K), les molécules sont mobiles et des interactions attractives entre les groupes terminaux moléculaires stabilisent des réseaux moléculaires ramifiés. Ceci peut être rationalisé en termes d'agrégation par diffusion limitée d'espèces de forme allongée sujettes à des interactions anisotropiques. A l'équilibre, un réseau d'échelette supramoléculaire unidimensionnel a pu être fabriqué, composé de paires de chaînes répulsives. Des images STM à haute résolution ont permis de mettre en évidence le positionnement de molécules individuelles induit par les liaisons hydrogène. Cette nanostructure moléculaire auto-organisée est enantiomorphique, i.e. il existe deux espèces miroir. Des simulations en dynamique moléculaire ont été effectuées pour étudier la chiralité des paires de chaînes associées aux deux espèces chirales existantes pour le PVBA adsorbé sur une surface. Toutes les paires de chaînes présentent une même chiralité sur de larges domaines. Un scénario est proposé, dans lequel la chiralité prolifère pendant le processus de croissance.

La même nanostructure unidimensionnelle que sur l'Ag(111) évolue sur l'Au(111), démontrant le couplage intrinsèque du PVBA. A cause de la réactivité locale prononcée des atomes d'or aux coudes de la reconstruction de surface, un réseau d'échelette supramoléculaire unidimensionnel quasi équidistant a pu être fabriqué avec une périodicité dictée par la reconstruction de l'Au(111). Sur le Cu(111), de fortes interactions entre le groupe d'acide carboxylique et le substrat sont présentes; à basse température, des molécules isolées, dans une configuration verticale, coexistent avec des îles dendritiques, où prévalent différentes géométries d'adsorption. Le rapport avec les adatomes du substrat conduit à plus haute température à des liaisons plates qui permettent de maximiser simultanément les interaction π avec le substrat et la liaison cuivre-carboxylate.

La différence subtile entre les géométries du PEBA et du PVBA conduit à des changements drastiques dans l'auto-organisation sur l'Au(111). Là encore, des rangées moléculaires sont formées par des liaisons hydrogène, mais elles sont liées de manière répétée, et des îles deux dimensionnelles évoluent. Au contraire du système PVBA/Ag(111), où des molécules chirales construisent des structures supramoléculaires enantiomorphiques à cause de la séparation entre espèces chirales, le compactage de molécules non-chirales conduit à des structures enantiomorphiques pour le PEBA sur l'Ag(111).

Finalement, nous discutons la liaison, la mobilité et l'ordre de la molécule C_{60} sur le Pd(110). Sur les images STM, deux espèces de C_{60} différemment liées sont distinguables, l'une est métastable et sa mobilité a pu être suivie. Elle est irréversiblement transformée en l'autre espèce par activation thermique. Trois couches hautement ordonnées de rangées alternées avec une modulation en hauteur très marquée sont observées, et, en combinaison avec des mesures de diffraction d'électrons lents (LEED), leurs cellules élémentaires sont déterminées. La structure de la monocouche saturée est compacte dense et identifiée comme étant une structure $\left(\begin{smallmatrix} 7 & -1 \\ \mp 2 & \pm 5 \end{smallmatrix}\right)$. Une structure rectangulaire (4×5) apparaît après la désorption partielle de C_{60}. A des taux de recouvrement plus faibles, l'arrangement hexagonal de la structure volumique du C_{60} prévaut uniquement localement et une structure rectangulaire (4×8) est formée. Une analyse en diffraction de photoélectrons X (XPD) révèle que toutes les molécules C_{60} dans les phases hautement ordonnées sont orientées de manière identique, faisant face à la surface avec une liaison 5-6. Leurs différentes hauteurs en STM sont attribuées à la reconstruction de la surface de Pd.

Abstract

The bonding, ordering and mobility of large organic molecules on well-defined metal surfaces are studied at the atomic scale. Their surface diffusion is for the first time directly characterized. A major objective is the systematic investigation of molecular self-assembly at surfaces, which is governed by the subtle balance between intermolecular and molecule-surface interactions. The latter can be tuned via the appropriate choice of substrate material and symmetry, whereupon a variety of supramolecular structures evolve. All structures presented in this thesis are prepared by organic molecular beam epitaxy (OMBE) and characterized *in situ* by scanning tunneling microscopy (STM).

The main part deals with two related molecular species, i.e., 4-[*trans*-2-(pyrid-4-yl-vinyl)]benzoic acid (PVBA) and 4-[(pyrid-4-yl-ethynyl)]benzoic acid (PEBA). Both rodlike molecules are planar and their identical endgroups are specifically designed to form strong hydrogen-bonds. The study of related molecules on different single crystal metal surfaces elucidates how nature and symmetry of the substrate and steric effects influence the bonding and ordering.

On Pd(110) the adsorption and growth of PVBA are dominated by strong π-bonding to the substrate. The molecules bind flat in two distinct orientations giving optimal coordination of the molecular subunits with the Pd surface atoms. The molecules' surface diffusion is strictly one-dimensional along the close-packed $[1\bar{1}0]$-direction and obeys an Arrhenius law with an activation barrier of (0.83 ± 0.03) eV and an attempt frequency of $10^{(10.3\pm0.4)}$ s^{-1}.

For the PVBA/Ag(111) system intermolecular interactions and molecule-substrate interactions are well balanced. At low temperature (125 K) molecules are mobile and attractive interactions between the molecular endgroups stabilize ramified molecular networks. This can be rationalized as diffusion limited aggregation of rodlike species subject to anisotropic interactions. At equilibrium a one-dimensional supramolecular nanograting consisting of repelling molecular twin chains could be fabricated. High resolution STM images elucidate the hydrogen bond mediated positioning of individual molecules. This self-assembled supramolecular nanostructure is enantiomorphic, i.e., two mirror species exist. MD-simulations are performed to investigate the chirality of twin chains associated with the two chiral species existing for PVBA adsorbed on a surface. In large domains all twin chains exhibit the same chirality. A scenario is proposed in which chirality proliferates during the growth process.

On Au(111) the same one-dimensional nanostructure as on Ag(111) evolves demonstrating the intrinsic coupling of PVBA. Due to the locally increased reactivity of Au atoms at the elbows of the surface reconstruction a nearly equidistant one-dimensional supramolecular nanograting with a periodicity dictated by the Au(111) chevron pattern can be fabricated. On Cu(111) strong interactions between the carboxylic acid group and the substrate are operative, at low temperatures isolated upright standing molecules coexist with dendritic islands where different adsorption geometries prevail. The interplay with substrate adatoms at higher temperatures leads to flat bonding which allows the *simultaneous* maximization of directed π-interactions to the substrate and copper-carboxylate bonding.

The subtle difference in geometry between PEBA and PVBA results in drastic changes in the self-assembly on Ag(111). Again molecular rows are formed by head-to-tail hydrogen-bonding, but they are repeatedly linked and two-dimensional islands evolve. In contrast to the PVBA/Ag(111) system where *chiral* molecules built enantiomorphic supramolecular structures due to *separation* of chiral species, the *packing* of *achiral* molecules causes enantiomorphic structures for PEBA on Ag(111).

Finally we address the bonding, mobility and ordering of the ball-shaped C_{60} molecule on Pd(110). In STM images two differently bound C_{60} species are distinguished; one is metastable and the mobility could be monitored. It is irreversibly converted into the other species upon thermal activation. Three highly ordered overlayers consisting of alternating rows with a strong height modulation are found and in combination with low energy electron diffraction (LEED) their unit cells are determined. The saturated monolayer structure is close-packed and identified as a $\left(\begin{smallmatrix} 7 & -1 \\ \mp 2 & \pm 5 \end{smallmatrix}\right)$-structure. A rectangular (4×5)-structure evolves after partial desorption of C_{60}. At lower coverage the hexagonal order of C_{60} bulk structure prevails only locally and a rectangular (4×8)-structure is formed. An x-ray photoelectron diffraction (XPD) analysis reveals that all C_{60} molecules in the highly ordered phases are identically oriented, facing with a 5-6 bond to the surface. Their different height in STM is attributed to Pd surface reconstruction.

Contents

Abbreviations and Common Symbols

AFM	Atomic Force Microscopy
DFT	Density Functional Theory
FWHM	Full Width at Half Maximum
HAS	Helium Atom Scattering
HOMO	Highest Occupied Molecular Orbital
(L)DOS	(Local) Density Of States
LEED	Low Energy Electron Diffraction
LITD	Laser-Induced Thermal Desorption
LUMO	Lowest Unoccupied Molecular Orbital
MC	Monte Carlo
MD	Molecular Dynamic
ML	Monolayer
NMR	Nuclear Magnetic Resonance
NN	Nearest Neighbor
OMBE	Organic Molecular Beam Epitaxy
PEBA	4-[(pyrid-4-yl-ethynyl)]benzoic acid
PVBA	4-[$trans$-2-(pyrid-4-yl-vinyl)]benzoic acid
SSC	Single-Scattering Cluster
STIS	Scanning Tunneling Inelastic Spectroscopy
STM	Scanning Tunneling Microscopy
UHV	Ultra-High Vacuum
XPD	X-ray Photoelectron Diffraction
XPS	X-ray Photoelectron Spectroscopy

a	surface lattice constant
a_0	Bohr radius, $a_0 = 0.529$ Å
D_0	preexponential factor for tracer diffusion
e	protonic charge, $e = 1.6 \cdot 10^{-19}$ C
E	energy with respect to the Fermi energy
E_b	binding energy of adsorbates
E_F	Fermi energy
E_m	energy barrier for surface migration
$f(E,T)$	Fermi-Dirac distribution
fcc	face cubic centered
hcp	hexagonal close-packed
I	tunneling current
i	tunneling current per energy unit
m_e	free electron mass, $m_e = 9.11 \cdot 10^{-31}$ kg
s	tip-sample distance
T	temperature
V	electric potential of sample with respect to tip
W	work function
δ	delta function
θ	surface coverage
$\hbar$	Planck constant, $\hbar = \frac{h}{2\pi} = 1.05 \cdot 10^{-34}$ Js
ν_0	attempt frequency
ν_s	hopping rate
π	pi, $\pi = 3.14$
ρ	electronic density of states
2D	Two-Dimensional

Chapter 1

Introduction

Dr Neal Lane, Advisor for Science and Technology to Bill Clinton, stated at a Congressional hearing in April 1998, "If I were asked for an area of science and engineering that will most likely produce the breakthroughs of tomorrow, I would point to nanoscale science and engineering."

Chemists control the arrangement of small numbers of atoms within molecules, that is, to synthesize molecular species at the nanometer scale. This has led to revolutions in drug design, synthetic materials and many other areas. Over the last several decades, photolithographic patterning (the primary manufacturing process of the semiconductor industry) of matter on the micron length scale has led to the revolution in microelectronics. With nanotechnology, it is just becoming possible to bridge the gap between the atom/molecular length scale and microtechnology, and to control matter at every important length scale, enabling tremendous progress in future materials design.

The applications of nanostructured materials are widespread ranging from novel catalysts with extremely high selectivity to medical implants adapted to a living organism.

A primary motivation for nanotechnology results from the desire to continue Moore's law which states that the feature sizes of microelectronic devices shrink by half every four years. Today the smallest features in modern microprocessors are about 200 nanometers and at this rate, feature sizes would be less than 10 nanometers by 2020 and atomic scale by 2035. In fact, Moore's law will halt before then, about 2012, because of quantum mechanical effects that will prevent us from continuing to improve performance of logic devices simply by shrinking them [1, 2]. At that point, new information processing methodologies will be required if we are to continue to advance our ability to compute.

Currently several new strategies for the envisioned post silicon era are discussed. One extremely promising route is molecular electronics [3], for which molecules that are quantum electronic devices are designed and synthesized using the batch processes of chemistry and then assembled into useful circuits through the processes of self-organization and self-alignment. A molecular rectifier has been proposed as early as 1974 [4] and single-molecule transistors have already been realized [5,6]. For connecting such molecular devices electrical conductance through single molecules, especially carbon nanotubes is currently investigated [7,8].

A major question to be tackled is the controlled arrangement of the molecular building blocks. Fascinating progress has been achieved in the last decades in supramolecular chemistry [9–12]. The basic concept in supramolecular chemistry is to create arrangements from molecular building blocks which are interconnected by chemical bonds, predominantly of noncovalent character. This idea originates from living organisms : Natural supermolecules are abundant in biological systems, where their proper functioning is of crucial importance for life. Due to its high selectivity and directionality, hydrogen bonding proved to be particularly important in this respect [13]. One of the most important concepts to obtain the corresponding molecular architectures and nanostructures is molecular self-assembly, i.e., the spontaneous association of molecules under equilibrium conditions into stable, structurally well-defined aggregates joined by noncovalent bonds [14–18]. The application of this methodology has been demonstrated so far mostly indirectly for systems in solution, where nanostructures with amazing complexity were reported, and for molecular crystals [15,17–22].

Molecular self-assembly *at surfaces* is governed by the subtle balance between intermolecular and molecule-surface interactions which can be tuned via the appropriate choice of substrate material and symmetry. Promising achievements have been reported in this field [23–26].

Upon adsorption on a substrate, the molecules experience the potential energy surface of the substrate, which makes specific adsorption geometries energetically favorable. The ease, with which these sites can be changed by either translational or rotational processes, i.e., the surface mobility, is a key parameter for the arrangement of molecules at surfaces. Similarly important is the strength and nature of the intermolecular interactions which compete with the molecule-substrate interactions. As a third parameter, the magnitude of the thermal energy governs the level of ordering which can be achieved. The balance of these factors controls molecular self-assembly at surfaces.

With the invention of the scanning tunneling microscope (STM) in the beginning of the eighties the direct elucidation of surface processes at the atomic scale became possible. It provides unique information on adsorbed molecular species and molecular phenomena at surfaces [27] and is an excellent technique for the study of epitaxial growth on conducting substrates [28]. Most of the studies performed so far have concentrated

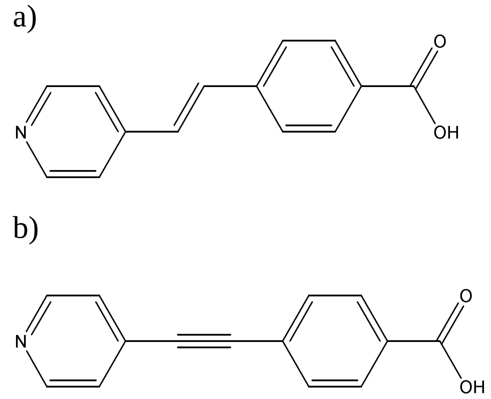

Figure 1.1: Molecular structure of **(a)** 4-[*trans*-2-(pyrid-4-yl-vinyl)]benzoic acid (PVBA) and **(b)** 4-[(pyrid-4-yl-ethynyl)]benzoic acid (PEBA). The planar and rigid molecules comprise a benzoic acid moiety as head and a pyridyl group as tail. They were conceived for self-assembly through head-to-tail hydrogen bonding.

on detailed observations in epitaxy of metal or semiconductor atoms. Among the first *organic molecules* studied by STM was benzene [29] and copper-phthalocyanine [30, 31] and in several recent studies the direct observation of processes in organic molecular beam epitaxy (OMBE) has been reported [32–37]. Large organic molecules are *the* basic elements in the field of molecular electronics and their behavior at surfaces and interfaces is thus of high current interest [3].

A major part of this thesis is devoted to the investigation of two organic molecules, namely 4-[*trans*-2-(pyrid-4-yl-vinyl)]benzoic acid (PVBA) and 4-[(pyrid-4-yl-ethynyl)]benzoic acid (PEBA) on different single crystal metal surfaces. In Fig. 1.1 their molecular structure is represented.

PVBA and PEBA are specifically designed for nonlinear optics applications and organic molecular beam epitaxy (OMBE). The crystal structure is stabilized by head-to-tail hydrogen bonding and this configuration results in macroscopic hyperpolarizability. Both molecules consist of the same molecular endgroups, a benzoic acid moiety as head and a pyridyl group as tail. They are linked via a C=C bridge and a C≡C bridge, respectively [38, 39]. The molecules are almost planar and the phenylene and pyridyl rings are aligned parallel. As a consequence of the angled geometry of PVBA two chiral species exist for the adsorbed molecule. In contrast the straight geometry of PEBA does not induce chirality in 2D (neglecting the asymmetry of the carboxylic acid group). The molecular endgroups are especially designed to form strong hydrogen bonds and as a consequence, substantial attractive interactions between the molecules adsorbed on a surface might be expected. On the other hand, attractive lateral dipole interactions due to the inhomogeneous in-plane charge distribution within the molecule might interfere.

Adsorption on different single crystal metal surfaces is investigated, ranging from the transition metal Pd(110) surface, the close-packed Cu(111) to the noble metal Ag(111) and Au(111) surfaces.

Our findings suggest that self-assembly of properly designed molecules via noncovalent bonding opens novel avenues for the positioning of nanometer functional units in supramolecular architectures at surfaces by organic molecular beam epitaxy. It is believed that this approach will be valuable for the future fabrication of nanoscale devices and supramolecular engineering.

Subsequently, the adsorption of C_{60} on Pd(110) is presented. Promising and appealing technological applications [40] stimulate the investigation of the properties of this fascinating new carbon-based material. In the beginning the main focus was on the geometric and electronic structure of pure and alkali metal doped C_{60} bulk samples [41]. Today, the study of interactions between fullerenes and surfaces has developed into a major area of research on this third allotropic form of carbon. Two aspects motivate this interest. Firstly, from a technological point of view, the substrate-induced modification of the electronic and structural properties of C_{60} layers is an important question to be addressed if this new material is to find an application in the electronics industry. Secondly, the variety of both bond strength and bond character observed in the interaction between C_{60} and a substrate is really exceptional.

The present work is organized as follows:

Chapter 2 gives an introduction to the experimental methods employed, i.e., scanning tunneling microscopy (STM) and x-ray photoelectron diffraction (XPD). The experimental set-up and the sample preparation are briefly described.

The PVBA/Pd(110) system presented in Chapter 3 is an example for the ordering and diffusion of a large organic molecule on an anisotropic substrate in the presence of strong adsorbate-substrate interactions. We report the first direct study of the surface diffusion of a large organic molecule chemisorbed on a metal surface. The data demonstrate that with the present system the adsorbate-substrate interactions completely determine the film growth and bonding geometry, which remains unaffected by intermolecular interactions.

For PVBA on Ag(111) described in Chapter 4 intermolecular interactions and molecule-substrate interactions are well balanced. A one-dimensional supramolecular nanograting consisting of molecular twin chains could be fabricated. High resolution STM images illustrate that molecules within a row are pointing in the same direction allowing the formation of head-to-tail hydrogen bonds. The PVBA rows within the twin chains are shifted with respect to each other and thus the supramolecular assembly is enantiomorphic. MD-simulations reveal that the chirality of twin chains is associated with the two chiral species present for PVBA adsorbed on a surface. In large domains all twin chains are of the same chirality. A scenario is proposed in which chirality proliferates during the growth process.

In Chapter 5 the adsorption of PVBA on Au(111) and Cu(111) is described. On the reconstructed Au(111) surface the same twin chain feature as on Ag(111) evolves. The periodicity is dictated by the chevron pattern, i.e., a highly regular nanograting is fabricated. On Cu(111) strong interactions of the carboxylic acid group to the substrate are operative and at low temperatures isolated upright standing molecules coexist with π-bonded molecules in dendritic islands. The availability of substrate adatoms at higher temperatures leads to a flat adsorption geometry which allows the *simultaneous* maximization of directed π-interactions to the substrate and copper-carboxylate bonding.

The ordering of PEBA on Ag(111) presented in Chapter 6 demonstrates the influence of steric effects for the growth in two dimensions. The subtle difference in geometry between PEBA and PVBA results in drastic changes in the self-assembly. Again, molecular rows are formed by head-to-tail hydrogen-bonding, but they are repeatedly linked and two dimensional islands evolve. In contrast to the PVBA/Ag(111) system where *chiral* molecules built enantiomorphic supramolecular structures due to *separation* of chiral species, the *packing* of *achiral* molecules causes enantiomorphic structures for PEBA on Ag(111).

Finally, in Chapter 7 a combined STM, LEED and XPD study of C_{60} on Pd(110) is presented. The mobility of single C_{60} molecules is directly investigated by variable-temperature STM. Two differently bound C_{60} species are distinguished; one is metastable and is irreversibly converted into the other upon thermal activation. The complementary information provided by the different techniques allows for a detailed understanding of the ordering at the local and mesoscopic scale. Three highly ordered structures consisting of alternating molecular rows with a strong height modulation are found, in combination with LEED their real space structures are determined. An x-ray photoelectron diffraction (XPD) analysis reveals that all C_{60} molecules in the highly ordered phases are identically oriented. Their different height in STM is attributed to Pd surface reconstruction.

Chapter 2

Experimental

We present an introduction to the principles and theory of the experimental methods, namely scanning tunneling microscopy (STM) and x-ray photoelectron diffraction (XPD). The experimental set-ups and sample preparation employed during the studies are discussed in Section 2.2 and Section 2.3, respectively.

2.1 Experimental Methods

Scanning Tunneling Microscopy

Scanning tunneling microscopy [42] was invented by Binnig and Rohrer in 1982 [43, 44]. Figure 2.1(a) shows the schematic of an STM. A tip, normally a sharpened metallic wire, is brought close to the conducting surface of a sample. The lateral tip position (x and y axis), as well as the tip-sample distance s are controlled with picometer precision by means of voltage signals applied to piezo-electric materials. If the tip is brought close enough to the sample that the wave functions of the conduction electrons of tip and

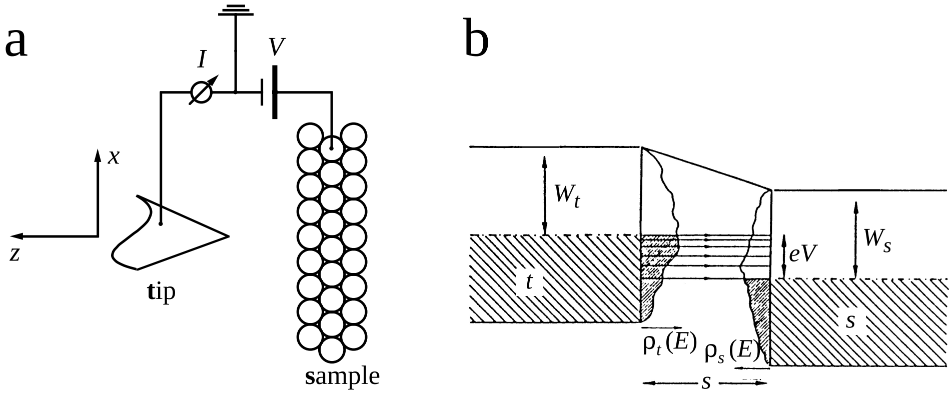

Figure 2.1: (a) Schematic of an STM. **(b)** Corresponding potential energy diagram.

sample begin to overlap substantially, a measurable tunneling current I flows between the biased sample (potential V with respect to ground) and the virtually grounded tip (Fig. 2.1(b)). The tip-sample distance in typical tunneling experiments is about 5–10 Å. Since the tunneling current depends exponentially on the tip-sample distance, it mainly flows through the few atoms at the very apex of the tip. Thus the tunneling current is highly localized, leading to the atomic-scale resolution of STM. In the case of a positively biased sample (as in Fig. 2.1(b)) the net current comes from electrons tunneling from occupied states in the tip to unoccupied states of the sample. The current per energy unit, i, is represented by the density of horizontal arrows in Fig. 2.1(b). As can be seen i decreases with decreasing energy since the energetically lower lying states decay steeper in the vacuum barrier region. Whereas it is intuitively clear from Fig. 2.1(b) that the tunneling current will depend on the density of occupied and unoccupied states of tip and sample (ρ_t and ρ_s), respectively, the exact calculation of the tunneling current starting from the electronic structures of tip and sample is a difficult task. It is further complicated by the fact that the atomic structure and the chemical nature of the tip apex is normally not known.

To interpret STM data one may follow the widely used transfer Hamiltonian approximation introduced by Bardeen [45], where the tunneling current is given by [46]:

$$\begin{aligned} I(V) &= 2e \sum_{\mu,\nu} \frac{2\pi}{\hbar} \left|T_{\mu,\nu}\right|^2 \delta(E_\mu - eV - E_\nu) \times \\ & \Big(f(E_\mu - eV, T)\,[1 - f(E_\nu, T)] - f(E_\nu, T)\,[1 - f(E_\mu - eV, T)] \Big) . \end{aligned} \tag{2.1}$$

Here the summation goes over all quantum states μ and ν of the unperturbed sample and tip, respectively, f is the Fermi–Dirac distribution function [1], T is the temperature and $T_{\mu,\nu}$ is given by

$$T_{\mu,\nu} = -\frac{\hbar^2}{2m_e} \int_{\Sigma} d\mathbf{S} (\Psi_\nu^* \nabla \Psi_\mu - \Psi_\mu \nabla \Psi_\nu^*) \,, \tag{2.2}$$

which must be evaluated over a surface Σ within the barrier region and with the wave functions of the unperturbed sample and tip, Ψ_μ and Ψ_ν, respectively. The $T_{\mu,\nu}$ matrix elements depend roughly exponentially on the barrier width s.

To get beyond qualitative properties of the tunneling current one has to find good approximations for the matrix elements $T_{\mu,\nu}$. A simple STM theory is the s-wave approximation for tip wave functions introduced by Tersoff and Hamann [47], leading to

---

[1] Energies are given with respect to the Fermi level if not otherwise stated.

the following expression for the tunneling current [48, 49]

$$\begin{aligned} I(V,T,x,y,s) \;\propto\; & \int\limits_{-\infty}^{\infty} dE\, \rho_s(E,x,y)\, \rho_t(E-eV) \times \\ & \mathcal{T}(E,V,s)\,[f(E-eV,T) - f(E,T)]\,, \end{aligned} \tag{2.3}$$

where ρ_t is the density of states (DOS) of the tip, x and y characterize the lateral position on the sample and s the distance between tip and sample measured from a virtual plane passing through the uppermost atoms. ρ_s is the LDOS of the sample in this virtual plane. An often used expression for the tunneling transmission factor $\mathcal{T}(E,V,s)$ reads [49]:

$$\mathcal{T}(E,V,s) = \exp\left(-2s\sqrt{\frac{m_e}{\hbar^2}}\sqrt{W_s + W_t - 2E + eV}\right)\,. \tag{2.4}$$

Here V is the electric potential of the sample with respect to the tip, W_s and W_t are the work functions of sample and tip, respectively (cf. Fig. 2.1).

Although this is a crude simplification, the expressions in Eqs. (2.3) and (2.4) contain the essential and are a good starting point for qualitative and under certain conditions quantitative discussions.

All STM images presented in this thesis are taken in the so-called *constant-current imaging* mode [42]. In constant-current imaging the tunneling current I is compared to a preset current value I_0. The difference signal $\Delta I = I - I_0$ is fed back to the voltage applied to the z-piezo so that the tip-sample distance is adjusted in order to minimize ΔI [50]. The surface is then scanned by the tip and the voltage applied to the z-piezo in order to keep the current constant is recorded. One thus obtains a so-called topograph $z(x,y)|_{I,V}$ which term is misleading because $z(x,y)|_{I,V}$ is rather a surface of constant local density of states (LDOS) of the sample. Thus it reflects the electronic structure and *one has to be careful to interpret $z(x,y)|_{I,V}$ images in terms of surface topography.*

This is apparent in the case of molecules. A well-known counterintuitive example is atomic oxygen chemisorbed on a metal surface, which appears as depression in STM images even if the atom is positioned above the metal surface layer [51]. STM patterns of molecules often show internal structures and details but the interpretation is not straightforward and a priori it is not even evident whether the bumps are located on the positions of atoms or bonds of the adsorbate.

Before the first successful STM experiments with clearly resolved organic molecules were reported [29–31] it appeared questionable whether “insulating” molecules can be imaged by STM at all. As stated above, the tunneling current is proportional to the sample LDOS near the Fermi level E_F within the framework of the s-wave theory of

STM. Most organic molecules have a large energy gap between the highest occupied (HOMO) and the lowest unoccupied (LUMO) molecular orbital(s). If physisorbed on a metal surface, the molecule-related states are usually far away from the substrate Fermi energy. The HOMO- and LUMO- derived resonances are typically several eV below and above E_F, respectively. Therefore, the molecule's contribution on the LDOS near E_F is rather small and at a first glance one might expect organic molecules to be transparent for tunneling electrons at low bias voltage.

The question what renders STM imaging of "insulating" species possible was first quantitatively discussed by Eigler *et al.* for Xe atoms adsorbed on Ni(110) being imaged as bright 1.6 Å high protrusions [52]. The occupied $5p$ orbital lies well below and the unoccupied $6s$ orbital about 4.5 eV above the Fermi level and thus an adsorbed xenon atom makes virtually no contribution to the state density at the Fermi level. The electronic structure of an adsorbed Xe atom was calculated using the atom-on-jellium model introduced by Lang [53,54]. Physisorption causes weak mixing of the Xe $6s$ state with metal substrate states, resulting in strong broadening of the atomic resonance, but the contribution to the density of states at E_F is low and this cannot explain the observed corrugation of Xe atoms in STM. However, the results demonstrated that this resonance extends considerably further out into the vacuum than the bare surface wave functions, which effect makes Xe visible in the STM.

These findings are of general importance for the imaging of molecules adsorbed on metal surfaces. Nonresonant tunneling occurs and the contribution of the adsorbate to the current comes from tails of molecular orbital resonances crossing the Fermi level. These tails are usually rather small at the Fermi level, which explains why contributions from the substrate itself cannot be neglected, despite the rather important difference in height.

To interpret STM images of molecules the electronic structure of the adsorbate-substrate system is calculated, whereby various levels of approximation are used ranging from effective Hückel to first-principles self-consistent methods based mainly on the density functional theory. The tunneling current is frequently associated with the LDOS of the sample at the Fermi energy.

A major drawback of this approach is that the tip and the surface are treated separately, which neglects any interaction between them and is valid only in the limit of large tip–surface distances. Secondly, a severe approximation is made to the structure of the tip apex and any tip dependence of the image is lost. This can be accounted for by regarding p and d states as tip orbitals [55] or by describing the tip apex by a cluster of a small number of atoms [56, 57].

Another approach is the proper description of the interaction between sample and tip with a scattering theory formalism. The influence of tip-sample interactions becomes apparent in the imaging of adsorbed alkali metal atoms. Although they are known to increase the LDOS at E_F, they are frequently transparent in STM data [58]. The basic idea of the scattering theory formalism is to consider the tunnel gap as a two-dimensional defect inserted between two semiinfinite periodic systems. The tunnel event is then viewed as a scattering process. An example is the electron scattering quantum chemical (ESQC) approach developed by Sautet and Joachim [59]. The tunnel junction is modeled by the approach of substrate and tip semiinfinite bulk solids. The adsorbate is chemisorbed on the substrate surface, while the tip apex, attached to the second semiinfinite solid, is modeled by a cluster of 1-15 atoms. Coupling with the tip and substrate electron reservoirs is hence fully taken into account.

This approach has been successfully applied to a multitude of systems, e.g., CO chemisorbed on Pt(111) [60, 61]. Two different molecular shapes are present in STM topographs employing the same imaging conditions. Bocquet *et al.* evidenced that the different shapes are related to two different chemisorption sites of the molecule on the surface [62], i.e., on top and bridge sites, respectively.

Among hydrocarbon molecules, the favorite one for STM imaging and calculations is certainly benzene. One of the earliest experimental images of this molecule, coadsorbed with CO on Rh(111) was obtained by Ohtani *et al.* [29]: The molecule, which is bound at a threefold substrate hollow site as determined by LEED [63], appears as three lobes arranged in a triangle in STM topographs. The lobes are located near the middle of C-C bonds, in between underlying Rh substrate atoms as evidenced by ESQC [64]. Hence the STM image of benzene does not show positions of molecular C atoms but some of the C-C bonds. The shape mainly results from the interaction of the molecule with the threefold surface site. Benzene does not have any electronic state in resonance with the Fermi level of Rh, the occupied and vacant frontier orbitals being well separated. The molecular contrast thus arises from nonresonant tunneling, i.e., through tails of molecular orbital resonances. As already noticed for Xe, this is the quasi-general case for the STM imaging of closed-shell adsorbates.

A detailed description about several theoretical approaches to the contrast mechanism of adsorbate imaging with the scanning tunneling microscope is given in a recent review by Sautet [65].

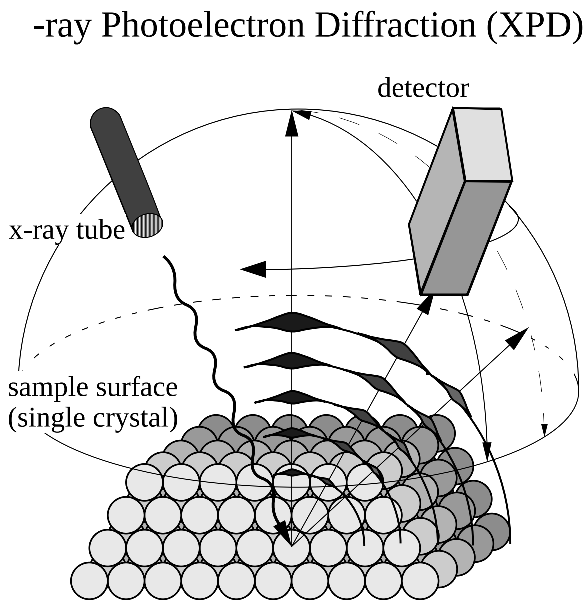

Figure 2.2: Illustration of the sequential acquisition of photoelectron diffraction data over the full hemisphere above the sample surface. (Figure from Ref. [72].)

X-ray Photoelectron Diffraction

In x-ray photoelectron spectroscopy (XPS) [66] the sample is illuminated by monochromatic x-rays of sufficient energy to excite electrons of the core atomic levels. The kinetic energy E_{kin} of the electrons is in a first approximation given by

$$E_{\text{kin}} = \hbar\omega - BE - eW_{\text{det}}$$

where $\hbar\omega$ is the energy of the incident x-rays, BE the binding energy of the electrons and eW_{det} the detector work function.

The fact that core-level photoelectrons emitted from single-crystals exhibit a strongly anisotropic angular distribution was first recognized by Siegbahn *et al.* [67] in 1970. It was soon understood that these intensities modulations are due to final state elastic scattering effects (Photoelectron diffraction) [68]. Already in 1974 it was proposed by Liebsch that photoelectron diffraction should provide a valuable technique for the investigation of the local *geometrical* structure near the photoemitter [69]. The first experimental realizations are reported by Kono *et al.* [70] and Woodruff *et al.* [71] in 1978.

In x-ray photoelectron diffraction (XPD) the intensity of photoelectrons of a certain energy is determined as a function of azimuthal angle ϕ and polar angle θ (cf. Fig 2.2).

The basic physical processes involved in photoelectron diffraction are shown schematically in Fig 2.3. A spherical photoelectron wave emanating from an emitter atom is

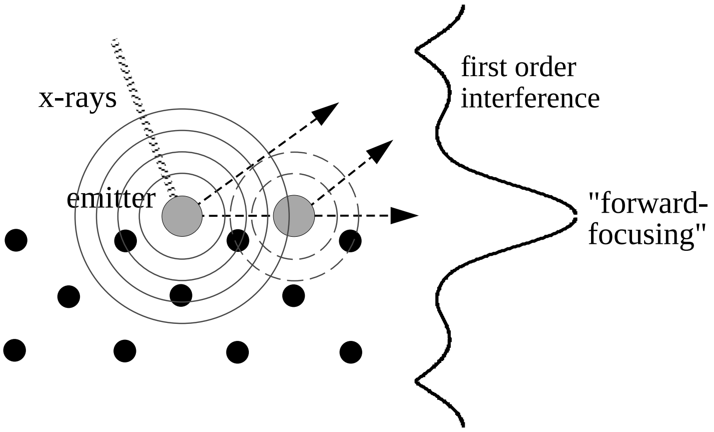

Figure 2.3: A schematic illustration of the dominant elastic scattering processes associated with photoelectron diffraction, which are relevant for adsorbate systems. (Figure from Ref. [72].)

strongly anisotropically scattered by the surrounding atoms, and the scattered components of the wavefield can interfere coherently with the directly emitted wave.

The intensity as a function of the polar and the azimuthal angle is in general displayed in a gray-scale map in stereographic projection. It provides direct and local information in real space and, hence, is a probe of the geometrical structure of surfaces. One of the unique advantages of photoelectron diffraction is the chemical sensitivity which is caused by the characteristic binding energies of the core electrons. This makes photoelectron diffraction an ideal tool to study adsorbates on surfaces. Here the local geometry around every chemically different atom in the adsorbate is probed separately. Most XPD experiments are performed in the higher kinetic energy, or forward focusing, regime. The particular advantage of this kind of experiment is that prominent intensity maxima can often be identified with bond directions, and one finds that the photoelectron angular distribution is to first approximation a forward-projected image of the atomic structure around the photoemitter. As an example in Fig. 2.4 an XPD pattern of the clean Pd(110) surface is reproduced. The prominent spots can be rationalized in the forward-focusing approximation and reflect the substrate symmetry. This directly gives the high symmetry surface directions marked with $[1\bar{1}0]$ and [001].

Single-scattering cluster (SSC) calculations are often used to simulate the XPD pattern [73,74]. The principle of this technique and their wide range of current and potential applications have been extensively described in recent reviews [75, 76]. XPD provides information on the surface crystallographic structure and bonding configuration of adsorbates. It is therefore complementary to STM and LEED.

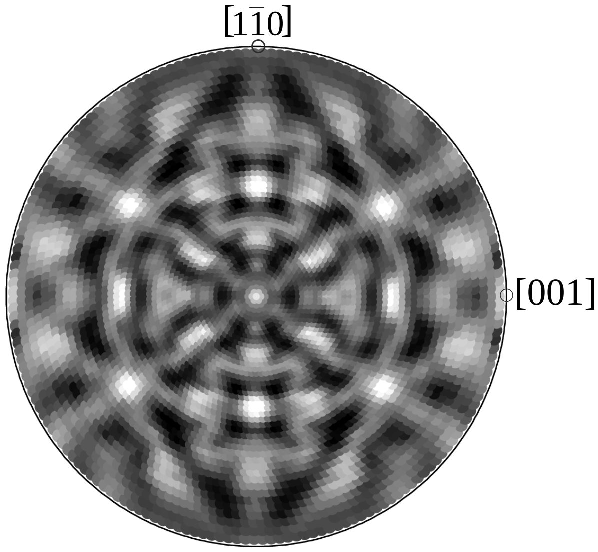

Figure 2.4: XPD Pd_{3d} pattern of a clean Pd(110) surface. The prominent spots can be rationalized in the forward-focusing approximation and reflect the substrate symmetry. This directly gives the high symmetry surface directions marked with [1$\bar{1}$0] and [001].

2.2 Experimental Set-up

The measurements presented in this thesis have been performed with three different UHV chambers. The STM measurements of PVBA and PEBA on Ag(111), Au(111) and Cu(111) presented in Chapter 4, 5 and 6 have been performed with a *low temperature* UHV scanning tunneling microscope. The measurements of PVBA and C_{60} on Pd(110) presented in Chapter 3 and 7 have been taken at a *variable temperature* UHV scanning tunneling microscope. The x-ray photoelectron spectroscopy/diffraction and low energy electron diffraction measurements of Chapter 7 have been acquired in the laboratory of J. Osterwalder at the university of Zürich.

The *variable temperature* STM [77] is operational in the temperature range 40 K–800 K. It is incorporated into an ultrahigh vacuum (UHV) chamber (base pressure $\approx 2 \cdot 10^{-10}$ mbar), which is equipped with standard surface preparation and analysis tools. Several evaporators for metals and organic molecules can be added. The sample is tightly mounted on the sample holder, cooling is realized with a Helium flux cryostat via a Cu-braid and the sample can be heated by electron bombardement (cf. Fig. 2.5).

During STM measurement the sample holder is decoupled from the precision tube and rests on the viton-damped Cu-stack (cf. Fig. 2.5); for low frequency vibration damping the whole UHV chamber is suspended by springs from the ceiling. The STM is a home-built "beetle type" STM (cf. Fig. 2.6). For operation, the STM is simply placed on the sample holder and by applying proper voltage pulses to the outer piezo legs walks

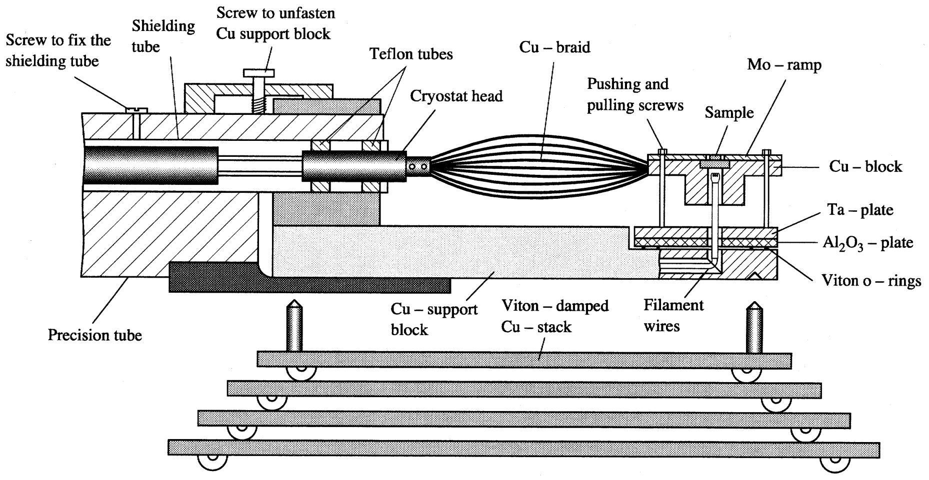

Figure 2.5: Side view of the manipulator and the sample holder. In the STM mode the copper support block is decoupled from the precision tube and rests on the viton-damped Cu-stack (Figure from Ref. [78]).

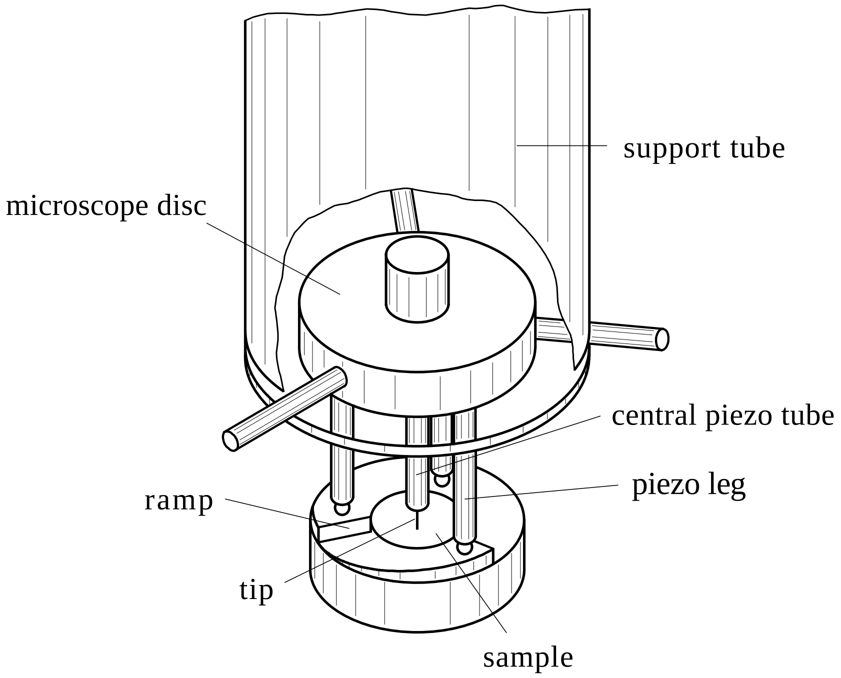

Figure 2.6: Principle of the "beetle-type" STM. The body of the STM, consisting of a microscope disc and three piezo legs, is placed onto a circular ramp. For the coarse approach between the tip and the sample the STM "beetle" - driven by a electrical signal provoking a "stick and slip" movement - walks down the circular ramp on the piezo legs. Once the STM is in the tunneling range scanning is effected through the central piezo, which is a single tube scanner. The STM "beetle" is lifted from the sample with the help of a support tube.

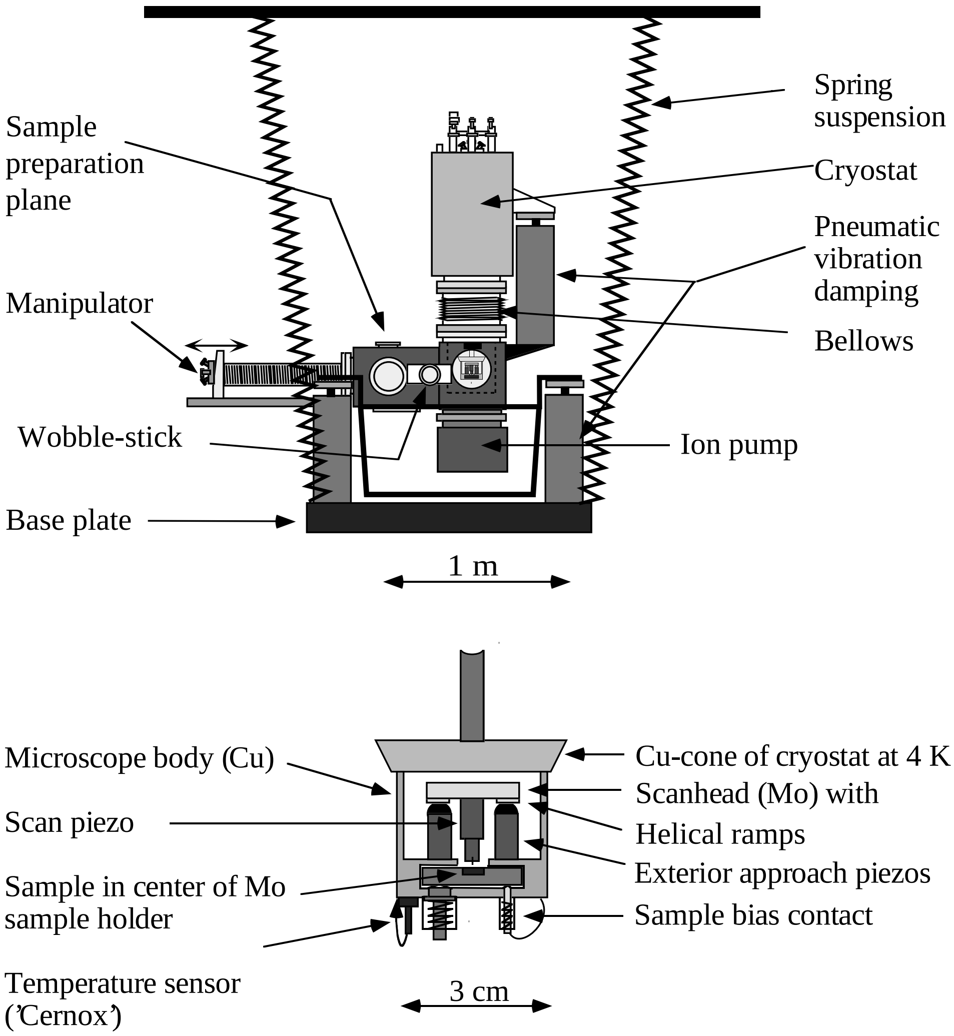

Figure 2.7: Sketch of the UHV-chamber and the 4K-5T scanning tunneling microscope. (Figure from Ref. [80].)

down the ramp. Once the STM is in tunneling range, scanning is effected through the inner piezo. The sample remains mounted to the manipulator during all operations, which throughout guarantees full temperature control. For a detailed description see [78].

The *low temperature* STM is described in detail in [79]. Its basic features are as follows: The UHV-chamber (cf. Fig. 2.7) is equipped with a load lock system. The samples are prepared on a temperature-controlled manipulator (40 K–1000 K) and subsequently transferred into the microscope with a wobble stick. The base pressure of the UHV system is at $\approx 8 \cdot 10^{-11}$ mbar ($\approx 3 \cdot 10^{-10}$ mbar) when the cryostat is at 4.2 K (300 K). It is equipped with standard UHV preparation and analysis tools (sputtergun, Auger spectrometer, two electron beam evaporators) and can be supplemented with up to two organic molecular beam evaporators. The microscope is a modified “beetle type” where the scanning piezo is mounted on a ramp sitting on the three outer piezo (see Fig. 2.7).

This design offers the advantage of easy sample transfer and good thermal contact. The vibration damping consists of three stages: a spring suspension of the base plate from the ceiling and two sets of commercial pneumatic damping elements (Newport). This set-up offers an excellent stability in the order of 5/1000 Å in z-direction.

The x-ray photoelectron spectroscopy/diffraction and low energy diffraction experiments have been performed in a VG ESCALAB Mark II spectrometer modified for motorized sequential angle-scanning data acquisition [75] with the sample held at 300 K. The base pressure is in the lower 10^{-11}-mbar region. The photoelectrons are excited by a Mg K_α x-ray source and detected with a 150-mm radius hemispherical analyzer.

2.3 Sample Preparation

Crystal Preparation

The experiments described in Chapters 4, 5 and 6 have been performed on close-packed fcc(111) surfaces: Ag(111), Au(111) or Cu(111). The crystals are hat shaped with a circular surface of 7 mm in diameter and a total thickness of 3 mm. They were supplied by MaTeck with an orientational misfit of better than 0.1° and mechanically polished (grain size < 30 nm). The samples were cleaned under UHV conditions by sequential cycles of Ar^+ sputtering at 300 K and subsequent annealing. We typically used a 0.5 μA ion beam of 700 eV energy and an incidence angle of 45° for sputtering. One sputter cycle typically lasted 30 min. Annealing was performed during 10 min at a temperature given in Table 2.1. The pressure while annealing was always below $1 \cdot 10^{-9}$ mbar. Usually an impurity depletion layer was created by annealing to temperatures exceeding the usual final temperatures by about 50–100 K for some cycles and only for the final preparation cycles the temperatures given in Table 2.1 were chosen again. This procedure resulted in atomically clean and flat surfaces with regions showing terraces of more than 2000 Å width. For all three surfaces we observed a coverage of less than ≈ 0.05 % of a monolayer (ML) impurities. We were not able to determine the chemical identity of these impurities since our Auger spectrometer only detects residual impurities in coverages larger than ≈ 1 %.

	Cu(111)	Ag(111)	Au(111)
T (K)	820	870	800

Table 2.1: Annealing temperatures.

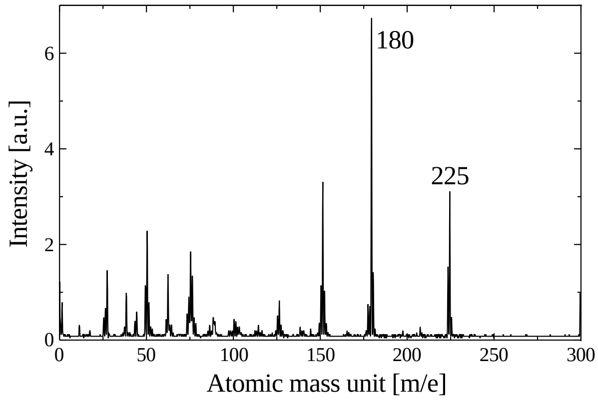

Figure 2.8: Typical mass spectrum of PVBA. The main peak at 180 amu results from single ionized molecules (225 amu) with the COOH-group detached during the ionization process.

The experiments presented in Chapters 3 and 7 have been performed with a Pd(110) crystal of the same geometry as described above. Preparation was by repeated cycles of 700 eV Ar^+ ion sputtering (4 $\mu A/cm^2$) during about 10 min followed by flash annealing to 1050 K resulting in large defect free terraces of typically 1000 Å width.

Organic Molecular Beam Epitaxy

4-[*trans*-2-(pyrid-4-yl-vinyl)]benzoic acid (PVBA), 4-[(pyrid-4-yl-ethynyl)]benzoic acid (PEBA) and C_{60} structures have been prepared *in situ* under UHV conditions. Due to the molecules' high stability and low vapor pressure, a molecular beam can be generated by thermal evaporation under UHV conditions [32, 33, 39]. Thus they have been deposited by a conventional Knudsen-cell at background pressures of $\approx 5 \cdot 10^{-10}$ mbar. In Table 2.2 the temperatures employed for the different materials are given. At these temperatures one physical monolayer is formed within about 2 minutes. For very low coverages a lower evaporation temperature was chosen to obtain an evaporation time in the order of one minute.

	PVBA	PEBA	C_{60}
T (K)	540	500	600

Table 2.2: Evaporation temperatures.

The molecular mass of PVBA and PEBA amounts to 225 amu and 223 amu, respectively. The geometries have been simulated with the computer code AM 1 in MOPAC (Cerius 2, BIOSYM/Molecular Simulations). As demonstrated by solid state ^{15}N NMR spectroscopy the crystal structure is mainly stabilized by hydrogen bonding [81], which is reflected in a rather high melting point of 350°C and 300°C, respectively [82]. A typical mass spectrum of PVBA is shown in Fig 2.8. The main peak at 180 amu results from single ionized molecules (225 amu) with the COOH-group detached during the ionization process.

A new organic molecular beam evaporator has been installed during this thesis. It is mounted on a linear z-drive and can be retracted behind a gate valve for changing substances without breaking UHV in the main chamber.

Chapter 3

PVBA on Pd(110): Large Organic Molecules on an Anisotropic Metal Surface

In this Chapter we present data of the PVBA [4-[*trans*-2-(pyrid-4-yl-vinyl)]benzoic acid]/Pd(110) system as an example for the ordering and diffusion of a large organic molecule on an anisotropic substrate in the presence of strong adsorbate-substrate interactions. PVBA is especially designed to form strong hydrogen bonds [81] and as a consequence, substantial attractive interactions between PVBA molecules adsorbed on a surface might be expected. Our data, however, demonstrate that with the present system the adsorbate-substrate interactions completely determine the film growth and bonding geometry, which remains unaffected by intermolecular interactions.

So far predominantly static aspects or direct manipulation of large organic molecules at surfaces have been addressed [83]. However, to fully understand their ordering and interactions at metal substrates, a necessary prerequisite for further developments in the field, an understanding of their surface kinetics is indispensable.

We report the first direct study of the surface diffusion of a large organic molecule chemisorbed on a metal surface. In contrast to thermal motions of adsorbed atoms or simple molecules, which frequently can be rationalized straightforward in a single particle hopping model, due to the more complex binding geometry including the possibility of conformational changes and both rotational and internal degrees of freedom, a rather complex scenario for the surface diffusion of large molecules might be expected [84–87]. However, to date there is a lack of systematic direct investigations, even if macroscopic techniques, such as laser-induced thermal desorption (LITD) were employed to address this problem [88].

In Section 3.1 the adsorption and ordering characteristics of PVBA on a Pd(110) are addressed. The molecules adsorb flat on the surface and bind diagonally to three neighboring Pd-rows, leading to four equivalent adsorption configurations. The “dog-bone” molecular structure could be resolved. This configuration is maintained at all submonolayer coverages. At low coverages single PVBA molecules are randomly distributed at the surface. With the completion of the first monolayer a parquet pattern evolves, resulting from the fixed bonding geometry and space limitations. Monte Carlo simulations of the film growth confirm that the monolayer ordering is stochastic in nature, even if an extrinsic precursor mechanism is operative in the adsorption. The lateral interactions between adsorbed molecules and Pd steps or adatoms at the surface are weak.

In Section 3.2 the surface diffusion of PVBA on Pd(110) is investigated by variable temperature STM at sample temperatures between 300 K and 450 K. The molecules' surface diffusion is strictly one-dimensional along the close-packed $[1\bar{1}0]$-direction of the surface Pd atomic rows and obeys an Arrhenius law with an activation barrier of (0.83 ± 0.03) eV and an attempt frequency of $10^{(10.3\pm0.4)}$ s^{-1}.

3.1 Binding and Ordering

A high resolution STM image with a small amount of PVBA evaporated on the Pd(110) surface is depicted in Fig. 3.1(a). The image reveals the ordering and adsorption geometry of PVBA molecules. The individual molecules lie flat on the surface and are imaged as 1.25 Å high protrusions with a length of $\approx$ 11 Å. The STM shape is in accordance with the geometrical distance between the extremal atoms of an isolated molecule (12.3 Å in the unrelaxed configuration [81]), the chemical structure formula of which is represented in the inset in Fig. 3.1(a). The molecule consists of a pyridyl group attached to a benzoic acid via a vinyl group. The corresponding “dog-bone” internal molecular structure, which is associated with the two coupled aromatic ring systems, is clearly discernible. The molecules are randomly distributed at the surface, which also holds for adsorption conditions with high molecular mobility or upon annealing of the surface. This indicates that molecule-substrate interactions by far exceed the intermolecular interactions. The molecular axis is oriented by $\pm 35^\circ$ with respect to the close-packed $[1\bar{1}0]$ surface directions. A detailed analysis of the STM data reveals a binding of the molecules to three neighboring Pd atomic rows, as demonstrated by the ball model in Fig. 3.1(b) (whereas the position in [001] is certain, the position of the molecule in $[1\bar{1}0]$ could not be exactly determined as atomic resolution of the substrate in this direction could not be achieved in the presence of the molecules). The

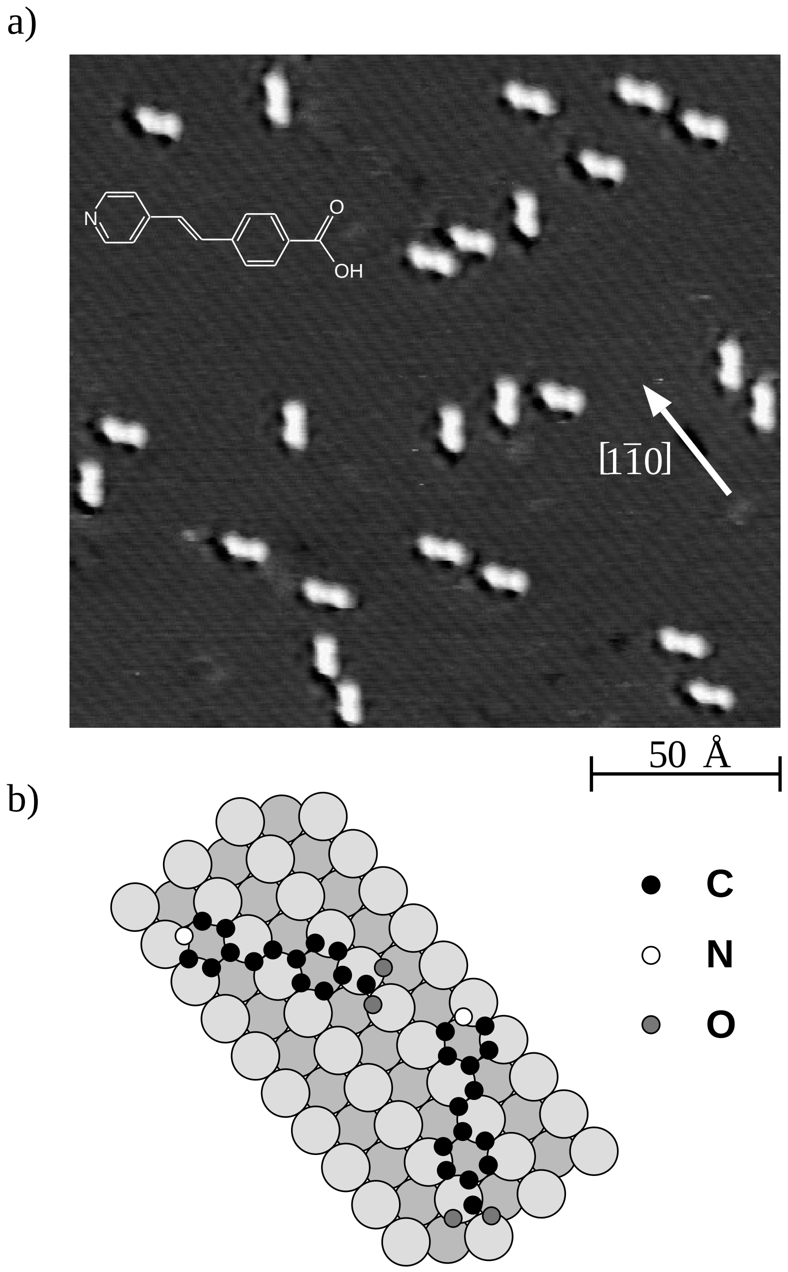

Figure 3.1: **(a)** PVBA molecules randomly distributed on the Pd(110) surface at low coverage ($\theta = 0.018$ ML). The molecules were adsorbed and imaged at a substrate temperature of 325 K and deposited with a rate of $3 \cdot 10^{-5}$ ML/s. The atomic rows of the Pd substrate and the "dog-bone" internal molecular structure are resolved (image size: 190 × 180 Å^2; $U_t = 1.04$ V, $I_t = 1$ nA). The chemical structure formula of 4-[*trans*-2-(pyrid-4-yl-vinyl)]benzoic acid (PVBA) is depicted in the inset. **(b)** Ball model for unrelaxed PVBA molecules on Pd(110). Light (dark) grey circles: Pd atomic rows of the surface (second) layer; small circles: individual PVBA atoms (omitting H atoms). The molecular axis is oriented by ±35.3° with respect to the [1$\bar{1}$0] Pd rows providing optimal coordination of surface Pd and molecular subunits.

data are in agreement with STM observations on the systems benzene/Pd(110) [89] and benzene/Ni(110) [90] where the C-ring was found at the fourfold hollow site of the substrate. The two different lobes of the molecule did not exhibit significantly different STM imaging characteristics. Dissociative adsorption with desorption of CO_2 cannot be entirely ruled out, but seems unlikely since there are no indications for the disruption of a carboxylic acid by Pd in the literature (possibly deprotonation occurs). In addition, very similar imaging characteristics were encountered for weakly bound PVBA on the noble metal Ag(111) surface (cf. Chapter 4). Hence it is believed that the symmetric shape results from the transparency of the carboxylic group not contributing to the tunneling current. Similar observations have been reported for fatty acids, where only the hydrocarbon backbones are imaged by STM and the carboxylic groups are nonconducting parts of the molecules [91] and for other large planar π-conjugated molecules adsorbed in a flat lying position on a metal surface, where the π-orbitals dominating the bonding to the metal states are imaged by STM [37]. The adsorption geometry reflects optimal coordination of the molecular subunits and the palladium surface atoms achievable without strong distortions of neither intramolecular nor substrate structure. The results indicate that the surface chemical bond of the organic molecules with the Pd substrate is predominantly due to π-binding via the electron ring systems of the pyridyl and the benzyl group, respectively [92, 93]. Due to the substrate symmetry and molecular asymmetry four equivalent molecular configurations are possible. Since the molecular end groups are not differentiated, only the two different orientations with respect to the $[1\bar{1}0]$ Pd atomic rows can be discriminated.

A molecule aligned in one orientational configuration cannot be transformed into the mirror configuration by a simple rotation for symmetry reasons. Rather, the molecule would have to be flipped about its own axis in addition. This is believed to be a reason why molecular rotations were not directly observed.

By contrast, the thermal migration of individual molecules could be directly monitored. A detailed analysis of STM data obtained in the temperature range 330–370 K reveals a strictly one-dimensional diffusion along the close-packed Pd-rows with an activation barrier of (0.83 ± 0.03) eV and an attempt frequency of $10^{(10.3\pm0.4)}\mathrm{s}^{-1}$ (see Section 3.2). No effects of lateral interactions became apparent in the molecular surface migration. The rather high migration barrier indicates a PVBA-Pd(110) binding energy of several eV, which is in line with the strong interaction of aromatic vinyl compounds and palladium atoms documented in organometallic chemistry [94].

With medium coverage little changes occur in the PVBA film structure. This is illustrated by the STM image in Fig. 3.2, where a medium coverage of PVBA on Pd(110)

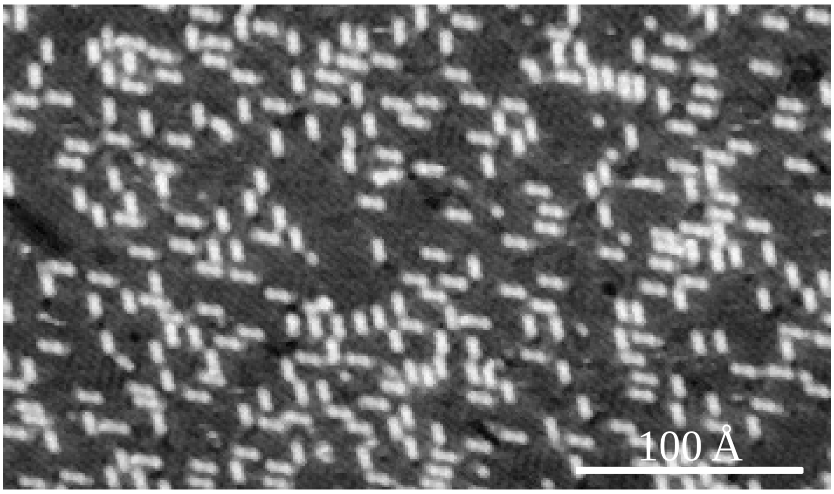

Figure 3.2: Medium coverage ($\theta = 0.037$ ML) of PVBA on Pd(110). All data obtained at a substrate temperature of 325 K with a deposition flux of $3 \cdot 10^{-5}$ ML/s.

is reproduced. Again, the two different rotational geometries are clearly visible. The molecules also remain randomly distributed on the surface, and even after annealing or deposition at 450 K, where the molecules are highly mobile, there are no indications of island formation. These findings demonstrate that the expected attractive interactions between the molecules are very weak or even absent and merely the short-range repulsions exist, which are always present. Presumably the fixed adsorption geometry lowers the possible energy gain from hydrogen bond formation. This forces the angle between the molecular axis and the close-packed Pd-rows to ±35° for optimal coordination of the molecular subunits with the Pd surface atoms. As a consequence the angle between two PVBA molecules corresponds to 110° instead of the ideal angle of 180° for hydrogen bonding [81]. Dipole interactions must be similarly weak. It is believed that the molecular dipoles are efficiently shielded by the electron gas of the metal surface. On less corrugated substrates with weaker adsorbate-substrate interactions, e.g., a fcc(111) noble metal surface, where the molecules are free to rotate, the hydrogen bonding and dipole interactions should play a major role in the ordering and molecular chains or clusters should be formed. Such a behavior was indeed observed for PVBA on Ag(111), Cu(111) and Au(111) surfaces (cf. Chapter 4 and 5). Upon further increasing the coverage a parquet-like pattern of flat lying molecules evolves, as demonstrated by the STM image reproduced in Fig. 3.3. With this monolayer structure the PVBA film on Pd(110) is completed at room temperature. Multilayer growth could not be observed. In the lower part of Fig. 3.3 a ball model for the rectangular area marked in the STM image is shown. Since it is impossible to distinguish between molecular head or tail groups, only the two different rotational geometries are drawn and all molecules of one orientation

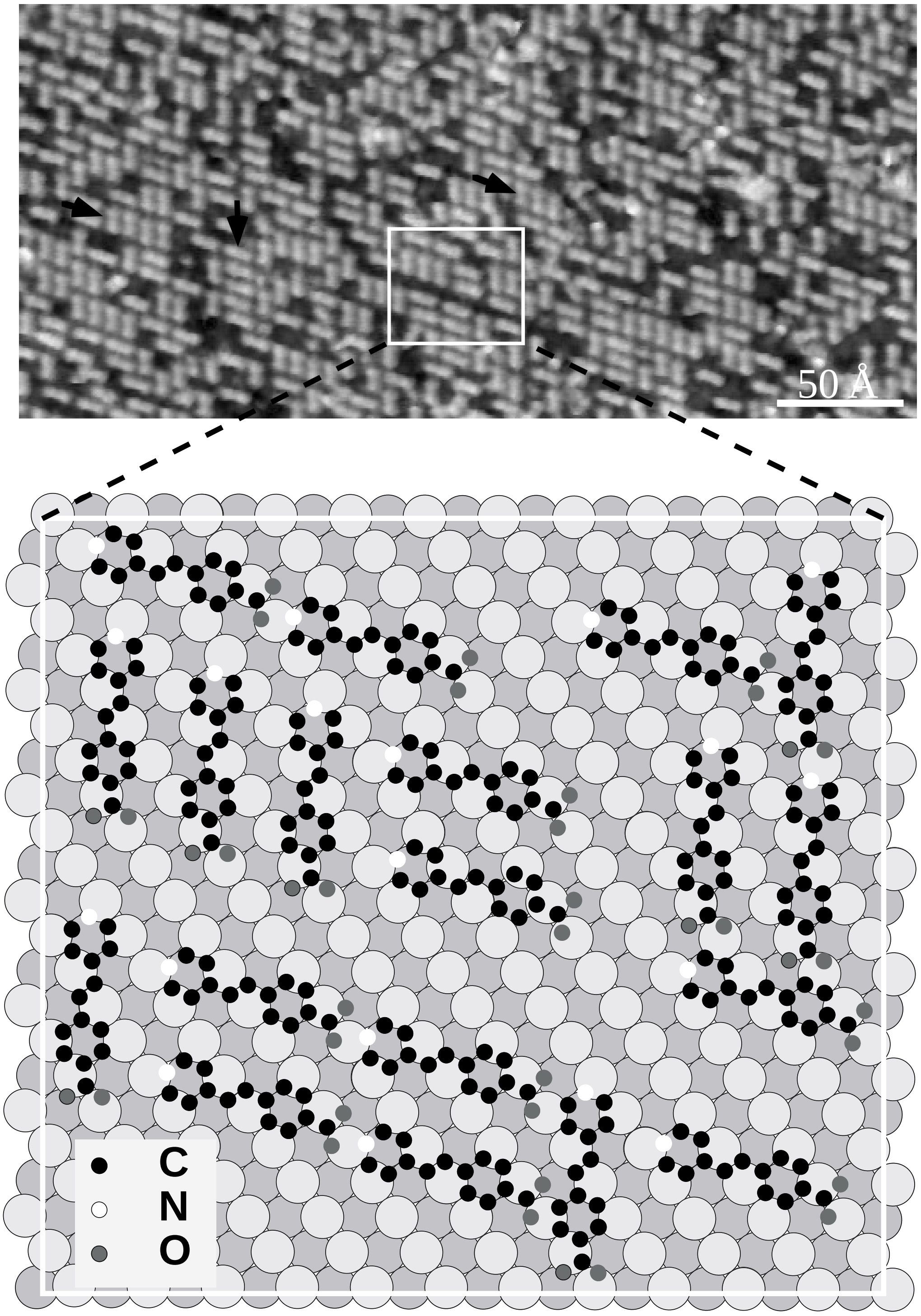

Figure 3.3: **(top)** STM image of a nearly completed monolayer of PVBA on Pd(110) ($\theta = 0.076$ ML $\simeq 0.60\theta_{\mathrm{id}}$) ($U_t = -1.0$ V; $I_t = 0.8$ nA). Arrows mark clusters of three or more side by side parallel molecules. **(bottom)** Ball model of the molecular ordering of PVBA on Pd(110) for the area marked in the STM image.

are identically aligned. From the ball model the nearest neighbor distance of adsorbed PVBA is determined to be $\sqrt{4a_1{}^2 + a_2{}^2} = 6.74$ Å, where $a_1 = 2.75$ Å and $a_2 = 3.89$ Å are the lattice constants of the Pd surface in $[1\bar{1}0]$ and [001], respectively. Locally, ordered clusters where molecules are oriented parallel at next-neighbor positions are found, as marked by the arrows in the STM image in Fig. 3.3. Overall, however, the film structure is not ideal and a substantial fraction of the bare surface remains that cannot be filled up with molecules. Packing with higher density is obviously prevented by the strictly one-dimensional motion along the $[1\bar{1}0]$-direction in connection with the simultaneous bonding of the molecule to three neighboring Pd-rows. Even deposition or annealing up to 450 K does not result in an improved ordering, whereas upon annealing to higher temperatures of approximately 600 K STM data show that the surface is littered with undefinable material. This is associated with the decomposition of the chemisorbed molecules and fragment desorption. Thus a more densely packed monolayer could not be fabricated. The relative coverage of the monolayer in Fig. 3.3 corresponds to approximately 60% of a perfectly ordered defect-free layer where the surface unit-cell contains eight Pd atoms (corresponding to an ideal monolayer coverage of $\theta_{\mathrm{id}} = 1/8$ ML).

During the course of the experiments we noted that the PVBA sticking coefficient does not fall rapidly as expected (with the formation of a well-ordered overlayer a $(\theta_{\mathrm{id}} - \theta)^8$ power law should hold in the absence of precursor mechanisms [95]). Rather, it remained nearly constant up to a coverage of at least $0.25\theta_{\mathrm{id}}$. As a consequence, an extrinsic precursor mechanism [96–98] must be operative in the PVBA film formation. This implies that adsorbing molecules hitting on top of an already occupied surface area are weakly bound and able to migrate to free sites on the Pd(110) surface. Now, it is conceivable that this process may influence the ordering of the PVBA film, since the precursor molecules are presumably free to rotate and their final accommodation may be influenced by the already adsorbed molecules or the interactions of the precursors with the latter. In order to get more insight into the mechanism of PVBA ordering, we performed Monte Carlo simulations of the adsorption process. The MC-simulations have been performed on a 100×100 large rectangular lattice with periodic boundary conditions. Each molecule is determined by the two coordinates (x and y) of the phenylene-ring plus a variable being 0 or 1 for the left- or right-hand molecular species. At the surface one adsorbed molecule inhibits adsorption at 18 neighboring positions (cf. Fig. 3.3). Molecules are adsorbed only when the surface site chosen by the random number generator is free, otherwise they are rejected. A random configuration of the film is obtained within the immobile adsorption model [95] excluding the PVBA surface migration. A typical result from such a Monte Carlo simulation is reproduced

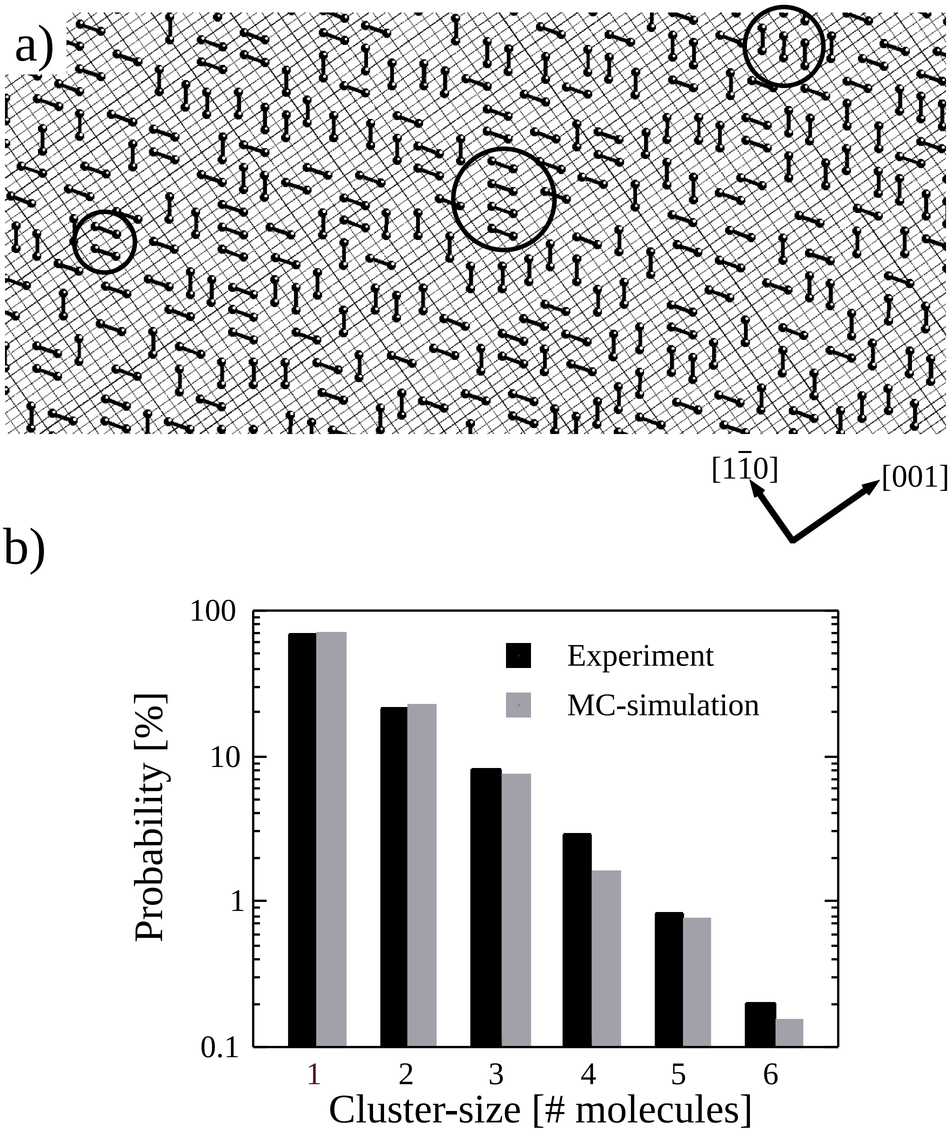

Figure 3.4: **(a)** Monte Carlo simulation for PVBA on Pd(110) film growth with site-blocking and immobile adsorption. Circles mark molecular clusters which are similarly found in the STM images in Fig. 3.3, where an extrinsic precursor mechanism is operative. **(b)** Comparison of cluster size distribution obtained from STM images and Monte Carlo simulations. There is no significant difference in the ordering, indicating that the extrinsic precursor mechanism with the molecules' adsorption does not improve the film ordering for the present system.

in Fig. 3.4(a), whose inspection clearly reveals that the cluster formation of molecules can be reproduced simply within this model. For a quantitative analysis several runs of the MC-simulation with different seed-values have been performed and the distribution of cluster sizes was determined. The statistics shown in Fig. 3.4(b) compare the results of the MC-simulation with the experimental findings. Experimental and simulation statistics are each based on a total number of approximately 3000 molecules

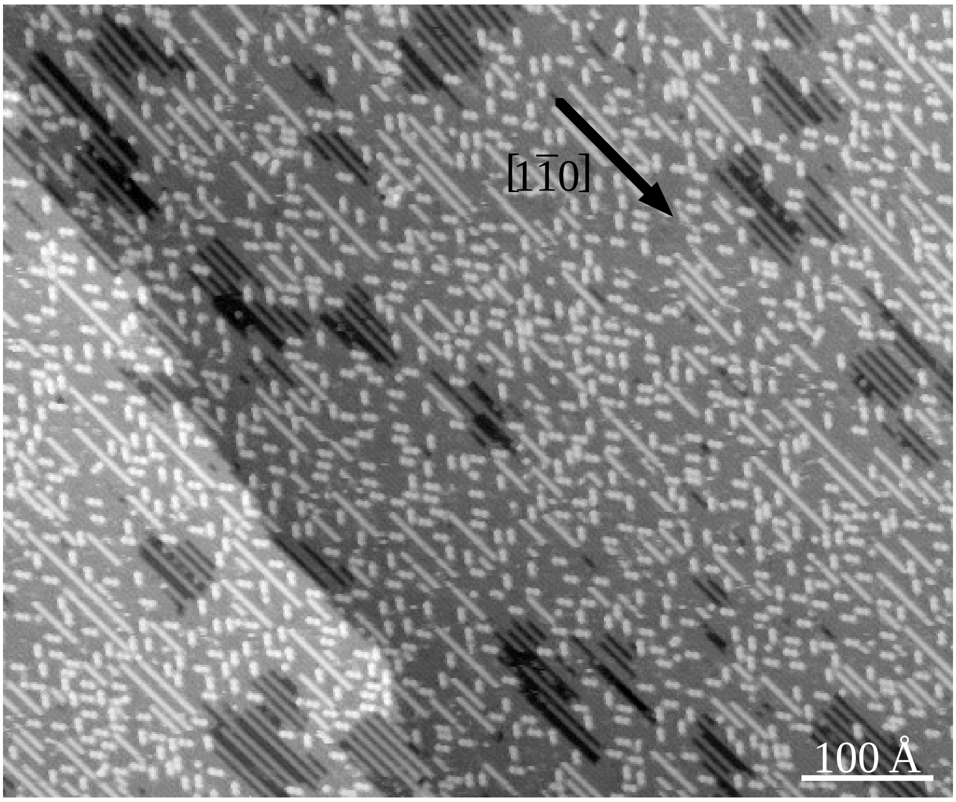

Figure 3.5: STM image of the Pd(110) surface covered with 0.018 ML PVBA (U_t = 1.4 V; I_t = 1.1 nA) and subsequent local H-induced missing row reconstruction. The added Pd rows are formed of the released Pd atoms. The measurements demonstrate the small lateral interactions of adsorbed PVBA and Palladium at 300 K.

and clusters. The agreement between experiment and simulation is very satisfying and shows that the film ordering can be fully understood on the basis of a "hit and stick model". The extrinsic precursor mechanism does not lead to a film ordering which is superior to that from statistical, immobile adsorption with the present system. In addition, monolayer completion with the maximum coverage of about $0.65\theta_{\mathrm{id}}$ obtained by the MC-simulations agrees well with the experimental results. Nevertheless, it is suggested that precursor-mediated molecular ordering is feasible with other systems.

Finally, we address the anisotropic nature of the PVBA-Pd interactions. In Fig. 3.5 an STM image of PVBA evaporated on the clean Pd(110) surface is shown. Subsequently a (1×2) missing row reconstruction was induced on the surface by dosing hydrogen [99]. The black stripes in the image are missing Pd rows, whereas the white stripes are added Pd rows formed of the released Pd atoms. Even if there is a substantial number of highly mobile Pd atoms on the surface, they do not bind laterally to the adsorbed PVBA molecules. There is also no preferential adsorption of PVBA at the atomic step (left side of the image). This means that although the adsorbate-substrate interaction is rather strong, the lateral interactions of adsorbed PVBA with released Pd atoms and Pd steps are small. The strong direction-dependence of the interaction signals again that binding from the PVBA molecules to the Pd substrate is mainly due to the π-electrons [92,93]. Accordingly, we found strong lateral interactions of Pd with C_{60} molecules adsorbed on Pd(110). In this case the ball shape of the molecular geometry provides the additional possibility of lateral π-bonding (cf. Chapter 7).

In conclusion, we have demonstrated that the adsorption and growth of PVBA on the Pd(110) surface is dominated by strong adsorbate-substrate interactions. The PVBA molecules adsorb in two rotational configurations giving optimal coordination of the molecular subunits with the Pd surface atoms. This adsorption geometry is maintained over the entire submonolayer range. In contrast to expectations, no effects of lateral molecular interactions are revealed, which is attributed to strong adsorbate-substrate interactions. They result in a fixed adsorption geometry, which is maintained under all conditions. With the completion of the first monolayer thus a parquet pattern evolves due to space limitations. Corresponding Monte Carlo simulations of the PVBA growth reveal the stochastic nature of the parquet pattern.

3.2 Surface Diffusion

In the following the molecular surface diffusion will be addressed. The STM measurements were performed in the constant current mode with typical tunneling voltages of ±1 V and currents below 1 nA, i.e., in the high tunneling resistance regime (> 1 GΩ). It was impossible to manipulate the adsorbed molecules under any tunneling conditions, which reflects a strong substrate-adsorbate interaction. We also investigated the possibility of tip-induced changes in the surface diffusivity, however, no modifications in the diffusion characteristics were observed at the employed high tunneling resistances.

The thermal motion of *individual* molecules could be monitored. STM data demonstrating molecular surface diffusion at a substrate temperature of 361 K are reproduced in Fig. 3.6. The data were recorded at the same area with a time lapse of 220 s between the two images shown. Two effects due the thermal mobility can be discerned upon inspection of the data. On the one hand, a comparison of consecutive images reveals that a fraction of the molecules changed position in the time interval between the recording. An analysis of the positional changes demonstrates that the PVBA surface diffusion is strictly one-dimensional along the close-packed substrate direction. The molecular displacements are thus exclusively along $[1\bar{1}0]$. This holds similarly for higher temperatures and reflects the anisotropy of the fcc(110) surface which results in different

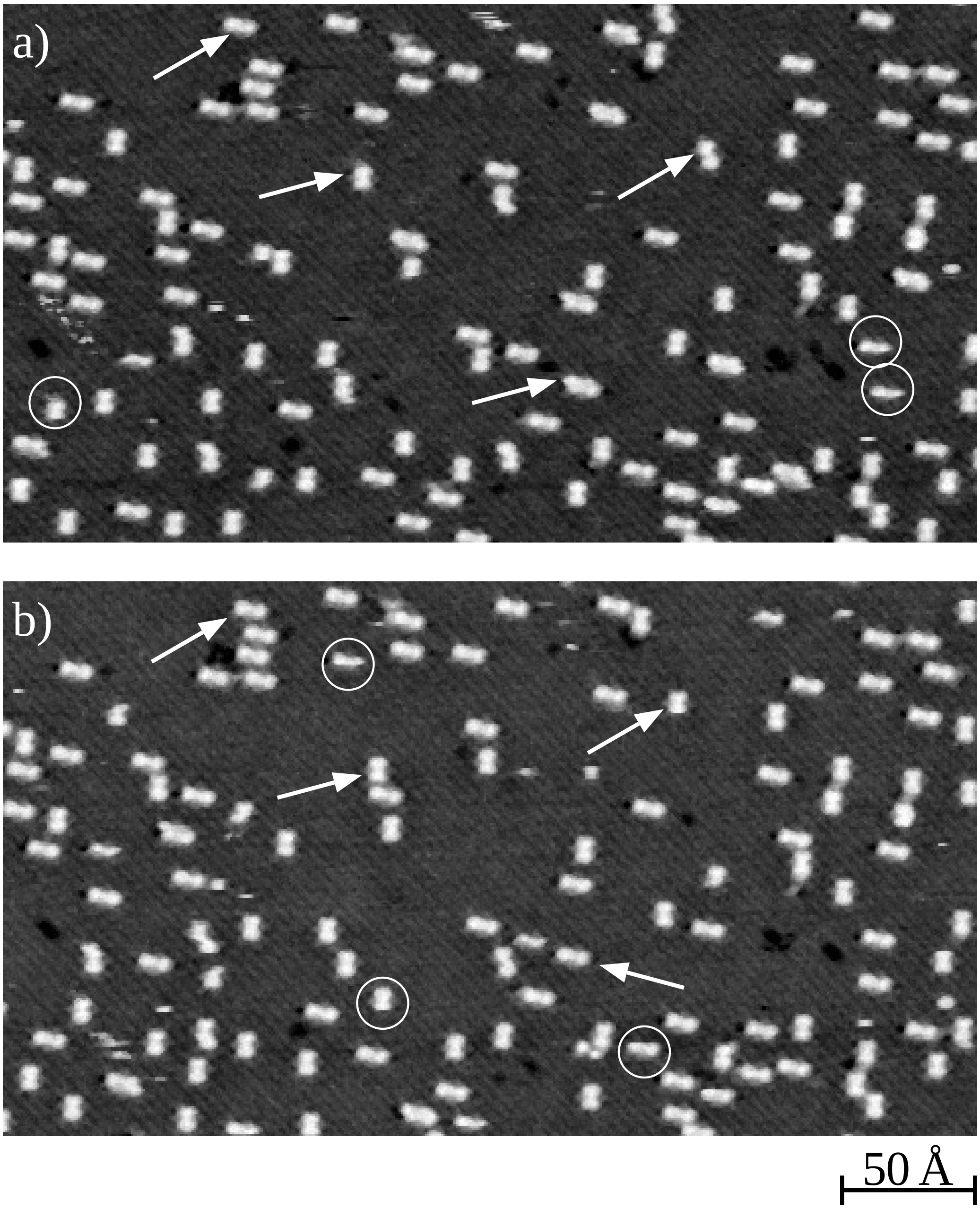

Figure 3.6: Series of STM images monitoring thermal motions of PVBA molecules on Pd(110) at $T = 361$ K (image sizes: 360×200 Å^2; $U_t = 1.20$ V, $I_t = 0.4$ nA). The time lapse between the two consecutive images is 220 s. Arrows indicate molecules whose position changed revealing the one-dimensional nature of the surface diffusion; circles mark molecules moving under the STM tip which are fractionally imaged.

diffusivities along the primitive surface directions, earlier observed for simpler molecular adsorption systems [100,101]. On the other hand, the imaging characteristics of single molecules within an individual STM image are subject to surface diffusion: since the imaging of the molecule requires a certain number of line scans and thus a certain time interval, there is a probability that molecules diffuse away from the area under the STM tip while recording the images. Thus the limited residence time at a specific site leads to an incomplete imaging of a fraction of the molecules. They show up in a reduced number of neighboring scanlines before they hop away during the measurement, whereupon characteristic "cut-off" features in the topographs are created (marked by circles in Fig. 3.6). These features are used to analyze the molecular surface diffusion with the present system.

The hopping rates are obtained from the number of scanlines where molecules are imaged at their original sites: the probability that a particle remains at a given site after time τ is $P(\tau) = \exp(-\nu_s \tau)$, where ν_s is the hopping rate to be determined [102]. τ is chosen such that it corresponds to the time necessary to image a molecule entirely, for which the number of scan lines times the scanning period (of the fast x-direction) was taken. Accordingly, $(1 - P(\tau))$ is the fraction of molecules which jumped within this time interval and the rates can be obtained from a statistical analysis of series of images. With the present system, the two orientational configurations of the molecule provide an additional check of this method. Since the fast scan direction is not parallel to the Pd surface atomic rows, the number of line scans for complete imaging of molecules in the respective configurations differ. However, the analysis of the individual geometries agree well and the same hopping rates are obtained. The temperature range accessible with the present system and instrumentation is the region 330–370 K. In addition, experiments employing different scan rates were performed, which substantiate the above statement that the molecular surface diffusion is unaffected by the STM tip.

The statistical hopping frequency analysis is plotted in the Arrhenius representation in Fig. 3.7. The results clearly demonstrate that the one-dimensional motion of the large organic molecule obeys an Arrhenius law. The linear fit of the data yields an activation barrier of (0.83 ± 0.03) eV. The corresponding attempt frequency amounts to $\nu_0 \approx 10^{(10.3\pm 0.4)}$ s^{-1}. The fact that the molecules' migration can be described by an Arrhenius law indicates that a single process is decisive for the motion of the molecules and that possible complexities due to the large molecular size do not result in extraordinary diffusion characteristics. Although the corrugation potential experienced by the large molecule is believed to be much more complex than that of an adsorbed simple molecule or atom, and intramolecular degrees of freedom might interfere, the molecular surface

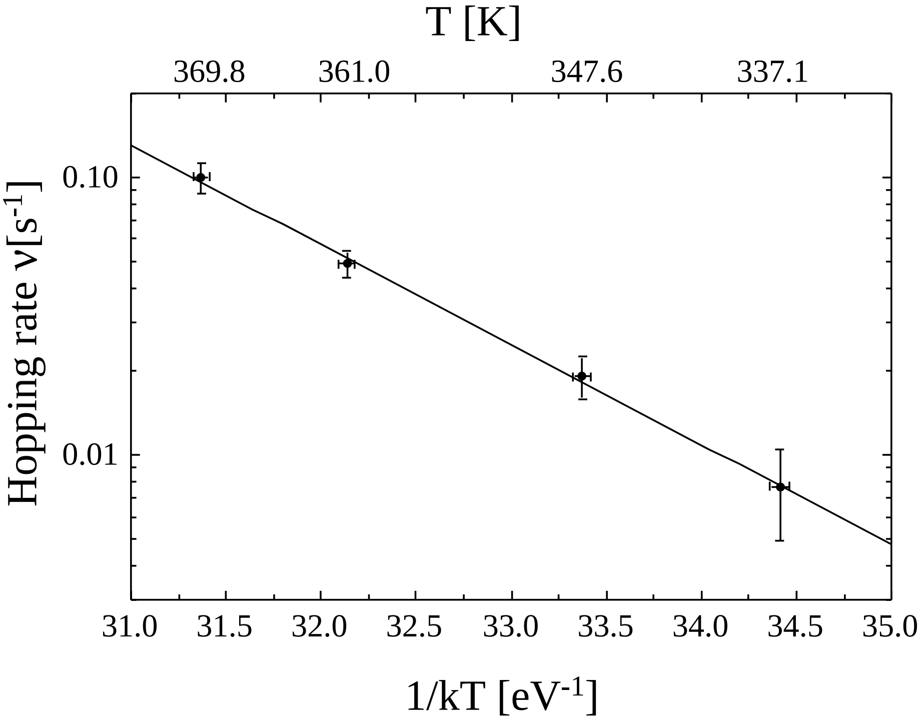

Figure 3.7: Arrhenius plot of single molecule hopping rates along the [1$\bar{1}$0] substrate direction in the temperature interval between 335 and 370 K. The surface diffusion of the large organic molecule obeys an Arrhenius law with an energy barrier of (0.83 ± 0.03) eV and an attempt frequency of $10^{(10.3\pm0.4)}$ s^{-1}.

diffusion can be described in simple terms. In agreement, molecular dynamics simulations of surface diffusion of n-alkanes report that an Arrhenius expression adequately describes large molecular motions for which complex diffusion mechanisms exist [84,86]. The migration barrier of the adsorbed molecules *per se*, is high and signals a rather strong bonding of the molecules to the Pd surface. Whereas for small adsorbates migration barriers (E_m) are typically ≈10%–20% of the binding energy (E_b), higher ratios of ≈30% have been reported for larger molecules [88], which would imply $E_b \approx 2.8$ eV with the present system. This compares well with the significantly higher mobility of benzene adsorbed at the same surface [89], where a weaker surface chemical bond is formed ($E_b \approx 1$ eV) [103]. Similar $E_m - E_b$ trends were reported for surface diffusion of n-alkanes on Ru(001) [88], studied by LITD experiments. With these investigations it was also speculated that the diffusion coefficients associated with the large molecules' chemical surface diffusion are much larger than would be expected from a hopping model where the molecules jump just by one surface lattice constant. Long jumps were suggested as a possible explanation for this behavior [86,88], however it must be noted that the LITD results have been obtained by means of an integral, nonlocal technique, where the ubiquitous surface defects such as atomic steps may interfere. An analysis of our data revealed that they are in agreement with statistics excepted from one-dimensional next-neighbor hopping and exclude the possibility of the rather long jump lengths (40–50 Å) invoked for the interpretation of n-alkanes' surface diffusion on Ru(001) LITD results [88], where we are dealing however, with weakly bound molecular species. Nevertheless, a precise quantitative analysis of the jump length is not possible with the present investigation due to slight thermal drift distortion obscuring comparison of consecutive images, so that a small fraction of molecular jumps over two or three lattice sites cannot be entirely ruled out. Assuming single site molecular hopping, a preexponential factor for the tracer diffusion coefficient of $D_0 = \frac{1}{2}a^2\nu_0 = 7.55 \cdot 10^{-6}$ cm^2/s for the one-dimensional motion is obtained. The results ascertain that the attempt frequency associated with the molecular motion ($\nu_0 = 10^{(10.3\pm0.4)}$ s^{-1}) is about two orders of magnitude smaller than that of benzene on Pd(110), where estimates signal $\nu_0 \approx 10^{12}$ s^{-1} [89, 104]. The small attempt frequency with the present system possibly indicates a bonding configuration with reduced entropy in the transition state leading to an effective attempt frequency reduction. Further theoretical investigations are suggested to clarify this issue. It is interesting to note that for small molecules, e.g., acetylene the energy barrier for rotation is much smaller than for migration [105]. In contrast, for PVBA on Pd(110) thermal rotation is not observed in the investigated temperature interval.

In conclusion, the surface diffusion of PVBA on Pd(110) is investigated by variable temperature STM at sample temperatures between 300 K and 450 K. The molecules' surface diffusion is strictly one-dimensional along the close-packed $[1\bar{1}0]$-direction of the surface Pd atomic rows and obeys an Arrhenius law with an activation barrier of (0.83 ± 0.03) eV and an attempt frequency of $10^{(10.3\pm0.4)}$ s^{-1}. These investigations demonstrate that variable temperature STM is a well performing tool to investigate surface diffusion of adsorbed large organic molecules with high precision. It is suggested that this technique will be of general use in studies concerning the kinetics of adsorbed large molecular species at surfaces.

Chapter 4

PVBA on Ag(111): One-Dimensional Supramolecular Nanostructures

This Chapter deals with 4-[*trans*-2-(pyrid-4-yl-vinyl)]benzoic acid (PVBA) on Ag(111). On the Pd(110) surface strong adsorbate-substrate interactions completely determine the ordering of PVBA (cf. Chapter 3). The fixed bonding geometry together with strictly one-dimensional diffusion prevents the formation of head-to-tail hydrogen bonds. The smoothness of the noble metal Ag(111) surface and weak adsorbate-substrate interactions allow for higher mobility including rotational motions and attractive intermolecular interactions become apparent.

At low temperature (125 K) PVBA is mobile on Ag(111) and molecular networks of flat lying molecules are formed in a diffusion limited aggregation process. The molecules are linked via the *endgroups* which is in line with the expected hydrogen bond formation.

Equilibrium is reached upon annealing or adsorption at 300 K. Molecular twin chains running along a $<11\bar{2}>$-direction of the substrate evolve. High resolution STM images illustrate that molecules within a row are pointing in the same direction allowing the formation of head-to-tail hydrogen bonds. Adjacent rows are aligned antiparallel and shifted. Due to the distinct shift in twin chains the built supramolecular structures are enantiomorphic. Their chirality is directly associated with the chirality of single PVBA molecules adsorbed on a surface.

Between neighboring twin chains repulsive interactions are operative and hence a one-dimensional supramolecular nanograting evolves. The periodicity can be varied over a wide range by the coverage.

In large domains, typically in the μm-range, all twin chains are of the same chi-

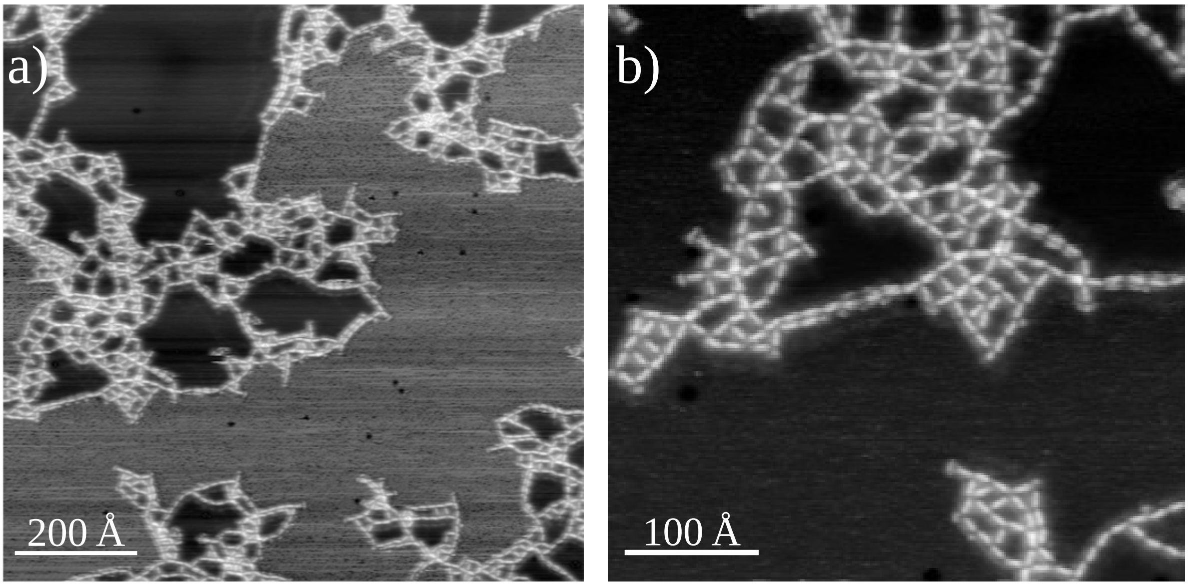

Figure 4.1: PVBA evaporated on Ag(111) held at 125 K (measured at 77 K). **(a)** Networks of meandering chains are formed demonstrating surface mobility at low temperatures and attractive interactions. **(b)** Close-up view showing that the molecules interact via the molecular *endgroups* which is in line with the expected hydrogen bond formation. The observed growth scenario can be considered as diffusion-limited aggregation of rod-like particles subject to anisotropic interactions.

rality despite their interrow distance in the 10–100 Å-regime. A scenario is developed supported by MD-simulations in which chirality proliferates during the growth process.

4.1 STM observations

In Fig. 4.1(a) an STM topograph of PVBA adsorbed on Ag(111) held at 125 K is depicted (measured at 77 K). It reveals that PVBA is mobile on the Ag(111) surface at low temperature and networks of meandering chains are formed. No isolated molecules can be imaged on flat terraces but the noisy background on empty areas might be due to mobile molecules dragged by the STM tip. The close-up view in Fig. 4.1(b) reveals the flat adsorption of PVBA on Ag(111). This is associated with directed π-bonding to the substrate and is similarly found for PVBA on Pd(110) (cf. Chapter 3) and other large organic molecules with extended π-systems, e.g., oligothiophenes on Ag(111) [32, 106]. Attractive interactions between the molecular *endgroups* are operative, which is in line with the directional interactions expected from hydrogen bond formation. Molecular strings thus evolve at the surface, and their curved shape signals that the substrate corrugation experienced by the molecules is rather weak. This is attributed to the

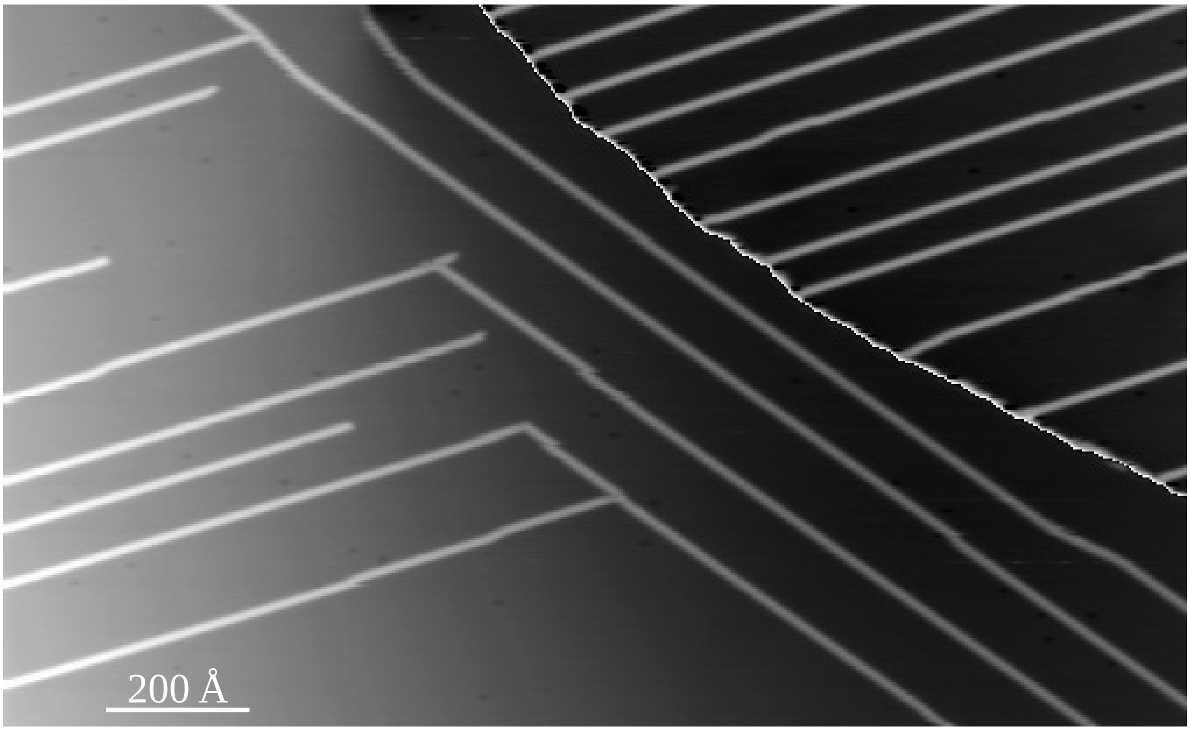

Figure 4.2: Parallel stripes evolve when thermal energy is augmented by adsorption or annealing at 300 K (measured at 77 K). Despite the large interrow distances of about 200 Å, neighboring rows are aligned parallel. The same greyscale range is used on both terraces and the atomic step thus appears as white line in the upper right corner of the STM image.

smoothness of the close-packed substrate geometry and the weak bonding between the adsorbate and the noble metal surface. Up to five molecular endgroups interact in one junction. MD-simulations elucidating the energetics of the bonding are discussed in Section 4.2. The observed growth scenario can be considered as diffusion-limited aggregation of rod-like particles subject to anisotropic interactions. Accordingly, the irregularity of the formed agglomerates suggests that their shape is due to kinetic limitations whereby thermal equilibrium is not attained.

As shown in Fig. 4.2, parallel molecular stripes evolve on the Ag(111) surface when the thermal energy is augmented by adsorption or annealing at 300 K (measured at 77 K). In agreement with the threefold symmetry of Ag(111), three rotational domains exist on the surface (two domains are present in the area depicted in Fig. 4.2). The distance between neighboring rows is in the order of 200 Å and the parallel alignment over this length scale is exceptional.

With increasing coverage, a highly regular one-dimensional supramolecular nanograting evolves. The domain depicted in Fig. 4.3(a) extends over two terraces separated by an atomic step. Whereas most stripes end at the step edge, the *direction* of the

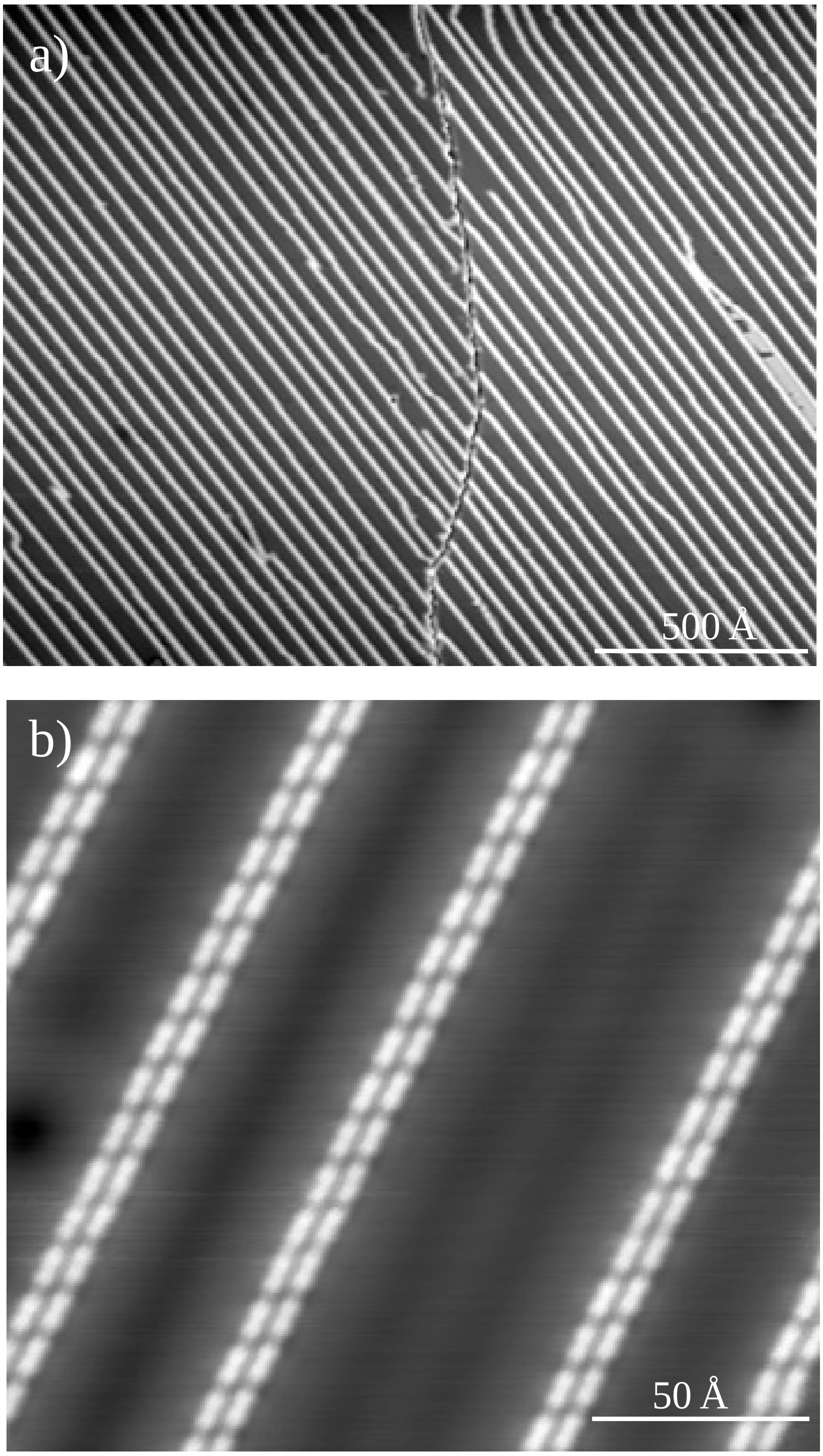

Figure 4.3: Formation of a one-dimensional supramolecular PVBA superstructure by H-bond mediated self-assembly on the Ag(111) surface at 300 K (measured at 77 K). **(a)** A large-scale STM topograph of a single domain extending over two terraces demonstrating ordering at the μm-scale (the same greyscale range is used on both terraces and the atomic step thus appears as white line in the middle of the STM image.). **(b)** A close-up view of the self-assembled twin chains reveals that they consist of coupled PVBA rows.

stripes is maintained (some stripes even directly continue on the other terrace). Such domains typically extend in the μm-range! Small terraces are nearly empty demonstrating migration over step edges at room-temperature. STM measurements performed at *room-temperature* show one-dimensional features along the same direction. No stable tunneling conditions are obtained and it cannot be distinguished if the fuzzy images are due to intrinsic or tip induced molecular motion at the surface. To determine the stability of chains and to investigate possible phase transitions other techniques, e.g., scattering experiments may be helpful.

A close-up view of some molecular stripes is reproduced in Fig. 4.3(b) revealing that the one-dimensional superstructure consists actually of PVBA twin chains. They run straight along a $<11\bar{2}>$-direction of the Ag-lattice and the molecular axis are oriented along the chain direction, in agreement with the expected formation of hydrogen bonds between the PVBA endgroups. Although atomic resolution of the close-packed Ag surface is routinely achieved with the STM employed for this study, simultaneous resolution of the substrate atomic lattice and imaging of the molecules is generally not possible. For a given tip apex the molecules are moved when tunneling parameters necessary for atomic resolution imaging of the substrate are employed. The chain orientation is determined by changing the tunneling parameters while recording an image and thus switching from atomic resolution to molecular imaging within one STM topograph. The dark lines between PVBA chains in Fig. 4.3(b) are interpreted as an electron standing wave pattern. The *s-p* derived surface-state-electrons of Ag(111) can be regarded as free two-dimensional electron gas, which is scattered at defects, e.g., adatoms or atomic steps. Similarly to the confinement of electrons in a resonator formed of two atomically parallel step edges investigated by Bürgi *et al.* [80, 107], the electrons are confined by the molecular twin chains.

The extreme stability of the low-temperature STM [79,108] allows for the elucidation of exquisite chain details. This is demonstrated by the high-resolution data in Fig. 4.4. The chain periodicity is determined to $p = 15.0$ Å, i.e., $p = 3\sqrt{3}a$ where $a = 2.89$ Å is the Ag(111) surface lattice constant. The PVBA rows within the twin chains are shifted by $\Delta p \approx 3.7$ Å with respect to each other. This suggests an intricate coupling mechanism between adjacent rows, which have a distance of $d \approx 2.4a = 6.9$ Å.

A slight asymmetry of the molecules becomes apparent in the topograph in Fig. 4.4(a), i.e., in the upper row the right lobes of all molecules appear oval, in contrast to the round shape of the left lobes. This inequality is elucidated by the STM contour lines in Fig. 4.4(b). The longer, oval lobe is associated with the PVBA benzoic acid moiety. Consequently, there is indeed a head-to-tail coupling of PVBA in the chains.

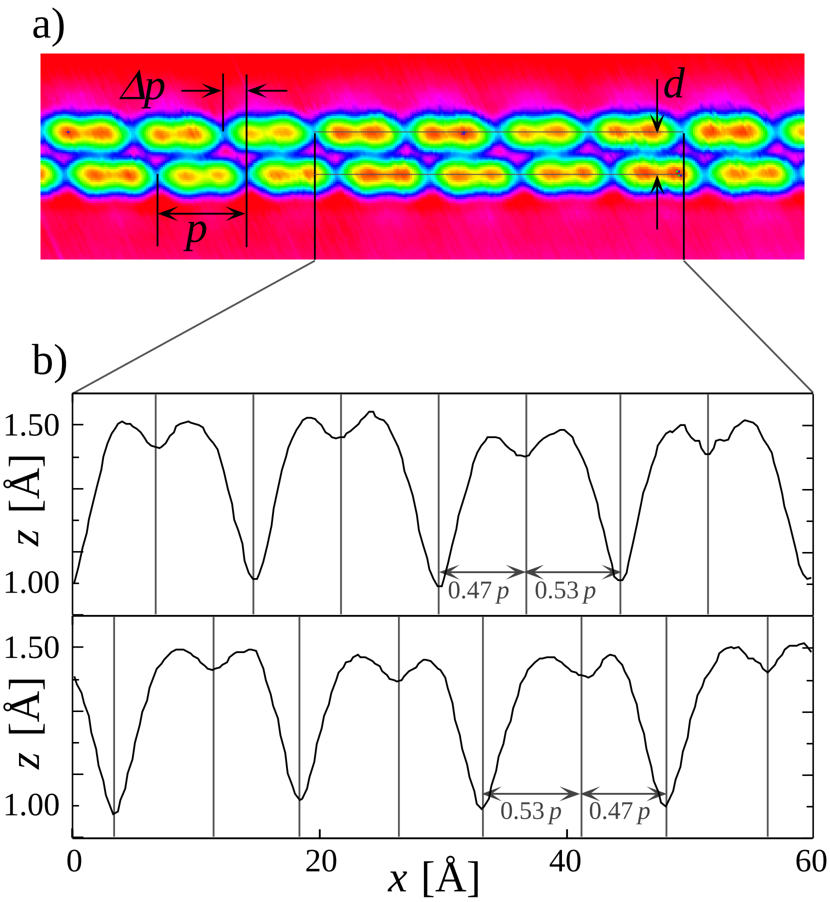

Figure 4.4: High-resolution STM data of a PVBA twin chain. **(a)** The chain periodicity p in a <11$\bar{2}$>-direction is $3\sqrt{3}a = 15$ Å, the PVBA interrow distance d is $\approx 2.4a = 6.9$ Å. **(b)** The STM contours along the lines indicated in (a) demonstrate the head-to-tail coupling of the PVBA molecules along the rows and the antiparallel molecular alignment in adjacent rows.

Furthermore the data reveal that in the lower PVBA row the left lobe of all molecules is more extended, just opposite to the configuration in the upper row. Therefore the molecules in adjacent rows exhibit antiparallel alignment.

The observed features of the supramolecular structure are rationalized by the model proposed in Fig. 4.5(a), where a montage of an Ag(111) atomic resolution image with a self-assembled twin chain drawn to scale is shown.

The orientation of the molecular chains reflects a good match of PVBA subunits with high-symmetry lattice positions. This accounts also for the chain periodicity being a multiple of Ag lattice units. Assuming an unrelaxed molecular configuration,[1] the length of the OH$\cdots$N hydrogen bond is 2.5 Å. This distance is larger than those of similar type H-bonds in crystals of nucleic acid components and isonicotinic acid

---

[1] The geometry of the molecule has been calculated *ab initio* by density functional theory (DFT).

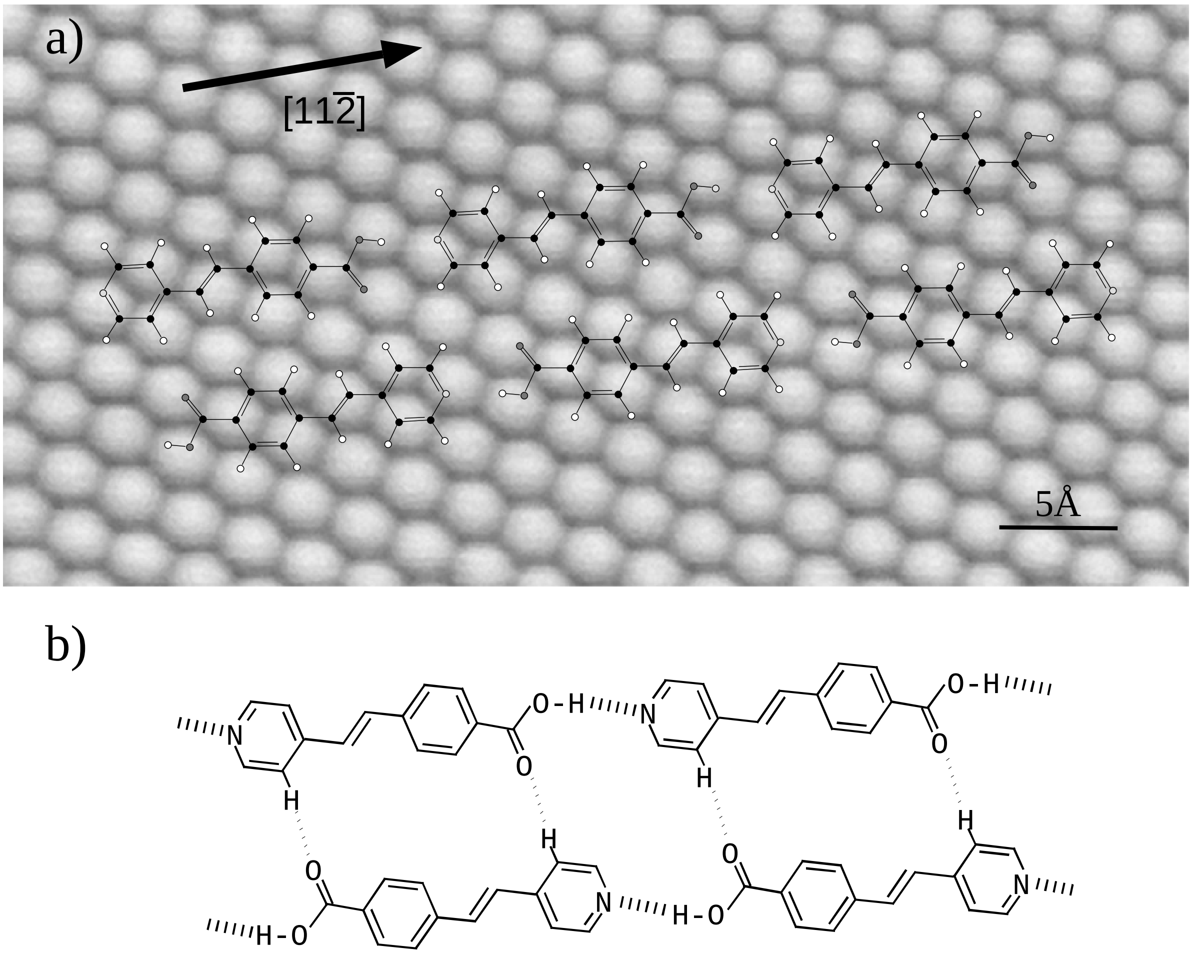

Figure 4.5: (a) Montage of an Ag(111) atomic resolution image with a proposed model of the self-assembled PVBA twin chain to scale illustrating the match of molecular geometry and substrate lattice. **(b)** Repeat motif of the PVBA supramolecular twin chains with moderate OH$\cdots$N and possible weak CH$\cdots$OC hydrogen bonds indicated.

(a lower analogue of PVBA), where values in the range of 1.5–2.1 Å exist [109, 110]. Nevertheless, the proximity of the coupled groups can be associated with the formation of moderate H-bonds (cf. the illustration of the twin chain repeat motif sketched in Fig. 4.5(b)) [111]. Note that the presence of the metal surface electrons might sensitively influence the hydrogen bonding. Proton transfer did not occur with PVBA in crystallites, as demonstrated by solid state ^{15}N-NMR [38]. This is in agreement with *ab initio* calculations for a twin chain in vacuum presented in Section 4.2. The coupling of the PVBA in adjacent rows is associated with weak intermolecular attractions. The antiparallel alignment and the relative displacement allow for a complementary assembly of two equivalent PVBA molecules, which are accommodated in similar adsorption geometries. In addition to the expected electrostatic interactions between the polar molecules, a weak CH$\cdots$OC hydrogen bonding is feasible. The corresponding CH$\cdots$OC distance is approximately 2.9 Å, close enough for a weak coupling [112]. The geometrical arrangement is a compromise between the lateral intermolecular interaction and the bonding to the substrate. Due to the interrow distance of $2.4a$ there is a slight outward relaxation of the rows away from the centers of the substrate hollow-site positions. This relaxation and the suggested inward orientation of the C=O group prevent from two-dimensional growth and thus account for the directional twin chain self-assembly. The rather regular mesoscopic ordering of the supramolecular chains into a grating, reminiscent of surface strain relaxation induced mesoscopic superstructures [113, 114], can be rationalized by the operation of repulsive electrostatic interactions between the twin chains [115].

There is a distinct directional shift in the twin chains, i.e., in the data presented so far it is always the right PVBA-row which appears to be displaced by Δp in the chain direction, and the supramolecular assembly is thus enantiomorphic. Due to the angled molecular structure two chiral species exist for PVBA adsorbed on a surface (disregarding the asymmetry of the carboxylic acid group which freely rotates in the gas phase and is expected to be able to flip on the surface). Whereas the chirality of twin chains is clearly discernible, our STM images do not yield a direct distinction of chiral molecular species. The observation of enantiomorphic supramolecular structures alone does not prove chiral phase separation [2]. From a geometrical model regarding the findings of STM, i.e., periodicity, surface direction, interrow distance, shift and the calculated molecular structure it is evident that steric effects favor twin chains built with only one enantiomer. Thus only one enantiomer is used in the model depicted in Fig. 4.5. With the mirror-enantiomer just the opposite shift is encountered and was indeed observed. Such a mirror twin chain is depicted in Fig. 4.6 together with the corresponding model. MD-simulations reveal that possible arrangements with a combination of different enantiomers are feasible but they lead to energetically less favorable structures (cf. Section 4.2). A striking phenomenon is that for domains extending in the μm-range all parallel twin chains are of the same chirality. In Section 4.2 a growth model is proposed explaining this phenomenon.

The mutual repulsions between twin chains are reflected in a coverage dependent series of STM topographs. Two STM images with a coverage of $\theta = 0.021$ and $\theta = 0.043$ are reproduced in Figs. 4.7(a) and (b), respectively ($\theta = 1$ corresponds to 1 PVBA molecule per Ag surface atom, a densely packed twin chain film to $\theta = 0.070$.). We have performed a statistical analysis of twin chain distances at four different coverages. For each coverage several STM images (50×50 Å^2) from different surface areas are evaluated.

---

[2] An example of achiral molecules aggregating into chiral supramolecular structures is the PEBA/Ag(111) system discussed in Chapter 6.

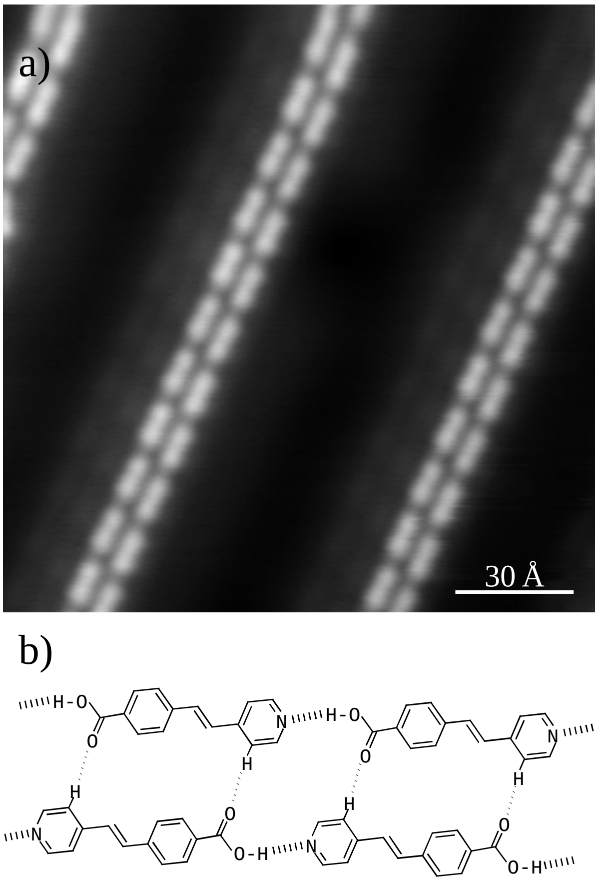

Figure 4.6: Mirror domain to the twin chain shown in Fig. 4.3(b) demonstrating the segregation of enantiomorphic supramolecular structures in domains (adsorbed at 300 K, measured at 77 K). Whereas in Fig. 4.3(b) it is always the right PVBA-row which appears to be displaced by Δp in the chain direction, here just the opposite shift is found. **(b)** Repeat motif of the PVBA supramolecular twin chains using the mirror-enantiomer.

The uncertainty of the determined distances in this length scale is less than 1 Å. The statistical distribution shows that the scattering of the distances is strongly dependent on coverage. The normalized standard deviation [3] is (0.30 ± 0.10) at a mean twin chain distance of 56 Å ($\theta = 0.017$) and reduces to (0.11 ± 0.02) at a mean twin chain distance of 22 Å ($\theta = 0.043$). Thus the spacing becomes nearly equidistant at higher coverage. Note, however, that the relative arrangement of neighboring twin chains along the chain direction is not uniform but they have a random offset. Figs. 4.7(c) and (d) show the statistical analysis corresponding to the situations in STM topographs (a) and (b), respectively. The interrow spacing at the highest coverage (cf. Fig. 4.7(b)) is smaller than the length of a PVBA molecule and the entire surface is still exclusively covered with twin chains, no triple chains or islands of more coupled chains exist. Note that all

---

[3] standard deviation divided by the mean distance

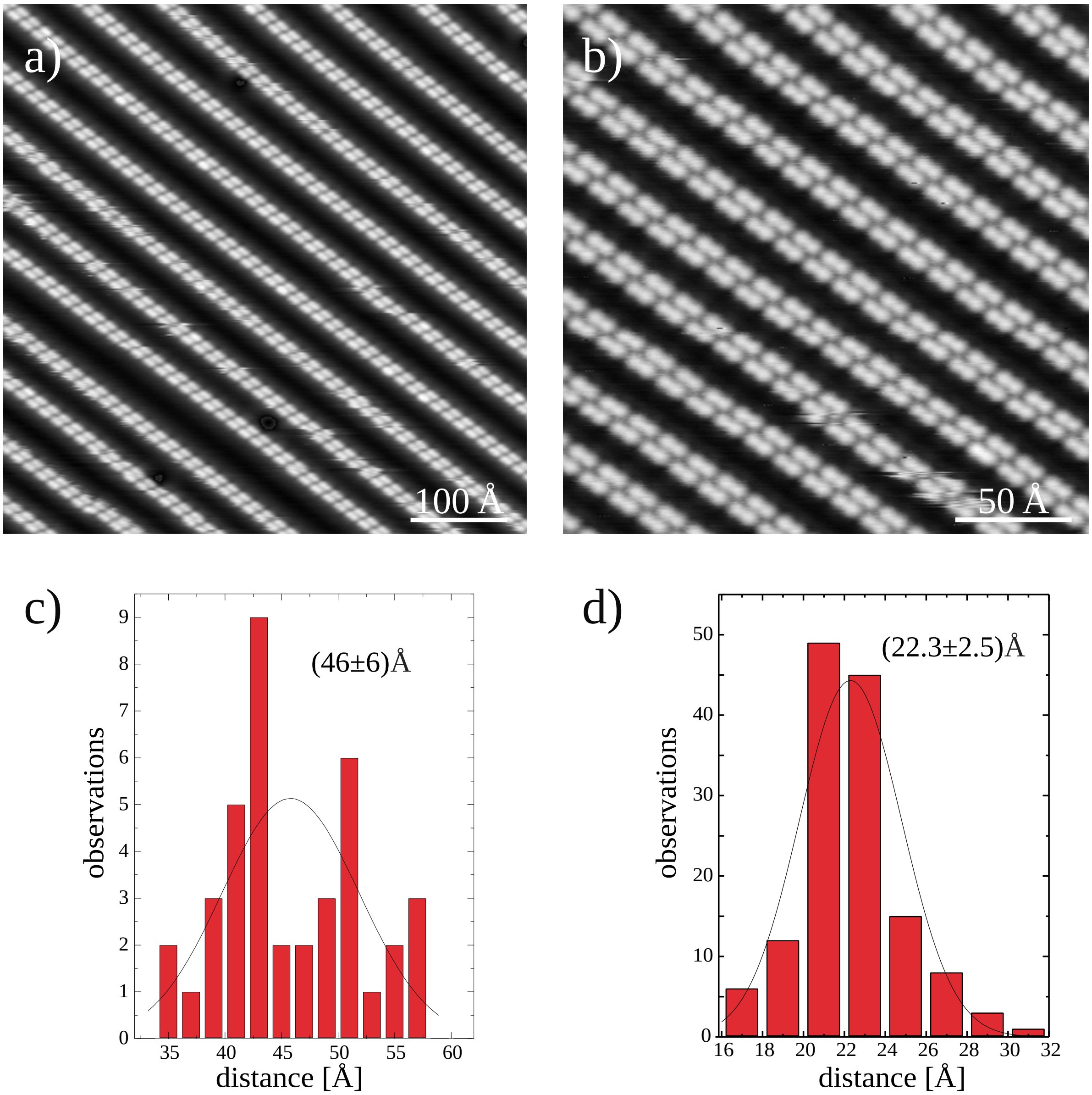

Figure 4.7: PVBA on Ag(111) adsorbed at 300 K (measured at 77 K) with **(a)** $\theta = 0.021$ and **(b)** $\theta = 0.043$ ($\theta = 1$ corresponds to 1 PVBA molecule per Ag surface atom). In **(c)** and **(d)** the corresponding statistical analysis of twin chain distances is plotted. The spacing of twin chains becomes nearly equidistant at higher coverage.

twin chains in the two domains depicted in Figs. 4.7(a) and (b) are of the same chirality, the mirror species of the one in Fig. 4.3.

Spontaneous formation of periodic domain structures was reported by Kern *et al.* for oxygen on Cu(110) [114]. They observed a periodic domain pattern (periodicity ∼100 Å) consisting of alternating stripes of clean Cu(110)(1×1) and (2×1)Cu-O added row areas for subsaturation oxygen coverages on Cu(110). Vanderbilt explained the mesoscopic ordering by elastic and electrostatic interactions [115,116]. Surface strain effects are well known to result in the formation of domain structures [117–120] when the energy gained from elastic relaxation in the presence of domains pattern is sufficient to overcome the cost of the resulting domain boundaries. Vanderbilt demonstrated that work function variations at a metal surface can lead in principle to the same kind of instability towards domain formation. Since the electrostatic potential in the metal is constant, the potential just outside the surface will have a discontinuity across each domain boundary, giving rise to fringing electric fields. While it might be thought that the presence of such fields would raise the energy of the system, it can be shown instead that domain formation leads to a *net energy reduction* when surface terms are properly taken into account. The similarity between the theory of elastic and electrostatic effects can be traced to the fact that both the elastic interaction between surface stress elements, and the electrostatic interaction between surface dipoles, have an identical $1/\mathrm{r}^3$ scaling. A variety of geometries have been considered, but a simple striped phase is found to be energetically favored under most conditions. Thus, as long as the work function difference between two phases does not vanish identically, the theory predicts that *periodic domain formation may spontaneously occur*. The Vanderbilt model explains the experimentally observed periodicity for the system O/Cu(110), where domain boundaries *per se* are energetically unfavorable. For PVBA on Ag(111) the intricate coupling mechanism of PVBA molecules results in twin chains being energetically favored and thus there is no energy cost for the formation of domain boundaries. Accordingly the twin chains evolve as an intrinsic property of the system already at the lowest coverages and persist whenever sufficient space is available. Nevertheless, the Vanderbilt model shows that mesoscopic ordering might be mediated by electrostatic interactions. For the O/Cu(110) system the relative contributions of electrostatic and elastic interactions remain to be clarified and an experimental proof for a purely electrostatic ordering is still missing [115].

We have quantified the electrostatic interactions between twin chains adsorbed on a metal surface within the framework of MD-simulations (cf. Section 4.2). Briefly, the charge distribution of PVBA in vacuum is calculated *ab initio* by density functional theory and the metal surface is accounted for via induced image charges. The twin chain configuration is found to be stable and between twin chains repulsive electrostatic interactions operate. The electrostatic energy per chain-segment of two relaxed PVBA twin chains as a function of twin chain distance is plotted in Fig 4.8. Apparently the electrostatic energy rapidly decreases with distance. Whereas at 15 Å, corresponding to nearly attached twin chains [4], the energy amounts to 12.8 meV per chain-segment, at

---

[4] Note that the center-center distance is defined as twin chain distance, not the interrow distance.

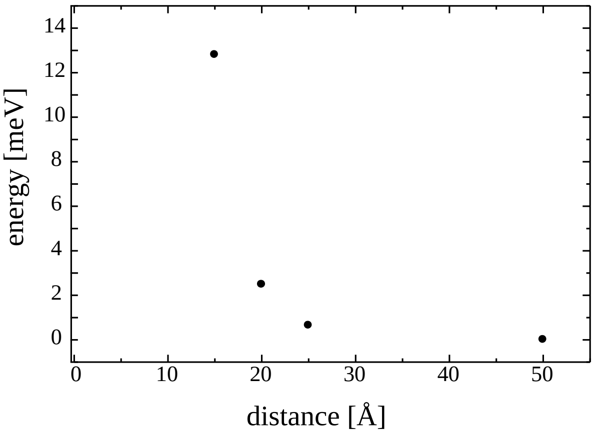

Figure 4.8: Energy per chain segment as a function of twin chain distance due to repulsive electrostatic interactions as determined by MD-simulations. Note that the center-center distance is defined as twin chain distance and a value of 15 Å corresponds to nearly attached twin chains.

20 Å it is merely 2.5 meV and at 25 Å a value of 0.6 meV is calculated.

An additional contribution to the system energetics results from the confinement of surface state electrons by the molecular twin chains (cf. Fig. 4.3(b)) which might lead to repulsive interactions. Currently, investigations elucidating this phenomenon are in progress. For CO adsorbed on Ag(111) surface state mediated repulsive intermolecular interactions have been reported by Briner [121].

Upon further increasing the coverage, twin chains coexist with three or more coupled chains as illustrated in Fig. 4.9(a). Space limitations become appreciable and the energy gain due to bonding to the substrate of arriving molecules overbalances the repulsive interactions between twin chains. Whereas the distinct shift of twin chains is always maintained in triple chains, the lateral ordering is lost when more chains attach. With increasing coverage "islands" grow in size, which finally leads to a structure as depicted in Fig. 4.9(b) for the monolayer. Molecules are still aligned along a <11$\bar{2}$>-direction and the periodicity within the rows is maintained. However, no regular 2D superlattice is formed. There is no distinct shift between adjacent molecular rows and the typical twin chain feature disappears. For some organic compounds, normally planar and rodlike molecules, there are thermodynamically stable phases in a well-defined temperature interval between the crystalline and liquid state of aggregation. The monolayer structure of PVBA on Ag(111) resembles the smectic phase of such liquid crystals, where molecules are arranged in parallel layers without lateral order. However, in the smectic phase molecules are mobile within a layer. In contrast, in the PVBA monolayer molecules are immobile and the structure is thus a static arrangement. Due to the slight

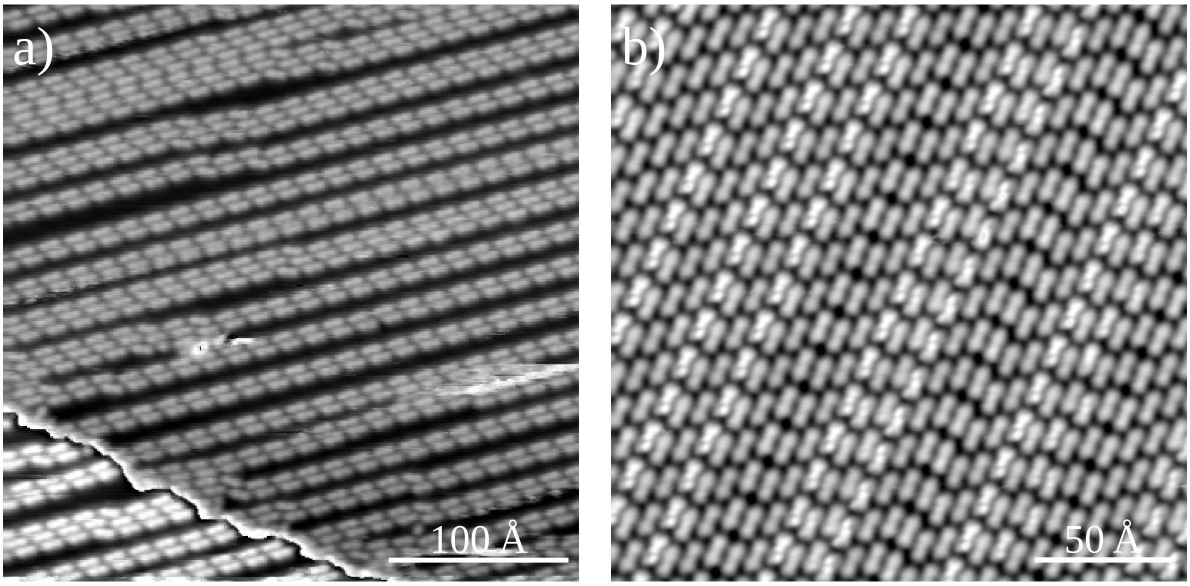

Figure 4.9: Equilibrium structure of high coverage phases of PVBA on Ag(111) (adsorbed at 300 K, measured at 77 K). **(a)** Twin chains coexist with three or more coupled rows. Whereas the distinct shift of the twin chains is maintained in triple chains, the lateral ordering is lost when more chains attach. **(b)** Monolayer structure of PVBA on Ag(111). The periodicity within the rows is maintained. Due to lattice mismatch between overlayer and substrate, some molecular rows are presumably displaced vertically in order to reduce strain and thus appear brighter in STM images.

lattice mismatch between overlayer and substrate, some molecular rows are presumably displaced vertically in order to reduce strain and thus appear brighter in STM images.

4.2 Molecular dynamics simulations

We model the intermolecular interactions with a classical force field and use molecular dynamics (MD) to find the stable structure [5]. The electrostatic potential of an isolated PVBA molecule in vacuum is calculated *ab initio* by density functional theory (DFT). Due to the characteristics of the carbon bonds involved, the molecule can be considered being flat and thus a planar geometry is enforced during the relaxation. Point charges are determined located on the C, N, O and H atoms providing a best fit for the calculated potential outside the van der Waals exclusion area (cf. Appendix A). The average error of the fitted potential is estimated to ~5% in the relevant region of space [122]. The resulting intermolecular force field includes the electrostatic interactions and the repulsive

---

[5] Simulations have been performed in cooperation with Dr A. De Vita at the Institut Romand de Recherche Numérique en Physique des Matériaux.

short range potential as given by hard spheres centered on the C, N and O atoms with a van der Waals radius of 1.9 Å, for the H atoms no van der Waals radius is chosen. Similar force fields have been successfully applied to a variety of hydrogen bonded systems [123]. Electrostatic screening of the metallic substrate is accounted for via image charges. The distance between charges and image charges is set to 7.0 Å. The PVBA molecules are free to move parallel to the model surface. The time scale per step in the MD-simulation is about 1 fs, thus a time range in the order of 0.1 ns can be simulated within an acceptable computing time. Meaningful initial configurations need thus to be selected and only the final relaxation is simulated. Repeated simulations with varied initial configurations ensure that the *absolute* energy minimum is reached.

As a first step we have modeled the coupling of two molecules, i.e., head-to-head and head-to-tail hydrogen bonding. In Fig. 4.10(a) the relaxed configuration of a head-to-head bonding is reproduced. Two $\mathrm{OH}\cdots\mathrm{O}$ hydrogen bonds with an identical distance of 2.7 Å are formed. The binding energy of this configuration is 91 meV per molecule, simulations with different enantiomers show that energy differences are rather small (about 4 meV). The second preferred configuration of two molecules is depicted in Fig. 4.10(b). Here the molecules form a head-to-tail hydrogen-bond with a $\mathrm{OH}\cdots\mathrm{N}$ length of 2.6 Å and a $\mathrm{CH}\cdots\mathrm{O}$ bond with the α-pyridil H atom (2.8 Å). This bond distance is comparable to the one of the $\mathrm{OH}\cdots\mathrm{N}$ head-to-tail bonding in twin chains (2.5 Å). The molecular axis are not parallel but slightly rotated to optimize the bonding with the α-pyridil H atom. The binding energy is with 71 meV per molecule significantly smaller than in the case of head-to-head bonding. Note, however, that in supramolecular assemblies the head-to-tail bonding allows the repeated linking of molecules and each molecule is thus participating in *two* bonds resulting in a higher overall binding energy. In contrast, an assembly of two head-to-head coupled molecules cannot be periodically linked. To elucidate the coupling in junctions of several molecules, as present in low temperature deposited PVBA networks (cf. Fig. 4.1), the binding of three molecules has been simulated. A relaxed configuration is depicted in Fig. 4.10(c). Three $\mathrm{OH}\cdots\mathrm{O}$ hydrogen-bonds with an identical length of 2.7 Å as in the case of head-to-head bonding are formed. The binding energy per molecule is 96 meV, slightly larger than in the case of a linear head-to-tail bond between two molecules. Again, such a complex cannot be continued in periodic structures.

In a second step we have addressed the stability of twin chains. Simulations have been performed for various combinations of enantiomers. The length of calculated twin chains is varied between 5 and 8 segments (corresponding to 10 to 16 molecules). From this, the binding energy per molecule is determined by subtracting the energies of consecutive

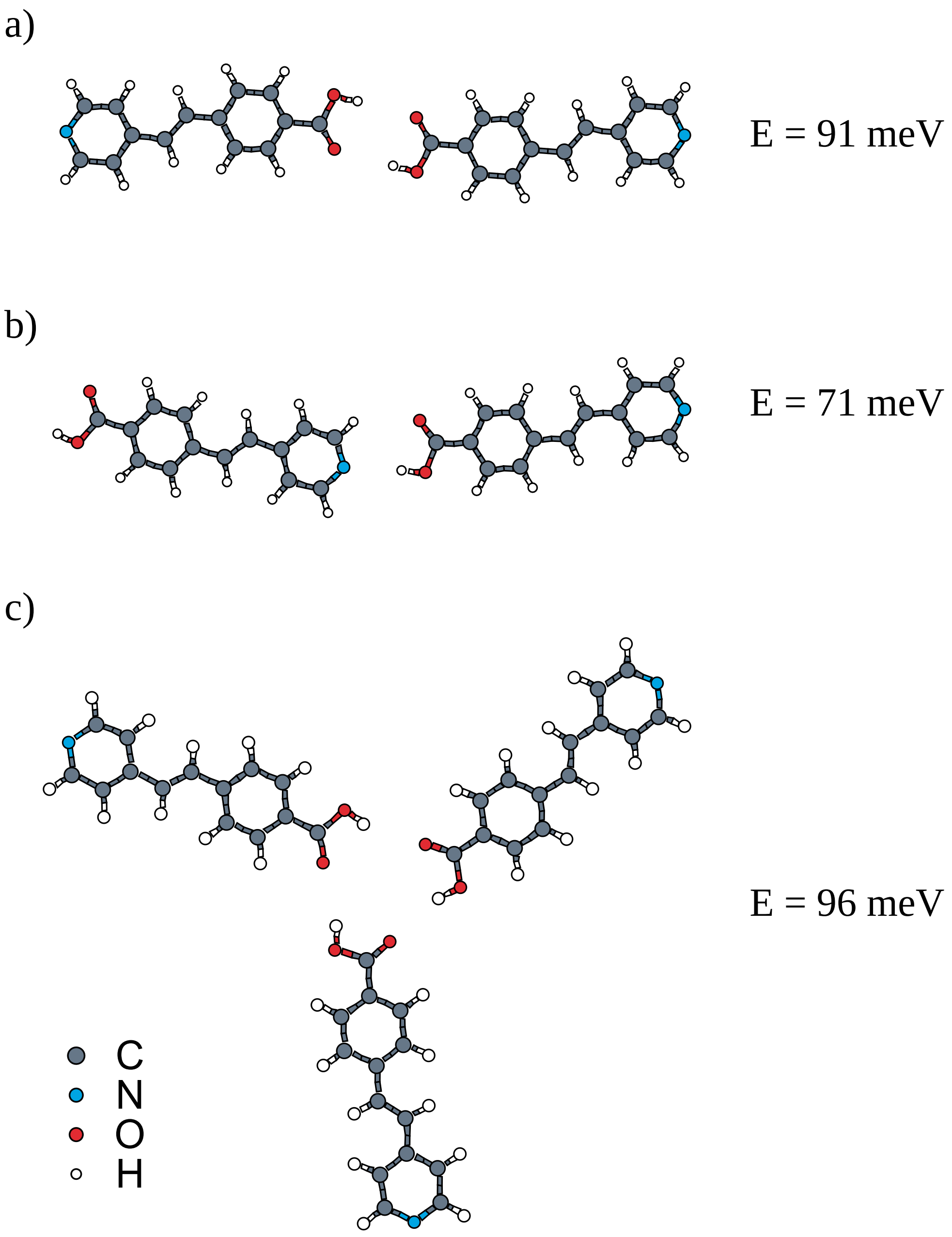

Figure 4.10: Relaxed bonding configuration and corresponding binding energy as determined by MD-simulations of:

(a) A pair of head-to-head coupled molecules

$\Longrightarrow$ two OH$\cdots$O bonds of 2.7 Å, binding energy per molecule 91 meV.

(b) A pair of head-to-tail coupled molecules

$\Longrightarrow$ OH$\cdots$N bond of 2.6 Å + CH$\cdots$O bond with the α-pyridil H atom of 2.8 Å, binding energy per molecule 71 meV.

(c) A junction of three molecular head groups

$\Longrightarrow$ three OH$\cdots$O bonds of 2.7 Å, binding energy per molecule 96 meV.

chain lengths. We find that the difference energies convert rapidly for the calculated lengths. The multitude of possible combinations of chiral molecular species is drastically reduced by the following considerations: Firstly, high resolution STM data reveal that all molecules inside a row are pointing in the same direction and adjacent rows are aligned antiparallel (cf. Fig. 4.4). Secondly, adjacent rows are linked via CH$\cdots$O bonds and thus only twin chain configurations with the C=O group of all molecules pointing inward the twin chain are acceptable. In view of these results only combinations of two compatible enantiomers are feasible (regarding the asymmetry of the vinyl-bridge *and* the carboxylic acid group *four* species of PVBA are present on the surface). To each twin chain configuration built of two corresponding enantiomers, a mirror twin chain exists built of the corresponding mirror enantiomers. In our model the metal substrate is accounted for via image charges and thus the virtual surface is a mirror plane. Therefore twin chains are energetically identical to their mirror twin chains. This restricts the number of required enantiomers to two, which will be referred to as species α and β. Twin chains are built by repetition of a basis containing up to four molecules, i.e., two molecules per row. The three possibilities for a two-molecule basis are the following: $\alpha\alpha$, $\beta\beta$ and $\alpha\beta$. The relaxed configurations of the respective two-molecule basis twin chains are represented in Figs. 4.11(a), (b) and (c).

Neither the shift of adjacent rows nor the rotation of the molecular axis away from the chain axis of the twin chains depicted in Figs. 4.11(b) and (c) matches the STM observations. In contrast, the calculated geometry of Fig. 4.11(a) closely resembles the STM data. The periodicity amounts to 15.1 Å in agreement to the value determined by STM (15.0 Å). The relative shift of adjacent rows is determined to 3.7 Å from STM images. The main part of the tunneling current is from the π-system of the molecule, but the contribution of the carboxylic acid group is not exactly known. These complications involved in the imaging of PVBA prevent for the direct comparison between observed and modeled shift. In the relaxed configuration, however, we find the N atom shifted by 4.2 Å with respect to the carboxylic acid C atom of the neighboring molecule in the adjacent row which agrees with the shift of 3.7 Å from STM. The binding energy per molecule amounts to 169 meV for the twin chain depicted in Fig. 4.11(a), slightly but significantly larger than 163 meV and 165 meV for the configurations shown in Figs. 4.11(b) and (c), respectively. Twin chains with a two-molecule basis have a significantly lower binding energy and the match with the observed STM images is poor. Thus the MD-simulations confirm that the chirality of twin chains is directly associated to the chirality of single molecules and twin chains exclusively consisting of one chiral species are energetically favored.

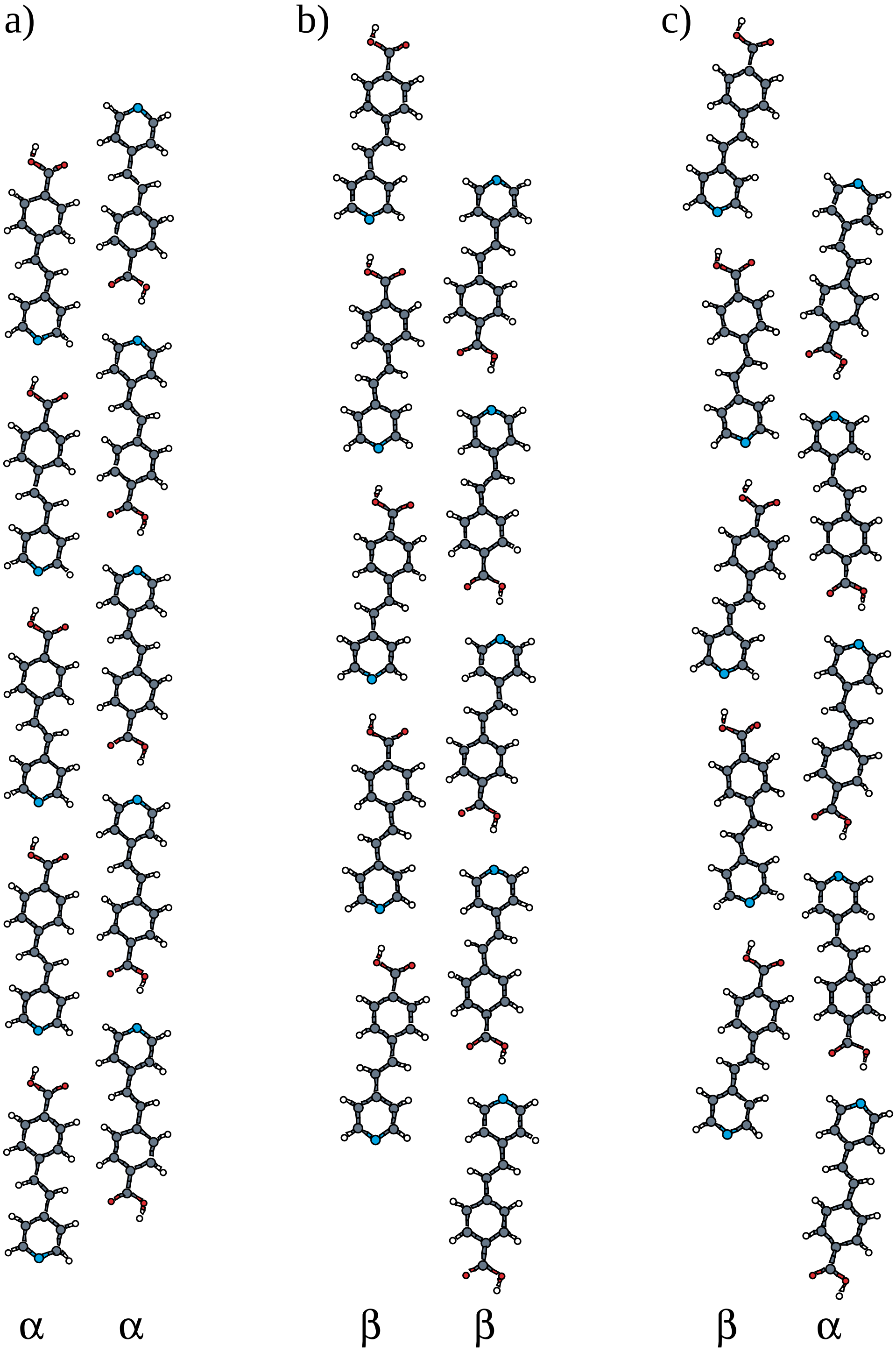

Figure 4.11: Relaxed configurations of all energetically different twin chains consisting of a two-molecule basis as determined by MD-simulations. **(a)** Both molecules of chiral species α, **(b)** both molecules of chiral species β, and **(c)** one molecule of chiral species α and one of chiral species β.

Pasteur already discovered in 1848 that chiral discrimination between mirror-image stereoisomers can lead to the spontaneous separation of a racemic mixture into enantiomerically pure phases [124]. In a molecular scale analogue Böhringer *et al.* used a scanning tunneling microscope to discriminate and separate a racemic mixture of 1-nitronaphtalene clusters [125]. In three dimensions, however, most racemic mixtures crystallize as racemates with the unit cell composed of an equal number of molecules with opposite chirality or as random solid solutions. It was originally proposed by Stewart and Arnett that confinement in two dimensions enhances chiral discrimination between enantiomers [126]. Most racemic 2D systems investigated so far, with respect to spontaneous breaking of mirror symmetry, are Langmuir films of amphiphilic molecules with one or more asymmetric carbon atoms [126–131]. Atomic force microscopy (AFM) observations by Eckhardt *et al.* of enantiomorphic supramolecular structures evolving from a racemic mixture of a chiral amphiphile have been interpreted in terms of chiral segregation [128]. In a recent publication, Böhringer *et al.* report a coverage driven chiral phase transition [132]. In their STM study they investigated 1-nitronaphtalene evaporated on a Au(111) surface. High resolution STM images directly reveal the chirality of the adsorbed molecules. At low coverage, clusters consisting of a well-defined number of both enantiomers are found, at higher coverages chains evolve consisting only of one chiral species [25]. In our study, the chirality of twin chains is clearly discernible but the direct determination of molecular chirality is not possible. In the PEBA/Ag(111) system achiral molecules aggregate into enantiomorphic supramolecular structures (cf. Chapter 6). Thus the observation of chiral supramolecular structures alone does not prove chiral phase separation. For PVBA on Ag(111), twin chains built of only one enantiomer match better due to stereochemical effects. The presented MD-simulations accordingly reveal that arrangements with a combination of different enantiomers are feasible but lead to energetically less favorable structures.

A striking phenomenon is that for domains extending in the μm-range all parallel twin chains are of the same chirality despite interrow distances in the 100 Å range. Repulsive interactions between neighboring twin chains decrease rapidly and cannot mediate chirality over such large distances. Thus other mechanisms have to be operative. To elucidate the segregation of enantiomorphic supramolecular structures in large domains, the following experiment has been performed: At first, a well-ordered equilibrium structure is prepared showing the typical twin chains in large chiral domains. Subsequently, a small amount of PVBA is evaporated with the Ag(111) surface held at 160 K. The resulting situation is represented in Fig. 4.12(a). Irregular molecular aggregates attach to twin chains. The molecules interact via the endgroups and form

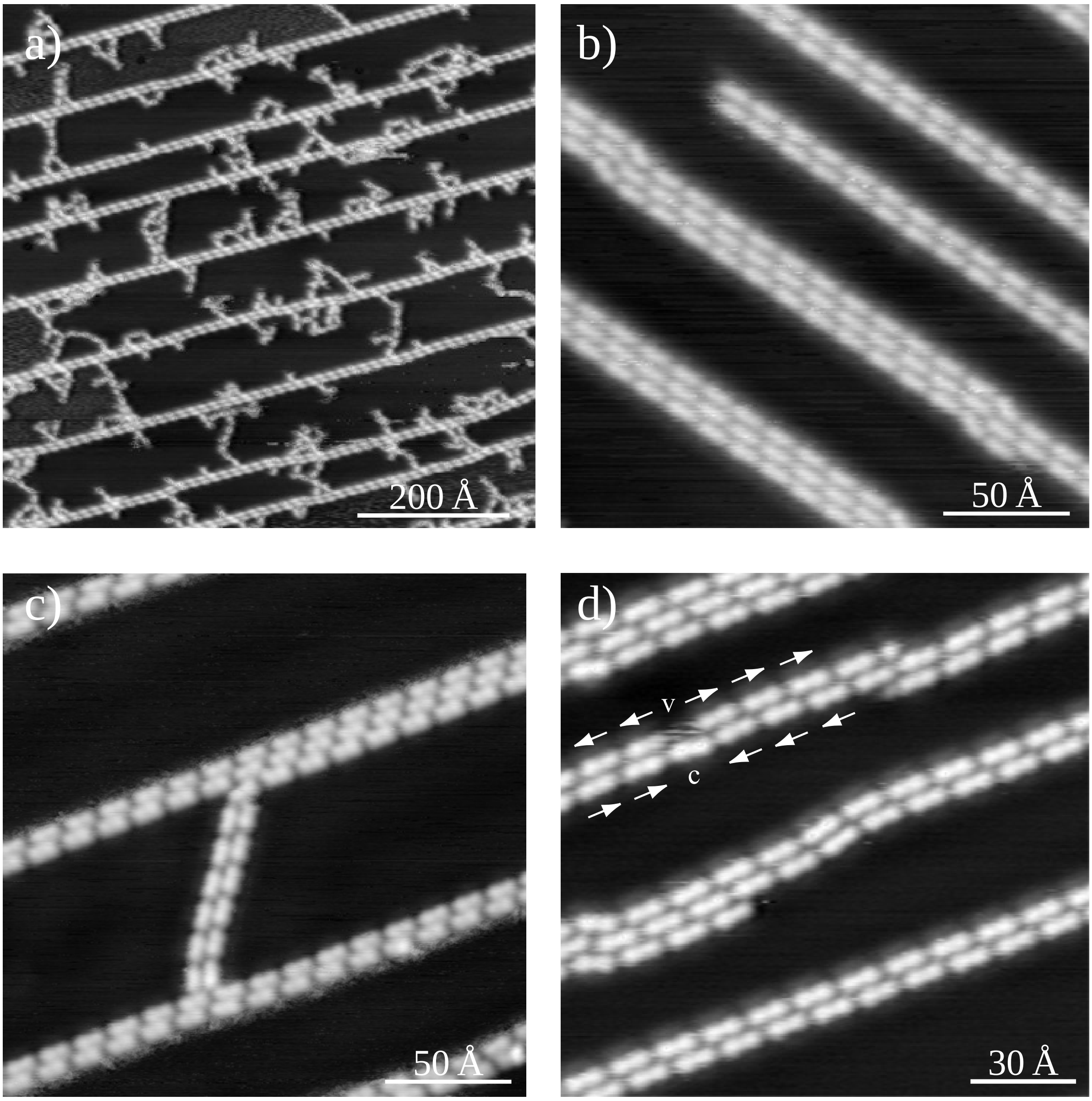

Figure 4.12: *Metastable* structures (measured at 77 K). **(a)** Firstly, well-ordered equilibrium twin chains are prepared and subsequently a small amount of PVBA is evaporated with the Ag(111) surface held at 160 K. **(b-d)** Annealing to 225 K results in different *metastable* structures such as triple chains in the absence of space limitations and chirality switch of twin chains at a vacancy (indicated by v) mediated by a coupling molecule (c) of unknown orientation.

meandering chains already known from low temperature aggregation (cf. Fig. 4.1). Upon annealing this structure to room-temperature, highly ordered twin chains in large chiral domains evolve. In Figs. 4.12(b-d) STM topographs taken after annealing to 225 K for 3 minutes, and thus showing *metastable* structures, are represented (measured at 77 K). Triple stripes are formed in the absence of space limitations. A variety of new features are found in the *metastable* phase unknown from equilibrium. For example, in Fig. 4.12(c) the third row spontaneously ends and a twin chain continues bridging to the neighboring chain. The chirality of a twin chain in the top left corner of Fig. 4.12(d) changes and a vacancy (marked by v) is formed in the upper row. Due to the distinct shift in the twin chains, the orientation of molecules in each row can be deduced and is marked by arrows (arrowheads indicating the carboxylic acid group). The two parts are coupled in the lower row by head-to-head and a head-to-tail bonding, respectively (the orientation of the coupling molecule (marked by c) cannot be determined.). Removing this molecule in the lower row coupling the two twin chains, the two attaching molecules in the upper row would be aligned tail-to-tail and no stable bonding could be formed. Accordingly, such a vacancy which would be in contradiction to our model has never been observed.

In MD-simulations the stability of a third row coupled to a relaxed twin chain, as has been found in the metastable structures, is investigated. The simulations are performed with chain lengths between 5 and 8 molecules and the binding energies are calculated from the converging energetic differences. In Fig. 4.13(a) the relaxed bonding geometry of the energetically most favorable triple chain is depicted. The topmost rows represent an $\alpha\alpha$-twin chain configuration (cf. Fig. 4.11(a)), the third row consists of enantiomers α with O and OH of the carboxylic acid group reversed (species α_{rot}), thus allowing to bind via the C=O group to the twin chain. The binding energy per molecule is calculated to 167 meV, slightly less than for a molecule in an $\alpha\alpha$-twin chain. Since the carboxylic acid group provides only a minor contribution to the tunneling current the shift of adjacent rows in the model is in accordance with the STM data. In contrast, enantiomers β coupled to an $\alpha\alpha$-twin chain result in a relative shift inconsistent with the STM observations and the configuration is energetically less favorable due to stereochemical effects.

A conspicuous phenomenon is, that four attached rows have never been observed during the STM study (neither in the metastable phase nor at high coverage). In Fig. 4.14 an STM image of a nearly completed monolayer is depicted. Twin chains coexist with an area showing the typical monolayer structure (cf. Fig. 4.9). In the upper left corner two twin chains shear out of the monolayer structure. This signals the energetic preference for twin chains which shear out when space is available.

To support this suggestion we performed MD-simulations for coupled rows. They indicate, however, that a fourth row of species α can be attached to $\alpha\alpha\alpha_{\mathrm{rot}}$-triple chains which configuration is depicted in Fig. 4.13(b). Again the bonding is mediated by the C=O group. Since the only difference between species α and α_{rot} is the position of

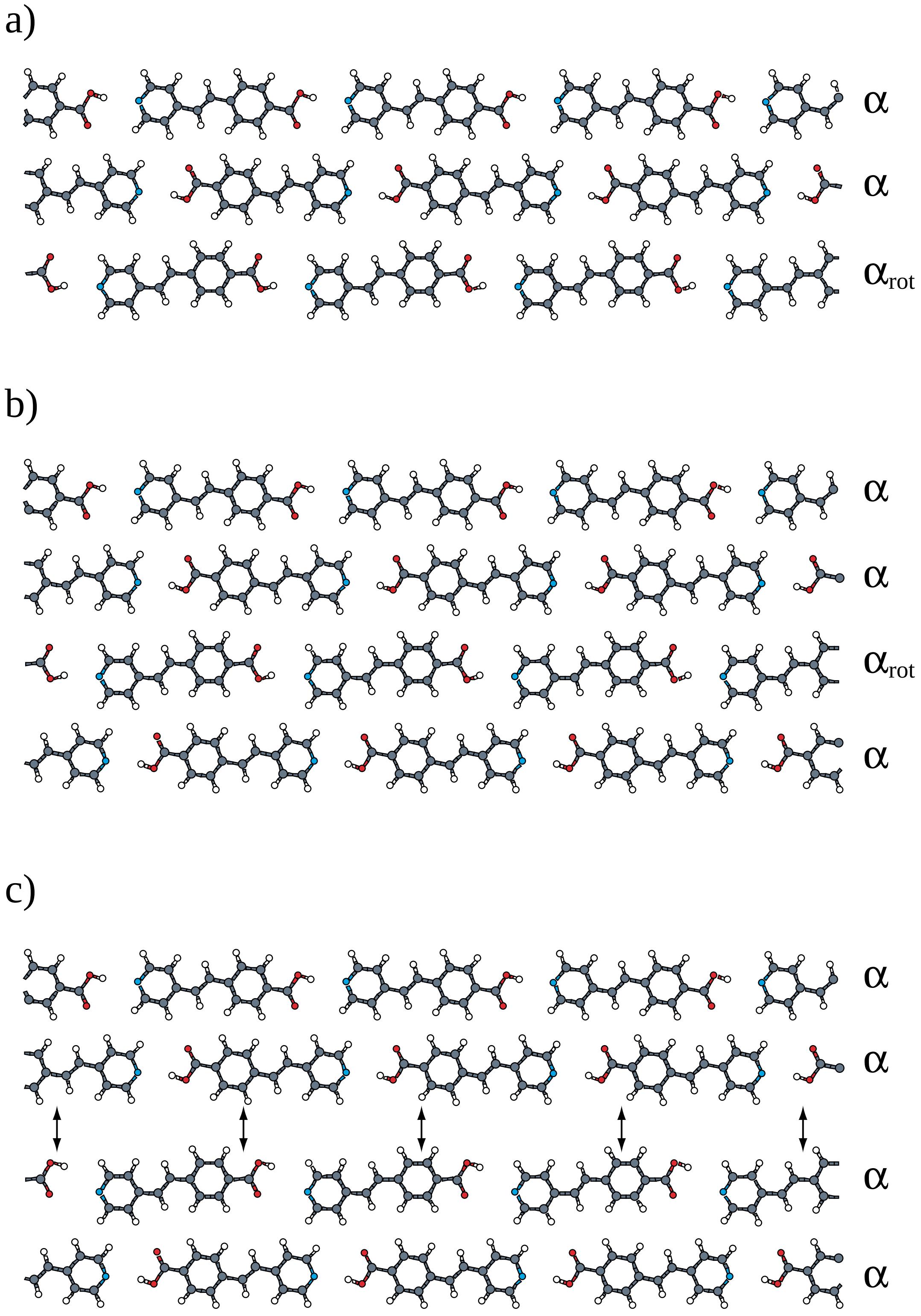

Figure 4.13: (a) Relaxed bonding geometry of $\alpha\alpha\alpha_{\mathrm{rot}}$-triple chain as determined by MD-simulation. **(b)** Fourth row of species α coupled to the triple chain in (a). This configuration is stable, but upon converting the third α_{rot}-row to species α, two $\alpha\alpha$-twin chains remove without breaking apart. This process involves a flipping of the H atom in the carboxylic acid group.

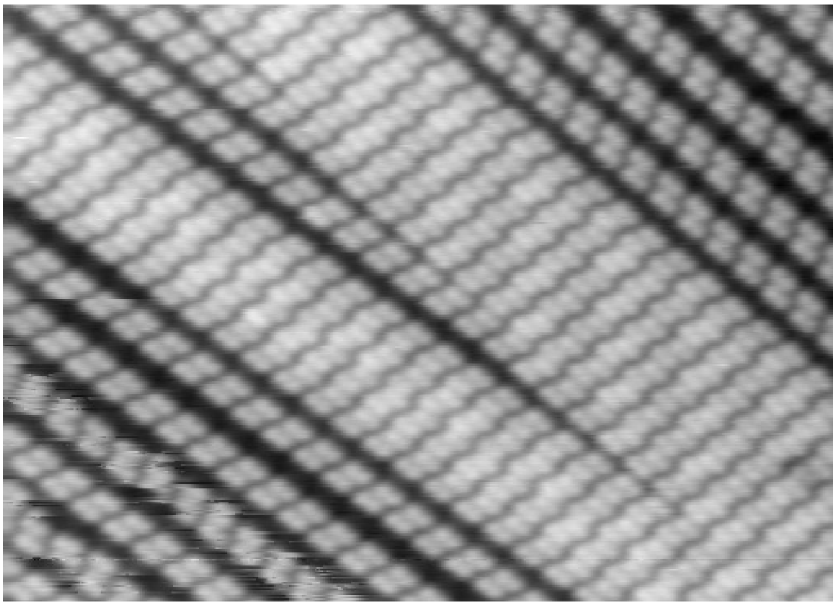

Figure 4.14: STM topograph of a nearly completed monolayer. Twin chains coexist with an area showing the typical monolayer structure. Note that in the upper left corner two twin chains shear out of the monolayer structure once space is available.

O and OH in the carboxylic acid moiety, we allow for a rotation of the carboxylic acid group of the molecules in the third row, i.e., flipping of the corresponding H atom and thus converting species α_{rot} in species α. Note that this is physically reasonable and associated with a phonon-assisted process, well documented for water molecules [133]. Indeed, this configuration is unstable and two $\alpha\alpha$-twin chains remove without breaking apart.

These findings suggest the following growth scenario: The starting point is a racemic mixture of PVBA on the surface. The molecules are highly mobile on Ag(111) at room-temperature. Upon cooling down molecular strings evolve via head-to-tail coupling reflecting the high energy gain in this configuration. This is apparent from low temperature deposited PVBA where linear chains are present in the STM topographs (cf. Fig. 4.1) and from MD-simulations of the intermolecular coupling (cf. Fig. 4.10). The strings must be considered *a priori* as racemic with a stochastic sequence of α and β species. The weak lateral interactions of mobile strings and monomers lead to the formation of twin chain nuclei. Once an $\alpha\alpha$ or $\beta\beta$ nucleus is formed, it rapidly grows in one-dimension with chiral recognition of the respective species. At the same time the nucleus acts as enantioselective catalyst for further formation of isochiral twin chain segments (cf. the discussion in the previous paragraph). This autocatalytic growth and spreading process proceeds from different origins at the surface, which accounts for the coexistence of the distinct chiral and rotational domains. The intriguing net result, however, is a mesoscopic demixing of chiral species, i.e., the segregation of parallel twin chains in large enantiopure domains.

This explains in a natural way the experimentally unambiguous chiral segregation of twin chains in large domains. PVBA mass transport is most likely involved in this process. Another possibility would be chirality switch of the adsorbed molecules, i.e., conversion from chiral species α to β, but the corresponding energy barrier is presumably rather high.

Recently, macroscopic surface chirality from supramolecular assemblies has been reported [134]. In these experiments, however, one species of tartaric acid molecules, which are chiral in *three dimensions*, is employed and thus chiral species do not have to segregate in the self-assembly.

In the MD-simulations the atomic corrugation of the surface is neglected. The main part of the binding energy in the modeled chain structures is found to be due to head-to-tail coupling ($\sim$140 meV for a molecule involved in two head-to-tail bonds compared to an overall binding energy of $\sim$170 meV). The weak lateral interactions ($\sim$30 meV) are reflected in the small energy differences of the various simulated configurations. On Ag(111), the corrugation of the potential energy surface results in preferred adsorption sites of the molecular subunits and thus to a distinct orientation of the molecules, which leads to twin chains running along a $<11\bar{2}>$-direction. Whereas the parallel alignment of molecules in the favored twin chain feature (cf. Fig. 4.11(a)) allows for good coordination of all molecules to the Ag(111) substrate, the lattice match of the other configurations is rather poor increasing the energetic difference expected on the Ag(111) surface compared to the model. The corrugation of the Ag(111) surface also enhances the preference of twin chains. The bonding to the substrate of further attaching rows is less favorable due to a slight outward relaxation in twin chains away from ideal sites. In the monolayer structure the lattice mismatch between overlayer and substrate is apparent in the vertical displacement of some molecular rows in order to reduce strain.

Finally, we address the nature of the OH$\cdots$N hydrogen-bond. The carboxylic acid group might deprotonate and the proton be transferred to the N atom involved in the bonding. *Ab-initio* calculations of the *twin chain* depicted in Fig. 4.11(a) have been performed to gain insight into this issue. We used periodic boundary conditions in a cell of (15.0×15.0) Å^2, corresponding to the chain periodicity as determined by STM. Due to the complexity of the arrangement the inclusion of the metal surface is not feasible, calculations have thus been performed in vacuum. In Fig. 4.15 the resulting charge distribution in the molecular plane is mapped. The high electronic charge at the position of the O and N atoms within the molecule is clearly visible. No deprotonation

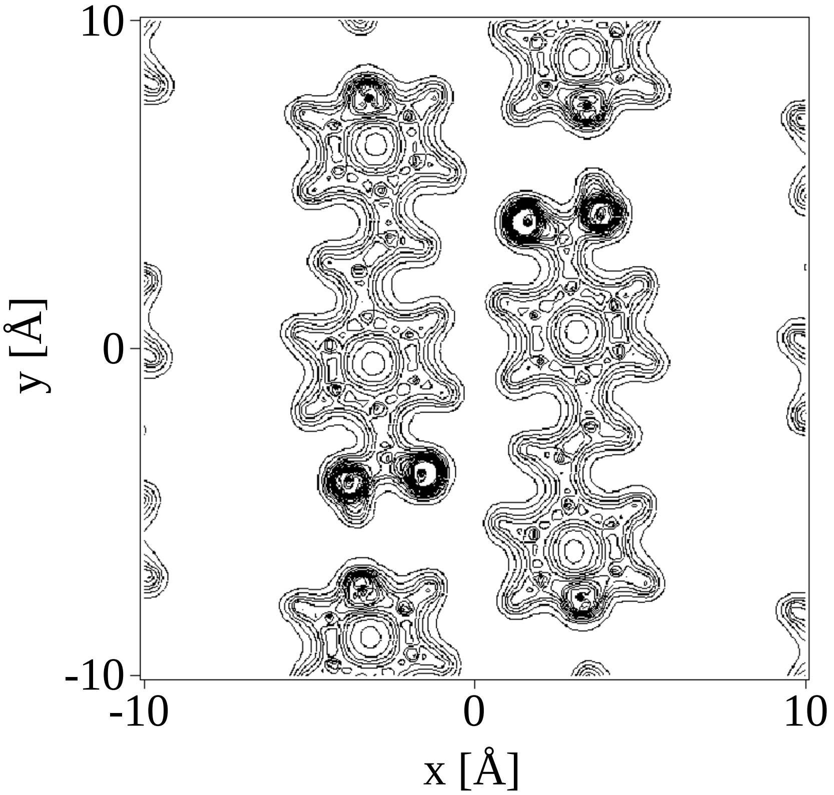

Figure 4.15: PVBA charge distribution in the molecular plane as determined by *ab initio* calculations (periodic boundary conditions, cell size (15.01×15.01) Å^2). Deprotonation of the carboxylic acid group does not occur, the net cost for proton displacement from the O to N atom amounts to ~ 0.6 eV.

of the carboxylic acid group occurs. The energy per chain unit of the relaxed geometry with the proton transferred to the N atom is ~1.15 eV higher, meaning ~0.6 eV of net cost for each proton displacement from the O to N atom. This is in agreement with ^{15}N NMR results of PVBA crystallites [38].

In conclusion, our STM measurements demonstrate that PVBA is mobile on the Ag(111) surface at low temperature (125 K). Molecular networks of flat lying molecules reflect directed π-bonding to the substrate and attractive intermolecular interactions. Molecules are linked via the *endgroups* which is in line with the expected hydrogen bond formation and MD-simulations elucidate the energetics of the bonding. The low temperature situation can be rationalized as diffusion limited aggregation of rod-like molecules subject to anisotropic interactions.

Equilibrium is reached upon annealing or adsorption at 300 K. One-dimensional PVBA twin chains running along a $<11\bar{2}>$-direction of the substrate are formed. High resolution STM images illustrate that molecules within a row are pointing in the same direction allowing for the formation of moderate OH$\cdots$N head-to-tail hydrogen bonds.

Neighboring rows are aligned antiparallel and linked by an intricate bonding mechanism including CH$\cdots$OC hydrogen bonds. Due to a distinct shift between adjacent rows the twin chains are enantiomorphic. The angled molecular geometry results in two chiral species for PVBA adsorbed on a surface. While twin chains with a combination of different enantiomers are feasible, they are energetically less favorable and the chirality of the supramolecular assembly is directly associated with the chirality of single molecules.

Repulsive interactions between neighboring twin chains result in the formation of a one-dimensional nanograting. The periodicity can be varied over a wide range by the coverage. At the completion of the monolayer a new structure evolves where the lateral order is lost and only the *direction* of chains is maintained.

In large domains all parallel twin chains are of the same chirality. Stimulated by STM results of metastable structures and MD-simulations, an intriguing scenario for the segregation of enantiomorphic twin chains in large domains is proposed, where chirality proliferates during the growth process.

Chapter 5

PVBA on Au(111) and Cu(111)

5.1 Au(111): Role of Surface Dislocations

Gold and silver should behave comparable from a chemical point of view, both being noble metals with deep lying *d* valence bands and a small density of states near the Fermi edge. Like on Ag(111) (cf. Chapter 4), the adsorbate-substrate interactions are expected to be weak for PVBA on Au(111) resulting in sufficient lateral mobility for the formation of long-range ordered structures. It is chosen to clarify whether the observed PVBA twin chains on Ag(111) are an intrinsic feature of PVBA on noble metal substrates. Furthermore the bare Au(111) surface is reconstructed and can be regarded as a model system to study the role of surface dislocations in the 2D self-assembly of supramolecular structures.

Fig. 5.1 shows an STM image of PVBA on Au(111) adsorbed at room-temperature and measured at 77 K. Twin chains are formed running along the $[11\bar{2}]$-direction as on the Ag(111) surface. Since the lattice constants of gold (4.08 Å) and silver (4.09 Å) are nearly identical, this surface direction guarantees again a good match of the molecular subunits and high symmetry lattice sites. The bare Au(111) surface is known to reconstruct into alternating regions of face centered cubic (fcc) and hexagonal close-packed (hcp) stacking of the surface atoms [113]. The domain walls form a chevron pattern with a periodicity of ~250 Å, which is clearly visible as bright stripes in the inset of Fig. 5.1 showing a large scale STM topograph of the bare Au(111) surface. The chevron pattern is as well visible for the PVBA covered surface and a closer inspection reveals that kinks are formed in the twin chains in order to run through the elbows of the reconstruction. In recent studies the elbows have been found to be favored adsorption sites for various metals as Fe [135], Co [136,137] and Ni [138,139]. Meyer *et al.* explained this phenomenon by a lower kinetic barrier to place exchange of adsorbate

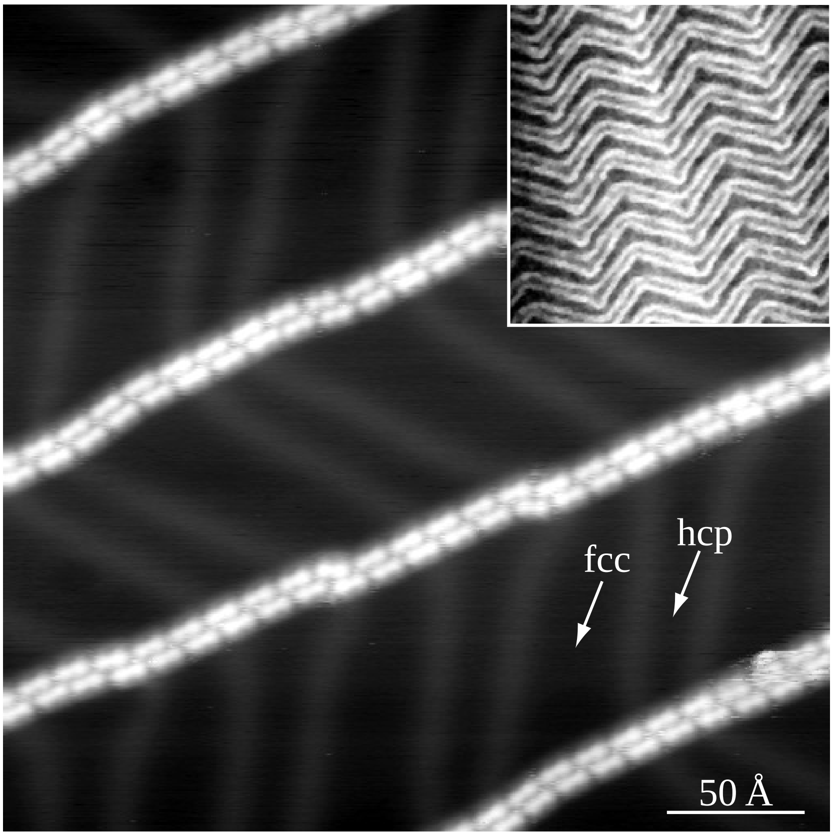

Figure 5.1: PVBA on Au(111) adsorbed at room-temperature and measured at 77 K. The same twin chain feature as on the Ag(111) surface is formed. The chains are aligned along $[11\bar{2}]$ giving optimal match of molecular subunits and substrate lattice. Kinks are created in the twin chains in order to run through the elbows of the reconstruction. In the inset a large scale image of the bare Au(111) surface is depicted illustrating the long-range periodicity of the chevron pattern.

atoms with Au at these specific sites and subsequent preferential nucleation on top of the substitutional metal atom [140]. Of course, this mechanism can be ruled out for large organic molecules such as PVBA, but Böhringer *et al.* report of 1-nitronaphtalene forming trimers pinned to the elbows at low coverage [141]. Apparently the Au surface atoms at the elbows show a locally increased reactivity. This is assigned to the disturbed local order leading to a lower coordination of these atoms. At equilibrium, molecules adsorb preferentially at elbows due to the increased bonding energy at these sites and a one-dimensional supramolecular nanograting evolves. The periodicity is dictated by the chevron pattern resulting in a highly regular arrangement with an interrow distance of about 100 Å. On Ag(111) a regular one-dimensional nanograting could be fabricated due to *repulsive interactions* between neighboring twin chains (cf. Chapter 4). The scattering of interrow distances narrows for smaller values but no regular spacing is achieved in the range of 100 Å due to decrease of repulsive interactions. On Au(111) the regular spacing of the natural surface defects extended over large domains is used as a *template*. This produces a nearly equidistant one-dimensional supramolecular nanograting with an interrow distance not accessible on Ag(111). We propose that this concept can be of general use for the positioning of molecules on substrates with dislocation patterns. Highly regular molecular nanostructures with given periodicity might be fabricated exploiting the multitude of surfaces with periodic lattice defects [142], e.g., the second Ag monolayer on Pt(111) showing a trigonal strain-relief pattern [143].

5.2 Cu(111): Interplay with Substrate Adatoms

The adsorption of PVBA on Cu(111) is a good example to illustrate the competition of different molecular subunits in the adsorbate-substrate interactions. Despite the different chemical nature of silver, gold and palladium PVBA adsorbs in a flat geometry on the investigated surfaces of these metals. This is rationalized by directed interactions of molecular π-electrons with metal states [92,93]. In contrast, on Cu(111) the carboxylic acid group of PVBA has the additional option of coupling to the metal via a copper-carboxylate bond.

In Fig. 5.2 an STM image of PVBA adsorbed on Cu(111) kept at 160 K is reproduced (measured at 5 K). Dendritic islands are formed on the surface, showing that PVBA on Cu(111) is mobile at 160 K and attractive interactions are operative. In contrast to the low temperature phase on Ag(111) the threefold substrate symmetry is clearly reflected in the island structure. Dendritic growth is frequently observed for low temperature metal aggregation on hexagonal close-packed surfaces [144], e.g., Ag on Ag(111) and Pt(111) [145] and Pt on Pt(111) [146]. The different island structures in low temperature aggregation of PVBA on Cu(111) and Ag(111) reflect the larger corrugation of the potential energy surface experienced on Cu(111). Besides dendritic islands single protrusions are present on the surface which are associated with isolated molecules oriented vertically. The height of these protrusions is about 1.4 Å, much smaller than the molecular length of 12.3 Å. This is assigned to poor electric conductance along the molecular axis or tilting of the isolated molecules interacting with the STM tip. Frederick *et al.* report the formation of a benzoate species for the related molecule benzoic acid on Cu(110) [147]. However, upright standing benzoate species are only found at high coverages. On Cu(111) benzoate is aligned normal to the surface at all coverages [148] (the mechanisms underlying the different orientations are addressed below.). The vertically oriented molecules are strongly bound to the surface, presumably

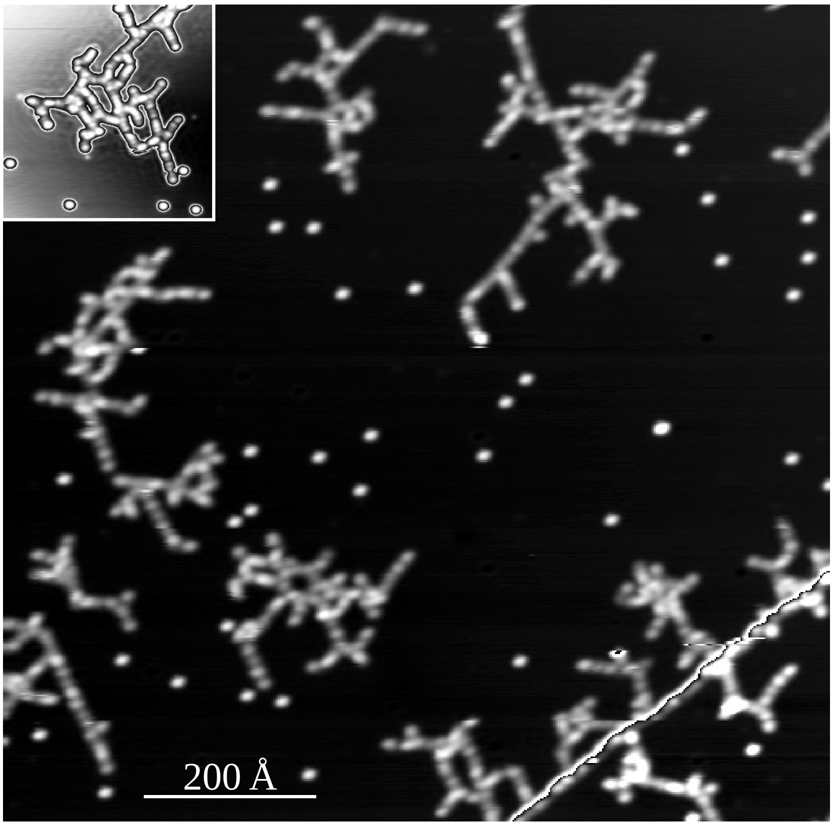

Figure 5.2: PVBA on Cu(111) adsorbed at 160 K (measured at 5 K). Molecules in dendritic islands coexist with isolated molecules in an upright bonding configuration (single protrusions). The bonding geometry of PVBA in the islands is not uniform as can be seen in the inset.

they are rather immobile at 160 K. The data suggest that the bonding geometry is determined already in the very first stage of the adsorption process due to, e.g., molecular orientation and kinetic energy of the arriving molecules whereupon different metastable states are populated. The coexistence of immobile monomers and islands is an exceptional phenomenon, unknown in metal epitaxy, and associated with different diffusion barriers due to different bonding configurations. In the islands the adsorption geometry is not uniform as can be seen in the inset. The competition between directed interactions of molecular π-electrons with metal states [92, 93], copper-carboxylate bonding and intermolecular interactions results in different adsorption geometries in the islands.

Deposition of PVBA on Cu(111) held at 425 K leads to the arrangement depicted in Fig. 5.3(a). Preferentially pairs of molecules in a linear complex with flat bonding geometry are formed. The adsorbed PVBA molecules are highly mobile at 425 K. Simultaneously Cu atoms evaporate from the step edges, a process which is inhibited at low temperature. This suggests that the interplay of PVBA with substrate *adatoms* plays a crucial role. On Cu(111) the rate for detachment of atoms from kinks onto the

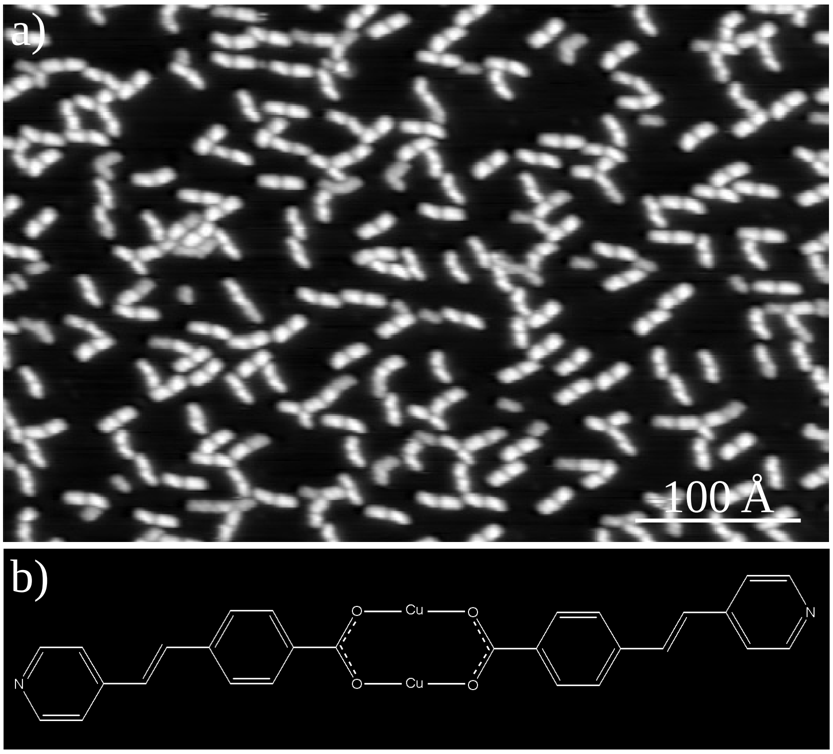

Figure 5.3: (a) PVBA on Cu(111) deposited at 425 K (measured at 77 K). Preferentially pairs of two molecules in a flat bonding geometry are formed. **(b)** Model of copper-carboxylate bonding, two copper atoms are bridging a pair of flat-lying molecules. The benzoic acid moiety is deprotonated to benzoate.

terrace is ∼15 s^{-1} at 425 K [149] and thus the surface is covered by mobile Cu atoms and interactions of the carboxylic acid group with these adatoms stabilize the flat PVBA geometry. The coupling of two PVBA molecules via Cu adatoms leads to the observed pairs of molecules in a linear complex with flat bonding geometry. The length of ∼ 28 Å as determined by STM is about twice the PVBA length (12.3 Å) and thus in accordance with a pair of flat lying molecules.

Similar findings have been reported by Perry *et al.* studying related systems, e.g., benzoic acid on Cu(111) [148]. They could prepare flat lying molecules under certain circumstances. In copper-coevaporation experiments they evidenced that the flat adsorption geometry is linked with the availability of metal adatoms. Deprotonation of the carboxylic acid group occurs and two copper atoms are bridging a pair of flat-lying molecules forming a copper-carboxylate bonding.

In Fig. 5.3(b) a model for PVBA in such a flat lying copper-benzoate complex is shown. It illustrates the *simultaneous* maximization of directed π-interactions to the metal surface and copper-carboxylate bonding.

In conclusion, on Au(111) the same twin chain feature as on Ag(111) is found demonstrating the intrinsic coupling of PVBA. Due to the locally increased reactivity of Au atoms at the elbows of the reconstruction a regular one-dimensional supramolecular nanograting with a periodicity dictated by the chevron pattern can be fabricated. Whereas on Ag(111) the regular spacing of twin chains is assigned to *repulsive interactions*, on Au(111) the periodicity of the surface reconstruction is used as a *template.* We propose that this concept can be of general use for the fabrication of highly regular molecular nanostructures.

On Cu(111), at low temperature dendritic islands coexist with single molecules oriented vertically at low temperature. The single molecules are associated with copper-carboxylate bonds. The contributions of directed π-interactions, copper-carboxylate bonding and intermolecular interactions lead to various metastable bonding configurations. At 425 K the surface is covered by mobile Cu adatoms evaporated from atomic steps and pairs of flat lying molecules bridged by two Cu atoms are formed upon cooling down. This allows the *simultaneous* maximization of directed π-interactions to the metal surface and copper-carboxylate bonding.

Chapter 6

PEBA on Ag(111): Chiral Packing of Achiral Molecules in Two Dimensions

In this Chapter we will present data of 4-[(pyrid-4-yl-ethynyl)]benzoic acid (PEBA) on Ag(111). From a chemical point of view the differences between PEBA and PVBA are marginal. In particular, the molecular endgroups designed to form head-to-tail hydrogen bonds are identical. The vinyl bridge of PVBA is substituted by an ethynyl bridge in PEBA (cf. Fig. 1.1). PEBA is thus slightly longer than PVBA (13.1 Å compared to 12.3 Å). The flat adsorption geometry in connection with the angled molecular structure of PVBA imposes a chirality in 2D which is not present in the gas phase. PEBA is linear and thus the adsorbed molecule is achiral (disregarding the asymmetry of the carboxylic acid group which freely rotates in the gas phase and is expected to flip on the surface). The comparison of these two molecules allows to gain insight into the principles in hydrogen-bond formation and supramolecular self-assembly at metal surfaces, especially to elucidate the role of shape and symmetry in the aggregation.

In the first part of this Chapter the ordering at low temperatures is reported. Similar networks as for PVBA are found demonstrating that the molecular *endgroups* are the active bonding sites. In the second part the equilibrium structure is discussed. PEBA grows in two-dimensional islands, in striking contrast to PVBA. At room-temperature migration even over step edges is possible leading to preferred covering of large terraces. Small terraces are nearly empty; only the upper and lower step edges are decorated. The 2D islands consist of linked molecular chains having a distinct shift and the supramolecular structure is thus enantiomorphic. Due to the threefold substrate symmetry three rotational domains exist on the Ag(111) surface. In addition, the mirror symmetry of

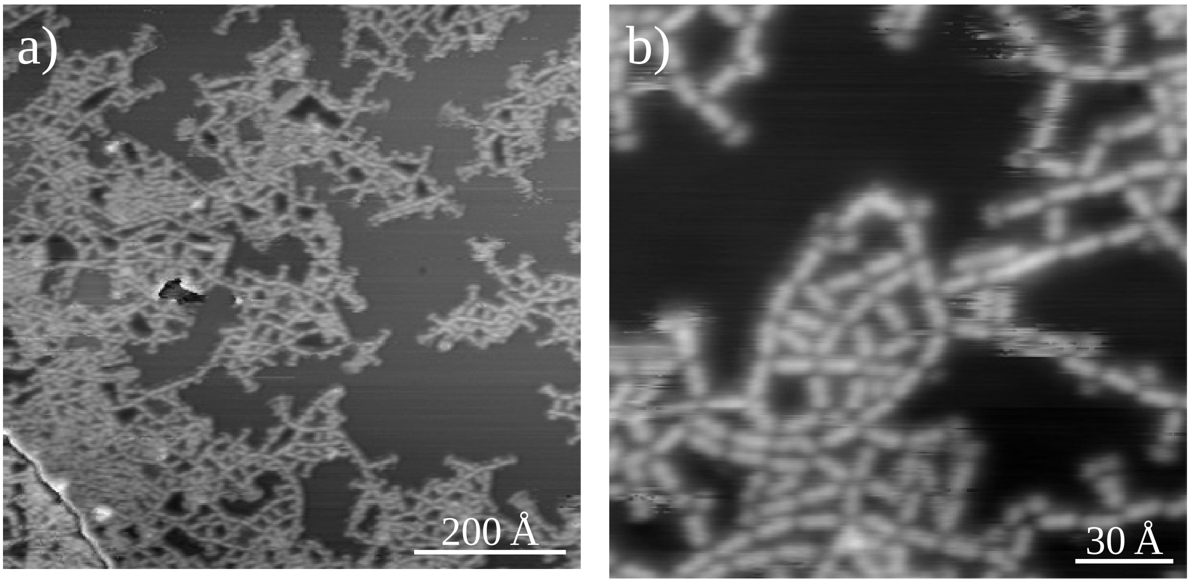

Figure 6.1: PEBA on Ag(111) evaporated at $T_{\mathrm{Ag}} = 150$ K and measured at 77 K. **(a)** On a large scale networks are formed, either growing from step edges or as islands in flat terraces. **(b)** A close up shows that the molecules adsorb in a flat geometry and interact via the *endgroups*.

the substrate accounts for a mirror domain to every rotational domain having opposite chirality. In contrast to the PVBA/Ag(111) system (cf. Chapter 4) where *chiral* molecules built enantiomorphic supramolecular structures due to *separation* of chiral species, the *packing* of *achiral* PEBA molecules causes enantiomorphic structures on the Ag(111) surface. A model for the PEBA supramolecular structure is proposed. The findings are discussed with regard to the related system PVBA/Ag(111).

In Fig. 6.1 an STM image of PEBA evaporated on a Ag(111) surface held at 150 K is depicted. After deposition the sample was transferred into the liquid nitrogen cooled STM freezing the prepared situation (all STM measurements shown in this Chapter have been performed at 77 K). On a large scale molecular networks are formed (cf. Fig. 6.1(a)), either growing from step edges or as individual islands in flat terraces. PEBA is mobile on the Ag(111) surface at 150 K and attractive interactions are operative between the molecules. The detail image in Fig. 6.1(b) shows that the molecules adsorb in a flat geometry and couple via the endgroups. The flat adsorption geometry reflects the directed π-bonding of PEBA to the metal surface which has been similarly found for PVBA (cf. Chapter 3 and 4). The interaction of molecular endgroups is attributed to head-to-head and head-to-tail hydrogen bond formation, in accordance with the scenario of low temperature deposited PVBA on Ag(111) (cf. Chapter 4). As for PVBA the crystal structure of PEBA is stabilized by head-to-tail hydrogen bonds [81]. The head-to-tail hydrogen bonding in the meandering chains and the bonding at the intersections of several molecular endgroups is discussed in more detail in Chapter 4 for PVBA. Compared with PVBA, the PEBA network is more compact. This is attributed to the different molecular shape and thus a steric effect. The low temperature island growth can again be rationalized as diffusion limited aggregation of rodlike species subject to anisotropic interactions.

In the following the equilibrium situation reached upon annealing such a film or direct adsorption with the Ag(111) surface held at room-temperature is discussed. In Fig. 6.2(a) a large surface area with some monatomic steps is depicted. Whereas the large terraces are nearly completely filled, on smaller terraces the coverage is low and basically only the step edges are decorated. This demonstrates that the molecules are able to migrate over step edges and large islands form, resulting in fewer energetically unfavorable island boundary sites. This so called Ostwald ripening is caused by a more rapid dissociation of smaller islands in favor of the growth of larger ones (in metal epitaxy this phenomenon is extensively studied [150–152].).

Fig. 6.2(b) demonstrates the formation of two-dimensional islands on large terraces, two domains rotated by an angle of 60° are discernible. The smaller scale in Fig. 6.2(c) illustrates that both the upper and the lower step edges are decorated with molecules. A close inspection reveals that the two different islands present in this image are not rotated by a multiple of 60° as expected from the substrate symmetry but represent a pair of enantiomorphic supramolecular structures. In Fig. 6.2(d) the distinct shift of the molecular chains in the supramolecular structure is easily discernible. This will be discussed in full detail below.

At the upper step edge double rows are aligned parallel to the monatomic step. At the lower step edge the molecules preferentially adsorb perpendicular and some double rows attach to these molecules. On Pd(110) no preferential adsorption of PVBA at the atomic step edges is found showing that the lateral interactions of adsorbed PVBA and palladium are weak (cf. Chapter 3). The strong direction-dependence is assigned to binding mainly via π-electrons [92, 93]. Whereas preferential adsorption at the lower step edge is a common phenomena and is attributed to higher coordination with substrate atoms, the preferential adsorption at the lower *and* upper step edge is only rarely reported in literature. The discontinuity in the surface potential at a step results in redistribution of charge from the top to the bottom of the step [153, 154]. This is believed to be the reason for the exceptionally strong affinity of 7,7',8,8'-tetracyanoquinonedimethane (TCNQ) for adsorption at the lower Cu(111) step edges. Kamna *et al.* report that after the lower step edge is completely decorated, TCNQ binds to the upper step edges [155].

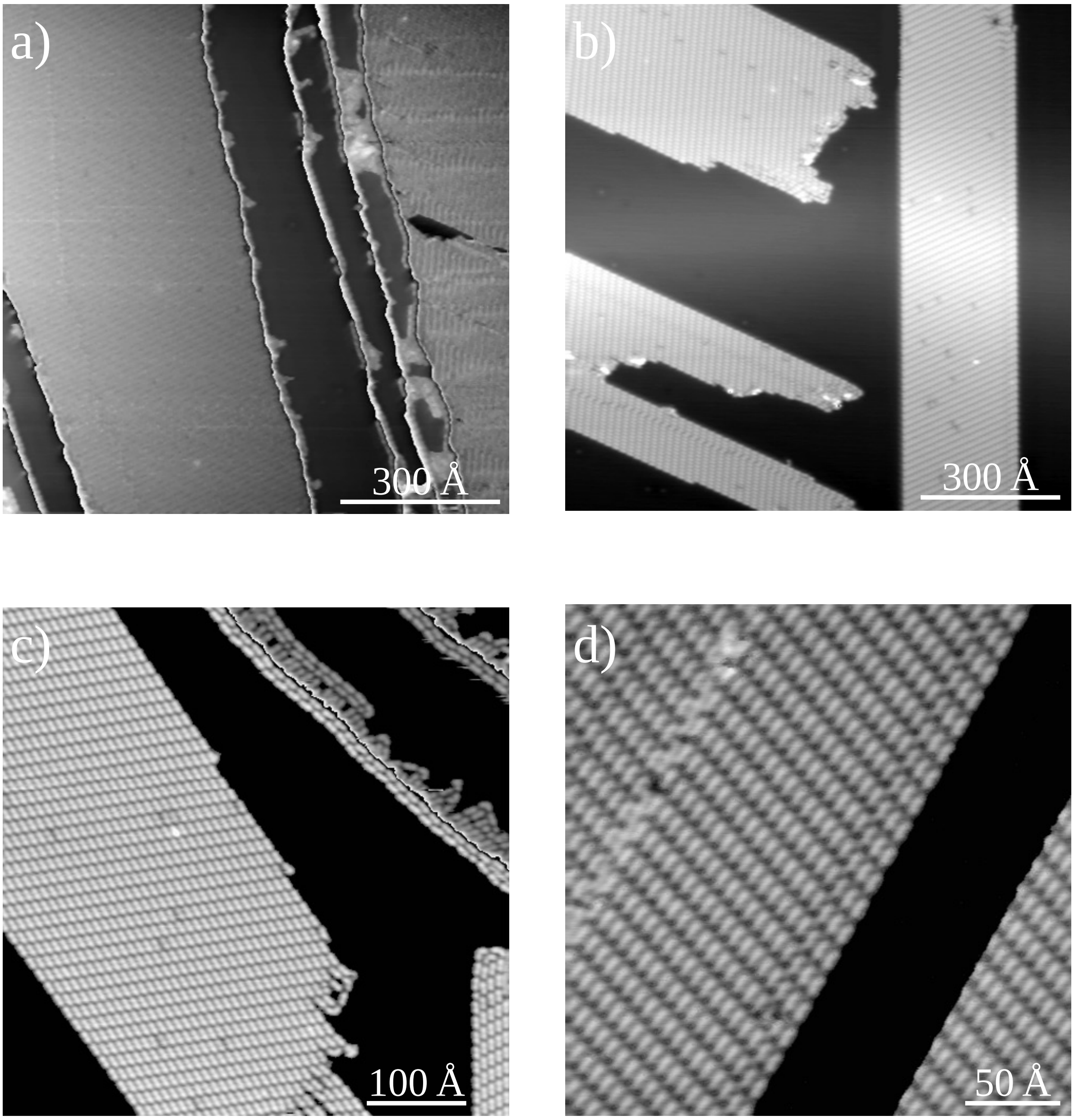

Figure 6.2: Equilibrium structure of PEBA on Ag(111). The structures in (a, d) have been prepared by 5 minutes deposition with the surface kept at *room-temperature*, in (b, c) PEBA has been evaporated during 1 minute at $T_{\mathrm{Ag}} = 150$ K and *subsequently* annealed to 300 K for 2 minutes. **(a)** Large scale image with some monatomic steps. Whereas the large terraces are nearly completely filled, on smaller terraces the coverage is low and basically only the step edges are decorated. **(b)** Large scale image demonstrating the formation of two-dimensional islands on large terraces. Two domains rotated by an angle of 60° are discernible. **(c)** Smaller scale showing that both, the upper and the lower step edges are decorated with molecules. **(d)** The packing of achiral PEBA molecules causes an enantiomorphic supramolecular structure.

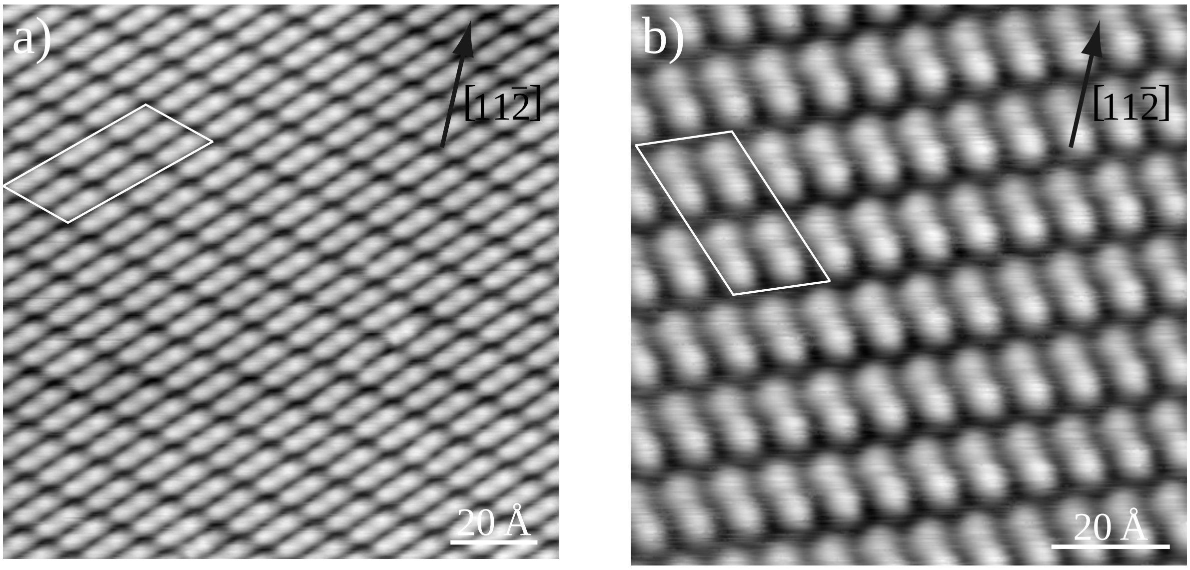

Figure 6.3: Equilibrium structure of PEBA on Ag(111). The substrate mirror symmetry results in a mirror domain to every rotational domain having opposite chirality, thus a total of six different domains are present on the Ag(111) surface. In **(a)** a mirror domain of **(b)** is represented.

In contrast, 1-nitronaphtalene on Au(111) was found to preferentially adsorb at the *upper* step edge and upon completion a second row forms along the step edge on the *lower* terrace [141]. The second row molecules are oriented perpendicular to the step edge which is interpreted in terms of directional attractive molecular interactions.

Unlike to low temperature adsorption the molecules at the step edge do not act as nucleation center but isolated islands consisting of linked chains are forming on flat terraces. High resolution STM images demonstrate that all molecules within the two-dimensional islands point in the same direction. The borders of the islands are nearly perfectly straight (cf. Fig. 6.2(d)), kinks are energetically unfavorable because no head-to-tail bonds can be formed. The tendency to head-to-tail hydrogen bonding is also apparent in Fig. 6.2(c) where molecules at the chain end rearrange to saturate the endgroups.

Our results show that the PEBA molecules do not follow a high-symmetry direction of the substrate. The threefold substrate symmetry is reflected in three rotational domains on the Ag(111) surface. The substrate *mirror* symmetry results in a mirror domain to every rotational domain having opposite chirality, thus a total of six different domains are present on the Ag(111) surface.

Two mirror symmetric domains are represented in Fig. 6.3. The domains form an angle of $(94 \pm 4)^\circ$ and thus are rotated by $\pm(47 \pm 2)^\circ$ with respect to the $[11\bar{2}]$-direction.

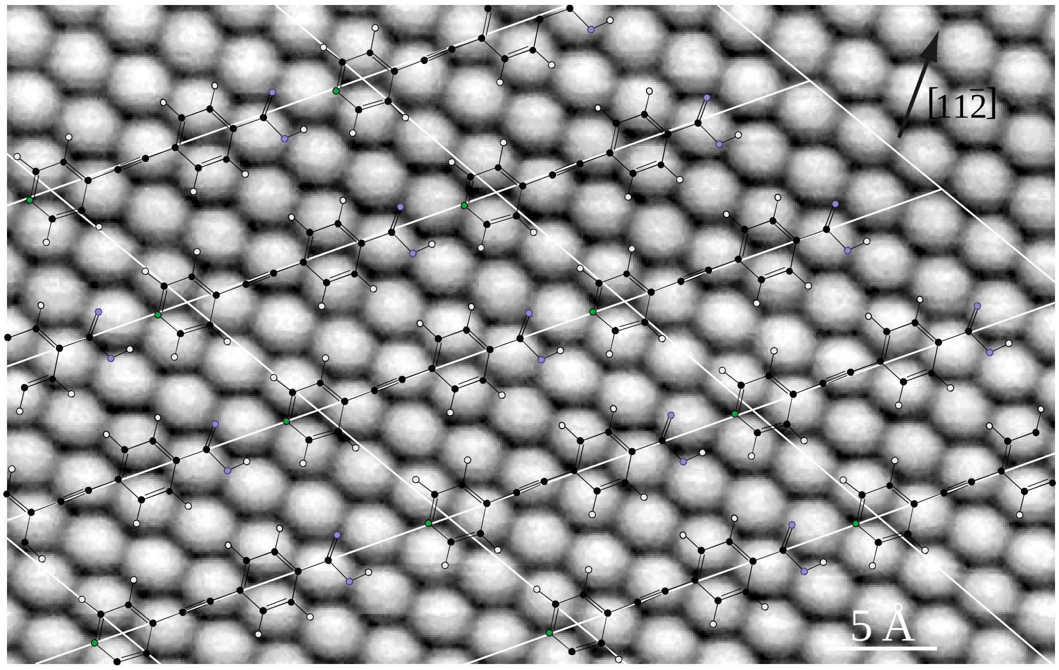

Figure 6.4: Montage of an Ag(111) atomic resolution image with a proposed model of PEBA structure to scale illustrating the match of molecular geometry and substrate lattice.

In the case of PVBA the reflection would change chirality of each molecule. PEBA is not chiral and the same bonding geometry is retained in related mirror domains. In contrast to the PVBA/Ag(111) system (cf. Chapter 4) where *chiral* molecules built enantiomorphic supramolecular structures due to *separation* of chiral species, the *packing* of *achiral* PEBA molecules causes enantiomorphic structures on the Ag(111) surface. Chiral symmetry breaking in the self-assembly of monolayers from achiral molecules has been reported in a recent STM study by Sowerby *et al.* for adenine on molybdenite [156]. Other examples include Langmuir-Blodgett films [157] and liquid crystals [158].

From STM images the substrate direction of the molecular chains in the different domains and the intermolecular distances can be determined. In Fig. 6.4 a montage of an Ag(111) atomic resolution image with the proposed model of the PEBA structure drawn to scale is represented. The molecular chains are running along [3$\bar{1}\bar{2}$] (in the mirror domains along [21$\bar{3}$]) with a chain periodicity of 15.3 Å and an interrow distance d of about 6.6 Å. The distance between the head O and the tail N atoms amounts to 2.3 Å.

For the PEBA/Ag(111) system as well as for PVBA on Ag(111) the intermolecular interactions and the molecule-substrate interactions are well balanced and long-range ordered structures evolve. The intricate difference in the self-assembly is the *two-dimensional* supramolecular islanding in contrast to the formation of *one-dimensional* twin chains (cf. Chapter 4). In the case of PVBA repulsive interactions operate between twin chains and two-dimensional islanding is only observed at the completion of the monolayer when space limitations become appreciable.

The strikingly different behavior of the two molecules can be rationalized as follows: While both molecules adsorb in a flat geometry, the slightly different length of PEBA and PVBA (13.1 Å compared to 12.3 Å) results in a different orientation of the molecular axis with respect to the Ag substrate lattice. Whereas for PVBA the orientation along a <11$\bar{2}$> direction allows for optimal coordination of the molecular subunits with high symmetry lattice sites, the linear structure of PEBA and the difference in length of 0.8 Å leads to an orientation of the molecular axis along [3$\bar{1}\bar{2}$] direction, rotated by 13° with respect to [11$\bar{2}$].

In both cases molecules interact via head-to-tail hydrogen bonding and thus form chains. The periodicity of PVBA chains amounts to 15.0 Å, only slightly shorter than in the case of PEBA (15.3 Å). This results in stronger OH$\cdots$N hydrogen bonding between PEBA molecules (bond distance $\sim$ 2.3 Å) than in the case of PVBA (bond distance $\sim$ 2.5 Å). For comparison, in crystals of nucleic acid components and isonicotinic acid (a lower analogue of PEBA) values in the range of (1.5-2.1) Å are reported [109, 110].

Adjacent rows in twin chains are aligned antiparallel and shifted. In contrast, all PEBA molecules within an island point in the same direction. In a classical dipole model the molecules should align antiparallel to minimize the electrostatic potential energy. Apparently the dipole approximation is not applicable for the short distances involved in supramolecular assembly. Rather the complete charge distribution has to be regarded to explain for the intricate coupling mechanism, MD-simulations have been successfully performed for PVBA on Ag(111) (cf. Chapter 4). In twin chains adjacent rows are linked by *two* CH$\cdots$OC hydrogen bonds per chain segment (bond distance $\sim$ 2.9 Å) saturating all atoms potential hydrogen bonds. In the case of PEBA the chains are repeatedly linked and two dimensional islands evolve. Despite the smaller interrow distance in the PEBA structure (6.6 Å compared to 6.9 Å in the PVBA twin chains) the linear molecular structure results in a CH$\cdots$OC distance of $\sim$ 4.0 Å, too large for efficient hydrogen bonding [111]. The coupling of adjacent rows is thus believed to be rather weak.

In conclusion, at low temperatures for both molecules similar networks are formed demonstrating that the molecular *endgroups* are the active bonding sites. This scenario can be rationalized as diffusion limited aggregation of rodlike species subject to anisotropic interactions. At room-temperature PEBA molecules migrate even over step edges leading to preferred covering of large terraces. Smaller terraces are nearly empty and only the upper and lower step edges are decorated. In equilibrium, PEBA is forming two-dimensional islands, in striking contrast to PVBA. In the islands adjacent chains show a distinct shift and the supramolecular structure is thus enantiomorphic. The threefold substrate symmetry leads to three rotational domains on the Ag(111) surface. The mirror symmetry of the substrate creates a mirror domain with different chirality to every rotational domain. In contrast to PVBA, PEBA is not chiral and the same bonding geometry is maintained in related mirror domains. A molecular model for the PEBA structure is proposed. The molecular chains are running along $<3\bar{1}\bar{2}>$ (along $<21\bar{3}>$ in the mirror domains) with a chain periodicity of 15.3 Å and an interrow distance d of about 6.6 Å. This gives a OH$\cdots$N distance of 2.3 Å, slightly shorter than in the case of PVBA (2.5 Å) allowing for stronger hydrogen bonding. Due to the linear geometry of PVBA no efficient hydrogen bonds between adjacent rows can be formed. In contrast to the PVBA/Ag(111) system where *chiral* molecules built enantiomorphic supramolecular structures due to *separation* of chiral species, the *packing* of *achiral* molecules causes enantiomorphic structures for PEBA on Ag(111). The comparison with PVBA demonstrates how subtle differences in the molecular geometry result in drastic changes in the self-assembly.

Chapter 7

C_{60} on Pd(110)

The shape of the best known fullerene C_{60}, a truncated icosahedron, has fascinated mankind long before the discovery of the carbon fullerenes. Drawings of this object attributed to Leonardo da Vinci date from the early sixteenth century (cf. Fig. 7.1). On a large scale, curved geodesic structures derived from pentagons and hexagons have been constructed by the architect and inventor R. Buckminster Fuller. It was in his honor that the new family of carbon molecules was named Fullerenes.

In diamond the carbon atoms are sp^3-hybridized giving an ideal bond angle of 109.5°. In graphite the carbon atoms are sp^2-hybridized with an ideal bond angle of 120° and hexagons are formed. In C_{60} the 60 carbon atoms have an intermediate hybridization [159] leading to a polyhedral surface consisting of 12 pentagons and 20 hexagons. Since the shape of C_{60} resembles exactly a soccer ball it has been nicknamed “buckyball”.

The existence of a closed-cage molecule consisting of 60 carbon atoms was first proposed by Kroto *et al.* [160] in 1985. But only since the discovery of a technique for producing and purifying C_{60} in macroscopic quantities by Krätschmer *et al.* [161] in 1990, pure C_{60} became available to a large scientific community. Promising and appealing technological applications [40] stimulated the investigation of the properties of this fascinating new carbon-based material. In the beginning the main focus was on the geometric and electronic structure of pure and alkali metal doped C_{60} bulk samples [41]. Today, the study of interactions between fullerenes and surfaces has developed into a major area of research on this third allotropic form of carbon. Two aspects motivate this interest. Firstly, from a technological point of view, the substrate-induced modification of the electronic and structural properties of C_{60} layers is an important question to be addressed if this new material should find an application in the electronics industry. Secondly, the variety of both bond strength and bond character observed in

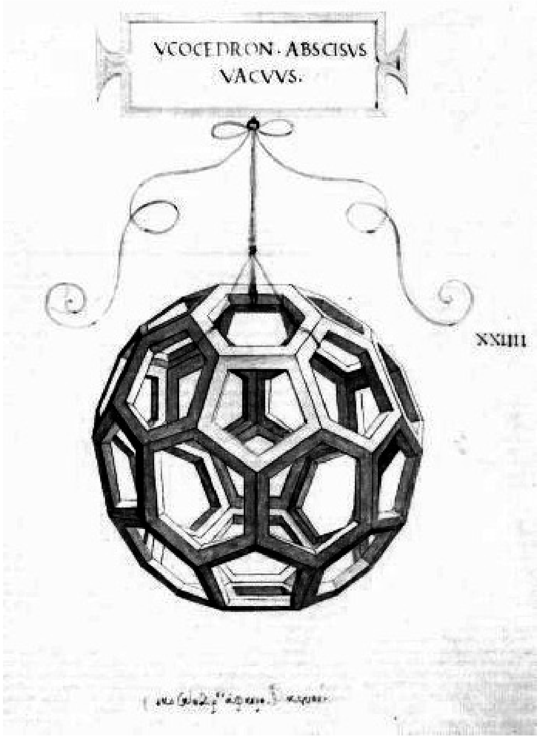

Figure 7.1: Design of a truncated icosahedron, first published in the book "De Divina Proportine" of Luca Pacioli (Venice, Pagani 1509). It is generally believed that Leonardo da Vinci made the illustrations for this book.

the interaction between C_{60} and a substrate is really exceptional. The nucleation and growth of C_{60} on a variety of different substrates, ranging from GeS [162], SiO_2 [163] or graphite [164], where the formed bonding is a very weak van der Waals type, to C_{60} adsorbed on potassium multilayers, where a negative charge state of the fullerene of the order of 11^- is found [165], has been studied. The adsorption of C_{60} has been investigated on a multitude of different metal surfaces, as for example Cu(110) [166–169], Cu(111) [166,170], Ni(110) [168,171–173], Pt(111) [172,173], Ag(111) [173,174], Ag(110) [175], Au(110) [171,176], Au(111) [174,177] and Al(111) [165,166,178]. A recent review is given in [179]. On all metallic surfaces investigated so far, fullerenes are chemisorbed, but the degree of hybridization of the C_{60} molecular orbitals with the substrate electronic states and the amount of charge transfer differ significantly from substrate to substrate. On most surfaces C_{60} tends to form well-ordered quasihexagonal close-packed overlayers with a nearest neighbor separation close to that of the van der Waals bonded solid C_{60} close-packed plane. In general C_{60} is regarded as ball shaped neglecting the real molecular geometry consisting of 5- and 6-membered rings. Recently it has been shown that the *orientation* of the C_{60} cage can be determined by full-hemispherical angle-scanned x-ray photoelectron diffraction (XPD) [166, 169]. C_{60} is found to bind in different high symmetric configurations ranging from a 6-membered ring, a 5-6 bond to a C edge atom facing to the surface, depending on nature and symmetry of the substrate.

In this Chapter a combined STM, LEED and XPD study of the mobility and growth of C_{60} on a Pd(110) surface is presented. The energy barrier for single molecule diffusion of C_{60} on a flat terrace of Pd(110) is determined to ∼1.5 eV by means of variable-temperature STM. Two differently bound C_{60} species are distinguished; one is metastable and is irreversibly converted into the other upon thermal activation. The mobility of Pd substrate atoms turns out to play a crucial role in the growth process. In STM images three highly ordered structures consisting of alternating dark and bright molecular rows are found, in combination with LEED their real space structures are determined. XPD results complete the understanding of the film structure and reveal the molecular orientation of the C_{60} molecules. Furthermore they unambiguously rule out that different molecular orientations might be responsible for the appearance of dark and bright rows in STM.

7.1 Mobility, Bonding Transition and Superstructures

Although there is a multitude of studies on the adsorption and growth of C_{60} on different substrates (see above), to our knowledge there is no detailed investigation of C_{60} surface diffusion. The thermal motion plays a crucial role in the film growth and an accurate knowledge is indispensable to fully understand the ordering and interactions at surfaces. Variable temperature STM has proven to be a powerful tool for the direct investigation of surface diffusion of large organic molecules at metal surfaces (cf. Section 3.2), but finds some limitations with the present system.

In Fig. 7.2 the thermal motion of C_{60} molecules and Pd substrate atoms is visualized. The two consecutive STM images are taken at the same surface area with a time lapse of approximately 1600 s at a substrate temperature of 437 K. The arrows marked with (m) show isolated C_{60} molecules on a flat terrace whose positions have changed. The temperature dependence of the site changes of these molecules has been used to determine the energy barrier for diffusion of C_{60} on a flat Pd(110) terrace (for a detailed description of the data evaluation cf. Section 3.2). A close inspection of the STM data shows that the C_{60} surface diffusion is not strictly one-dimensional as in the case of PVBA on Pd(110), nevertheless motions along $[1\bar{1}0]$ prevail. The arrows marked with (c) and (d) show C_{60} cluster formation and dissociation, respectively. Attractive intermolecular interactions lead to an increased number of C_{60} clusters compared to expectations from statistical distribution. The fact that the dissociation of C_{60} clusters

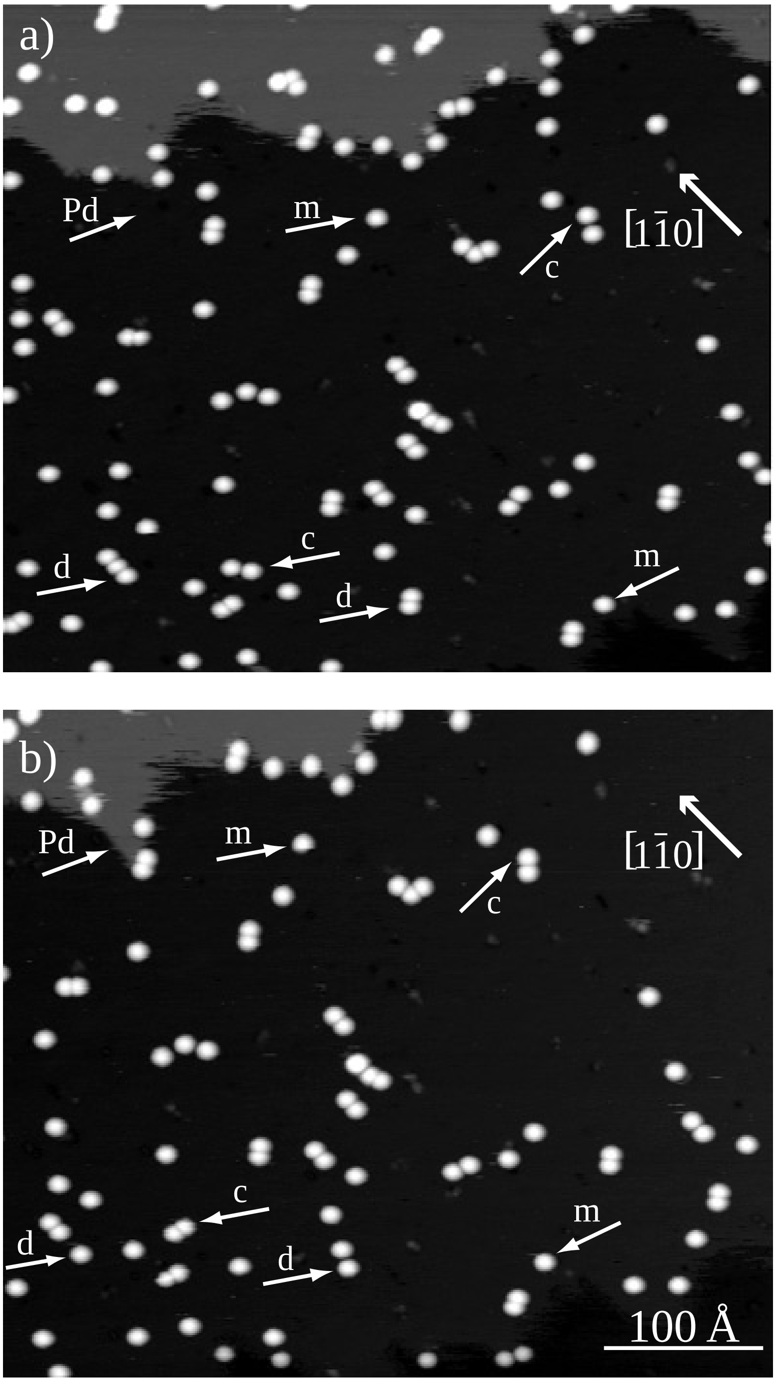

Figure 7.2: Series of STM images monitoring thermal motions of metastable C_{60} molecules and Pd substrate atoms on Pd(110) at $T = 437$ K. The time lapse between the two consecutive images is 1600 s. Arrows indicate: (m) single C_{60} monomers whose positions changed, (c) C_{60} cluster formation and (d) C_{60} cluster dissociation due to moving C_{60} molecules. The arrow in the top left corner of the STM image marked with (Pd) indicates the thermal motion of a monatomic substrate step. Note that two C_{60} molecules adsorbed on the lower step edge in (a) are embedded by the moving Pd terrace in (b) but are still bound to the lower terrace.

takes place at 437 K is attributed to relatively weak lateral C_{60}-C_{60} interactions, which are presumably of van-der-Waals type, as in the C_{60} bulk. This is in accordance with the desorption of the multilayer C_{60} at 455 K [180]. In contrast to integral methods, as for example helium atom scattering (HAS), the local information of STM offers the advantage to distinguish between these different processes and allows to gain insight into diffusion of an isolated molecule on a flat terrace. Another notable process taking place in the two STM images of Fig. 7.2 is the moving Pd substrate step in the upper left corner (marked with (Pd)). Two C_{60} molecules adsorbed on the lower step edge in (a) are embedded by moving Pd atoms in (b). From the height of the C_{60} molecules it is concluded that they are still bound to the lower Pd terrace surface layer. This is a hint for strong *lateral* attractive interactions between Pd atoms and C_{60} molecules. Due to the increased molecular coordination to Pd, C_{60} is expected to be more strongly bound in this configuration. Cuberes *et al.* [170] reported of C_{60} molecules on Cu(111) which have been trapped in nanometer-sized Cu vacancies after manipulating C_{60} over a step edge with an STM tip. They have still been bound to the second Cu layer below the surface. In contrast to the present system the lateral interactions between PVBA and Pd have been found to be negligible (cf. Section 3.1). The strong direction-dependence of the PVBA-Pd interactions has been assigned to binding via π-electrons. In the case of C_{60} the ball shape of the molecular geometry provides the additional possibility of lateral π-bonding to Pd.

The temperature range accessible with the present system and instrumentation for the determination of the diffusion rates is the interval 435–485 K. The statistical frequency analysis is plotted in an Arrhenius representation in Fig. 7.3. For each value between 250 and 800 events have been counted. The linear fit of the entire data set yields an energy barrier of (1.0 ± 0.5) eV. The larger uncertainty compared to PVBA-diffusion (Fig. 3.7) may be attributed to effects of lateral adsorbate-tip interactions. The STM measurements have been performed in the constant current mode with typical tunneling voltages of 1.2 V and currents below 0.5 nA, i.e., in the high tunneling resistance regime ($> 2\text{G}\Omega$). Variation of this tunneling parameters did not result in a systematic change in rates, i.e., going to lower tunneling resistances where adsorbate-tip interactions should become larger did not increase the mobility. Nevertheless the diffusion measurements for C_{60} on Pd(110) turned out to be more delicate than for the system PVBA/Pd(110) which may be at least partially due to the height of the C_{60} molecules. Sørensen *et al.* have calculated that the energy barriers for adatom diffusion are lowered by the influence of the tip [181]. Disregarding the grey plotted, probably tip influenced values the linear fit (dashed line) yields an energy barrier of $\sim$1.5 eV. Due to the large uncertain-

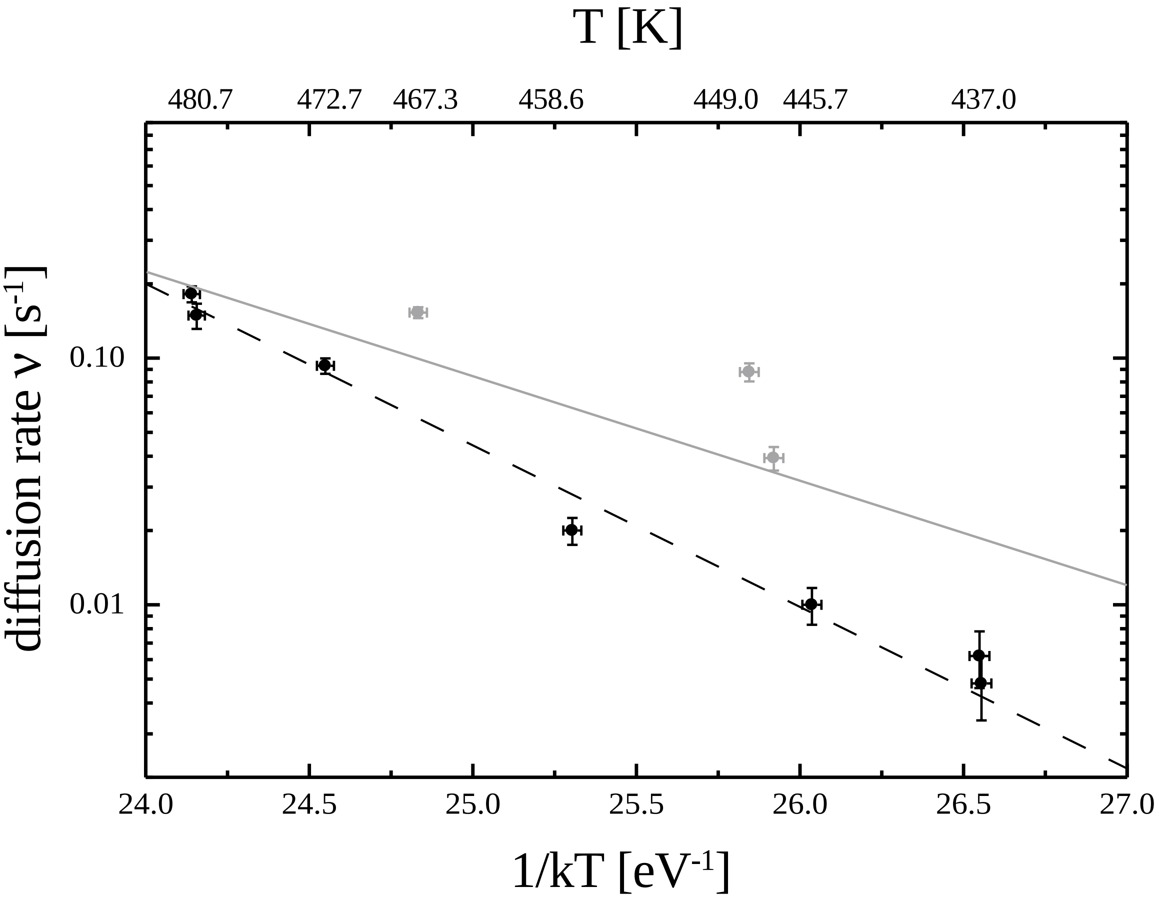

Figure 7.3: Arrhenius plot of single molecule diffusion rates in the temperature interval between 435 and 485 K. From the linear fit (straight line) the energy barrier can be determined to (1.0 ± 0.5) eV. The scattering of the data is attributed to effects of lateral adsorbate-tip interactions due to the height of the C_{60} molecules. Disregarding the grey plotted, probably tip influenced values the linear fit (dashed line) yields an energy barrier of ~1.5 eV.

ties we refrain from an estimate of the attempt frequency. The mechanisms involved in the thermal motion of C_{60} might differ from that of atoms or simple molecules, which can be rationalized as a hopping between adjacent bonding sites. Due to the shape and size C_{60} can be a rolling "buckyball", where high coordination of C_{60} to Pd substrate atoms is locally retained. The persistent lateral π-bonding should energetically favor this process.

At higher temperatures the mobility of C_{60} molecules does not increase continuously, rather their bonding characteristics change entirely. Upon annealing C_{60} molecules deposited at room-temperature to about 720 K, the apparent height in the STM images decreases substantially. To exclude imaging-effects the following experiment has been performed: A small amount of C_{60} is evaporated on a Pd(110) surface kept at room-temperature. All C_{60} molecules are identically imaged and the height is determined

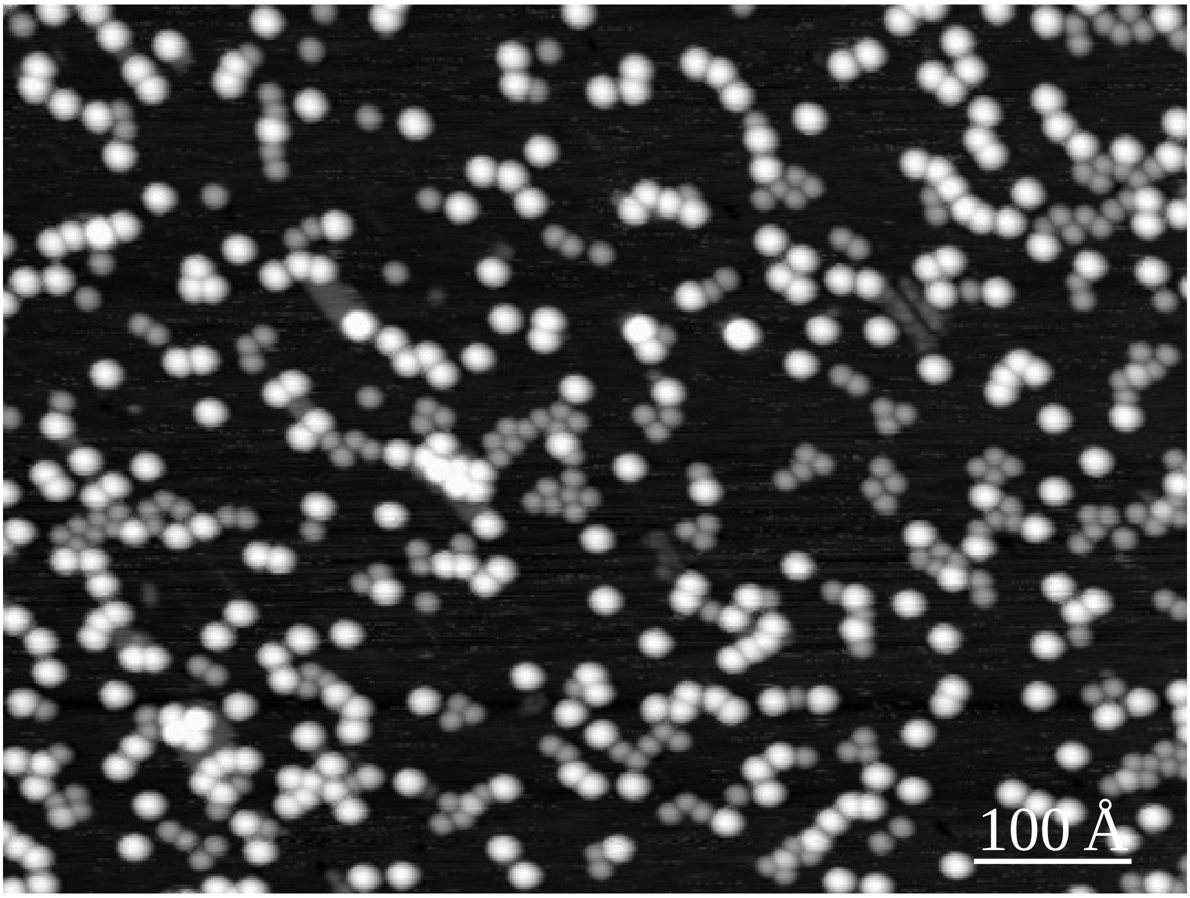

Figure 7.4: Pd (110) surface after evaporation of C_{60} at room-temperature for 2 minutes followed by annealing to 720 K and subsequent C_{60} evaporation at room-temperature during 1 min. Two different molecular species are clearly discernible; the bright molecules ((5.5 ± 0.2) Å high) are metastable and convert into the dark species ((3.1 ± 0.2) Å high) upon annealing.

to (5.5 ± 0.2) Å. Upon annealing to 720 K, STM images taken at room-temperature show again identical C_{60} molecules which are now more often found in clusters and the height has decreased to (3.1 ± 0.2) Å. In the STM image shown in Fig. 7.4 an additional small amount of C_{60} has been evaporated with the sample held at room-temperature. Two different molecular species are clearly discernible. The bright molecules are mostly isolated at the surface whereas the majority of the dark species is found in clusters. It can be concluded that the bright molecules are metastable and convert into the dark species upon annealing. The single molecules within a C_{60} cluster can be easily distinguished. The apparent molecular shape in the STM images is deformed and clusters are imaged like “soap bubbles”. This is not associated with a deformation of the C_{60} cage but rather an electronic effect. The intermolecular distance within a C_{60} cluster is with about 12 Å quite large and the strong perturbation of electron density is astonishing for the expected

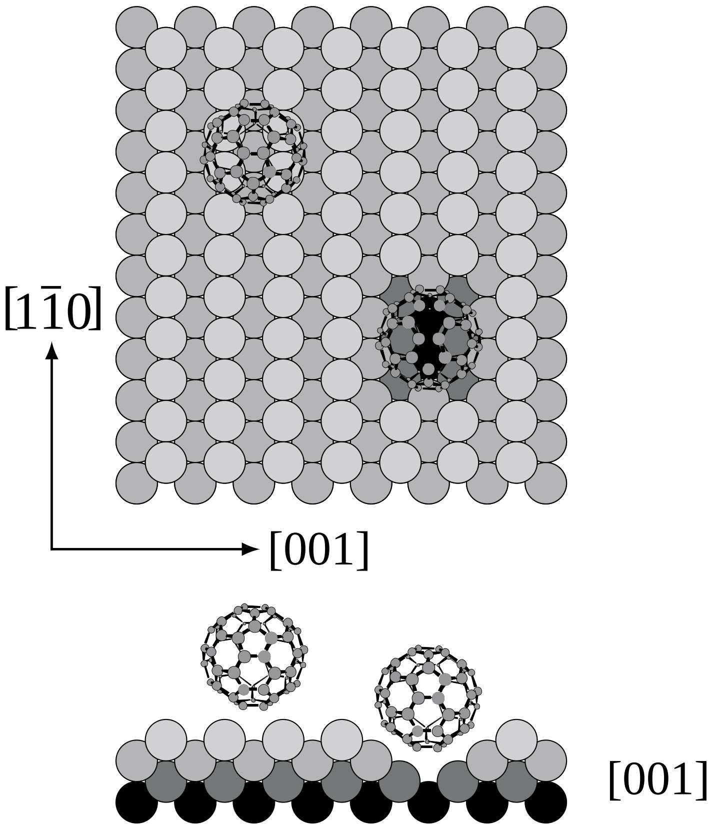

Figure 7.5: Model for the bonding configurations of metastable and stable bound C_{60}. Whereas metastable C_{60} binds to the first Pd layer, the release of 8 Pd substrate atoms allows for binding to the third Pd layer. The side view demonstrates the increased C_{60}–Pd coordination in the stable bonding configuration.

pure van der Waals interactions. The mobility of the dark species is much lower which reflects a stronger adsorbate-substrate interaction. Determination of the energy barrier for diffusion of the dark species is impossible in view of the above mentioned clustering and instrumental limitations. These results already demonstrate that the transition is thermally activated, but the nature of the bonding change is still unclear. To distinguish between height differences due to geometrical and electronic effects, the bias voltage is varied between −5 V and +5 V. No dependency of the apparent C_{60} molecular height and the bias voltage is found. The height difference between metastable and stable C_{60} of 2.4 Å is close to twice a monatomic step (1.38 Å) on the Pd(110) surface. It is thus suggested that Pd atoms are released and the C_{60} molecules sink into the Pd substrate in order to increase C_{60}–Pd coordination leading to stronger lateral interactions. This is supported by the strong lateral C_{60}–Pd interactions inferred from the analysis of Fig. 7.2. In Fig. 7.5 a model for the two bonding configurations is proposed. Whereas the metastable C_{60} species is bound on top of the unreconstructed Pd(110)(1×1) surface, the stable C_{60} species can be accommodated in a vacancy formed by 8 Pd atoms released out of the first two layers. The side view demonstrates the increased C_{60}–Pd coordination in the stable bonding configuration. A similar strictly local reconstruction has been reported for potassium on Cu(110) [182] and on Ag(110) [183]. The small discrepancy between expected and measured height difference might be related to the higher C_{60}–Pd coordination in the relaxed bonding configuration changing the electronic structure. Reorientation of the C_{60} cages upon annealing might also occur, this is addressed by XPD measurements presented in Section 7.2.

Thermal activation is typical for adsorbate-induced reconstructions, a detailed analysis of the mechanisms driving the reconstruction is given, e.g., in the report of Behm for alkali metal adsorption on fcc(110) transition metal surfaces [184]. Yao *et al.* report of a physisorbed C_{60} species on $Si(100)(2 \times 1)$ which becomes chemisorbed upon annealing to 870 K and appears smaller in STM images [185]. They propose that during the annealing procedure, the elevated temperature breaks the π bonds of Si dimers, providing two unsaturated dangling bonds on each dimer and allowing C_{60} molecules to bond covalently on top of them.

In the following the evolution of the first monolayer C_{60} on Pd(110) will be addressed. In the experiment shown here, C_{60} is adsorbed on the Pd(110) surface held at room-temperature followed by an high-temperature annealing cycle (700 K or as indicated). Evaporation of C_{60} on a Pd(110) surface held at the respective high temperature is equivalent. In Fig. 7.6 a series of STM images illustrating the growth of C_{60} on Pd(110) is reproduced, Fig. 7.6(a) shows a very low coverage.

The molecular height of the C_{60} molecules is (3.1 ± 0.2) Å indicating their relaxed bonding configuration. They are forming clusters with a preferential width of two molecules oriented roughly perpendicular to the close-packed Pd rows. On the flat terrace, Pd atoms desorbing from the step edges at elevated temperature aggregate into Pd islands (same height of 1.4 Å as Pd(110) monatomic steps). These islands are edged by C_{60} clusters. This demonstrates again the strong lateral C_{60}–Pd interaction, without C_{60} Pd islands on flat terraces do not form. During cool down C_{60} clusters form and pin the Pd. In Fig. 7.6(b) nearly the entire surface is covered with preferentially two molecules wide C_{60} stripes which extend roughly perpendicular to the close-packed Pd rows. In view of the preferential adsorption of the stable C_{60} species in vacancies along $[1\bar{1}0]$ (cf. Fig. 7.5), one might expect the formation of troughs by a missing row reconstruction, which would result in a linear ordering of C_{60} along $[1\bar{1}0]$. Apparently this is not the case and we thus believe that the surface reconstruction remains local and the ordering is mediated by elastic lattice distortions. Out of this structure a

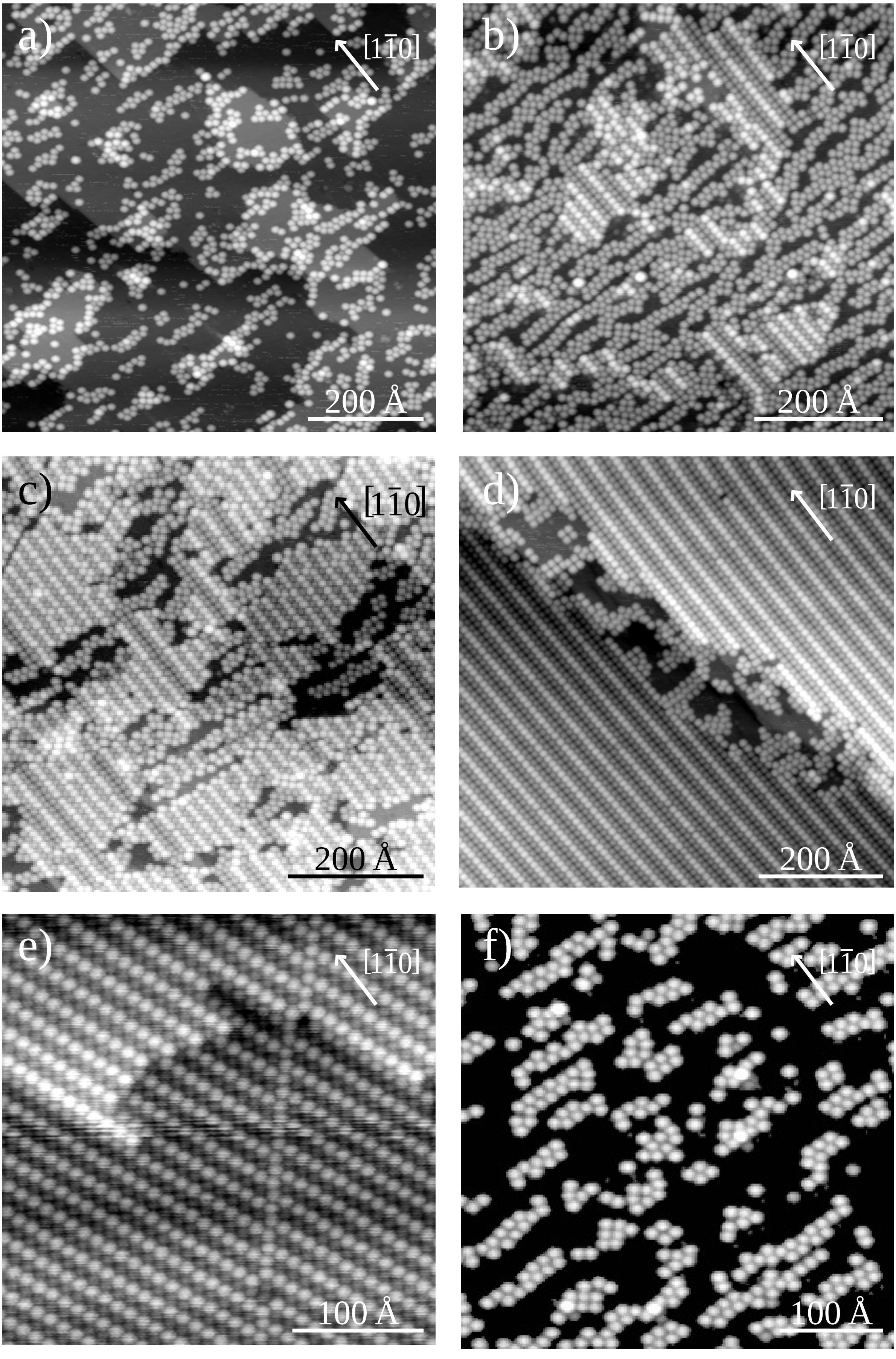

Figure 7.6: Figure caption see next page.

highly ordered phase consisting of alternating dark and bright rows along $[1\bar{1}0]$ evolves. Neighboring dark and bright rows are shifted by half a C_{60} molecular width and snap in, whereas neighboring dark rows are in phase. Upon increasing the coverage (Fig. 7.6(c)) the striped phase along $[1\bar{1}0]$ is covering nearly the entire surface. There are regions where dark and bright rows are alternating and others where there are *two* dark rows between bright ones. Upon annealing to about 970 K a well-ordered phase of alternating bright and two dark rows along $[1\bar{1}0]$ extends over the entire surface (cf. Fig. 7.6(d)) (in the middle of the image there is an atomic step). The height difference between bright and dark rows is about (1.5 ± 0.2) Å. This phase, which will be referred to as single-domain triple-stripe phase, will be discussed in Section 7.2 in more detail. Further increasing the coverage leads to another highly-ordered phase which can be extended over the entire surface (cf. Fig. 7.6(e)). It consists of alternating dark and bright rows. The rows are rotated by about ±22° with respect to $[1\bar{1}0]$ and thus two domains exist on the Pd(110) surface. As no more molecules can be adsorbed in the first layer, this phase will be referred to as saturated monolayer and is discussed in Section 7.2 in more detail.

Figure 7.6: Series of STM images demonstrating the growth of C_{60} on Pd(110) at elevated temperatures. **(a)** At low coverage C_{60} clusters with a preferential width of two molecules form; Pd substrate atoms desorbing from the steps nucleate in Pd islands on the terraces in between C_{60} clusters. **(b, c)** With increasing coverage a striped phase along the $[1\bar{1}0]$ substrate direction evolves which enlarges until nearly the entire surface is covered. Note that in the striped phase there are one or two dark rows between bright ones. **(d)** Well-ordered phase of alternating bright and two dark rows along $[1\bar{1}0]$ (annealed to about 970 K) which will be referred to as single-domain triple-stripe phase (in the middle of the image there is an atomic step). **(e)** Saturated monolayer of alternating bright and dark rows (annealed to about 920 K). The rows are rotated by about ±22° with respect to $[1\bar{1}0]$ and two domains exist on the Pd(110) surface. **(f)** Upon annealing to 1050 K the C_{60} molecules can be desorbed without decomposition whereby clusters with a preferential width of two molecules remain.

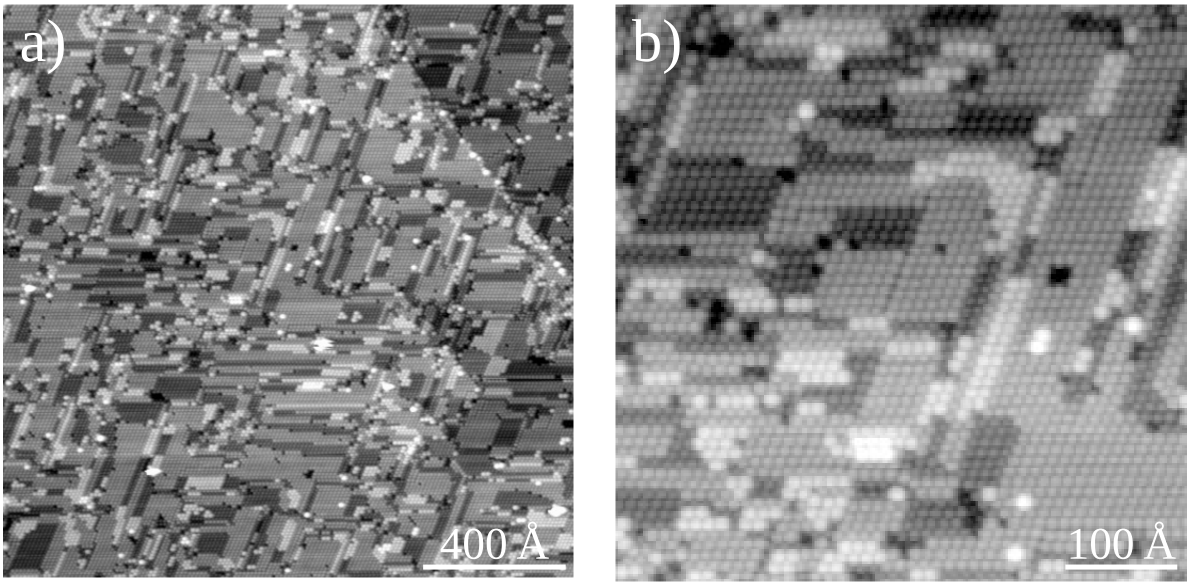

Figure 7.7: (a) Surface roughening due to Pd mass transport after an annealing cycle too moderate to reach the equilibrium structure. **(b)** Detail image of (a) showing the local close-packed ordering of the C_{60} molecules.

In contrast to Pt(111) and Ni(110), where the monolayer has been found to decompose at 1050 K and 760 K respectively [171,172], on Pd(110) C_{60} can be desorbed without decomposition at about 1050 K. Prior to complete desorption (∼1100 K) clusters of a preferential width of two molecules remain and finally a nearly clean Pd surface with some C_{60} molecules adsorbed at the upper step edges is obtained. This is insofar remarkable that both, palladium and nickel are *d*-metals and their electronic structure is quite similar (almost full *d*-band). On noble metal surfaces, e.g., Au(111) the desorption of C_{60} leaving a clean surface was reported and already occurs at temperatures of about 770 K [177].

Already the low coverage phase presented in Fig. 7.6(a) demonstrated that the mobility of substrate atoms plays a crucial role for the growth of C_{60} on Pd(110). This is corroborated by the STM topograph depicted in Fig. 7.7 showing a monolayer of C_{60} on Pd(110) which has been prepared by annealing an C_{60} multilayer to 720 K. All layers on top of the first physical monolayer of C_{60} do not - or only weakly - interact with the substrate [186] and start to desorb at about 455 K [180]. In Fig. 7.7(a) multilayers are thus completely desorbed. Apparently there is no long range order and the originally flat terrace is strongly roughened. Upon annealing to 920 K the highly ordered monolayer structure represented in Fig. 7.6(e) evolves in large flat domains. This clearly evidences that substantial Pd mass transport is involved in the formation of well-ordered monolayer structures. In the detail image of Fig. 7.7(b) the local ordering of the

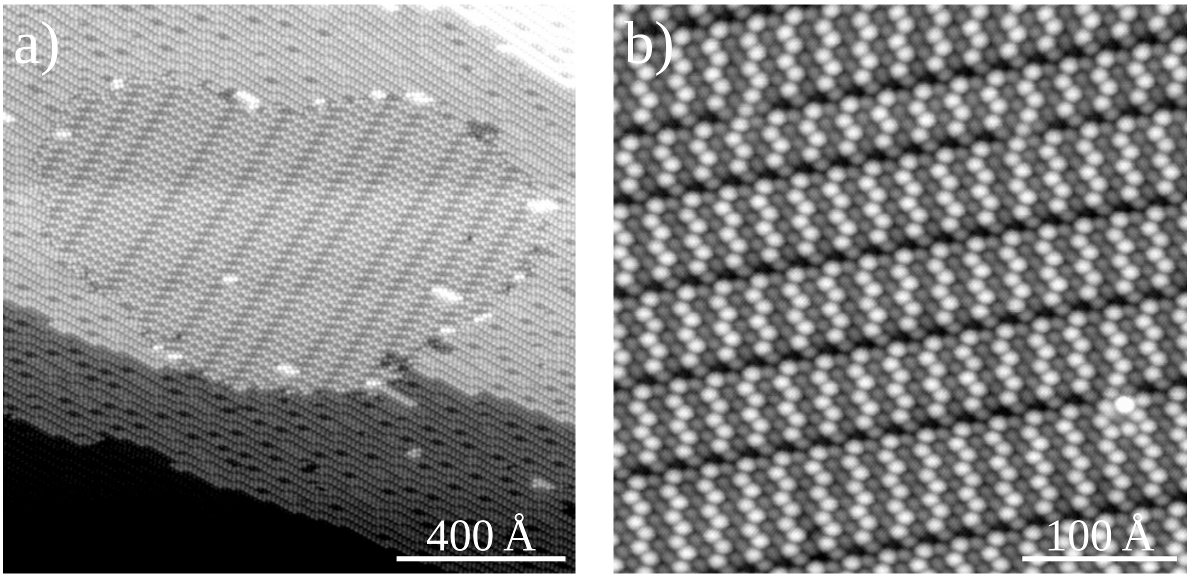

Figure 7.8: (a) Highly ordered phase on a length scale of several hundred Ångstroms which cannot be extended over the entire surface. **(b)** Detail image of (a) showing the local ordering of the C_{60} molecules.

C_{60} molecules is represented. The height difference between domains corresponds to a monatomic substrate step demonstrating surface restructuring. Surface reconstruction with large substrate mass transport has also been observed for another *d*-metal, namely for C_{60} adsorbed on Ni(110) [168].

In addition to the equilibrium structures discussed above, further highly ordered phases on a length scale of several hundred Ångstroms are occasionally found on the surface. Fig. 7.8 shows such a structure, which is never found to extend over the entire surface and represents a rather unusual situation. A detail image in Fig. 7.8(b) shows the local ordering of the C_{60} molecules. Similar zigzag pattern have been found for C_{60} on Ag(001) [187] and Au(110) [176]. Guidice *et al.* interpret the difference in height between dark and bright C_{60} molecules by different chemical bonding with the surface excluding any geometrical effect [187], but their argumentation is nonconclusive. Gimzewski *et al.* report of zigzag patterns along $[1\bar{1}0]$ on Au(110) with a height difference of approximately 1 Å independent of bias voltage [176]. They ascribe it to substrate reconstruction which allows a close-packed C_{60} structure with NN distance close to the bulk value.

In conclusion we have presented a detailed analysis of the mobility, interactions and growth of C_{60} on Pd(110). The diffusion of C_{60} on Pd(110) is preferentially along $[1\bar{1}0]$ and a mean energy barrier of ~1.5 eV is determined. Two differently bound C_{60} species are distinguished in STM images. The metastable, mobile C_{60} molecules become strongly chemisorbed and immobile upon annealing. This is ascribed to the release of substrate atoms resulting in higher C_{60}–Pd coordination in the stable bonding configuration. The mobility of Pd substrate atoms turns out to play a crucial role in the growth scenario and substantial Pd mass transport takes place. Whereas lateral C_{60}–C_{60} interactions are rather weak, the molecules do strongly interact with Pd substrate atoms. The ball shape of the molecular geometry provides the additional possibility of lateral π-bonding to Pd adatoms. Highly regular structures consisting of alternating dark and bright C_{60} rows could be fabricated.

In Section 7.2 we focus on the highly-ordered phases depicted in Figs. 7.6(d) and (e), the single-domain triple-stripe phase and the saturated monolayer, respectively.

7.2 C_{60} Ordering on the Local and the Mesoscopic Scale

The most reliable way to fabricate different well-ordered structures of C_{60} on Pd(110) is multilayer deposition and subsequent annealing to increasingly higher temperature. In Fig. 7.9 the evolution of the x-ray photoemission (XPS) C1s peak during such an experiment is depicted [1]. All spectra are taken with a MgK_α source ($\hbar\omega = 1253.6$ eV), an analyzer pass-energy of 20 eV, and are normalized to the same experimental conditions and incident photon flux. For comparison the multilayer peak is divided by 25. At about 455 K the multilayer desorption sets in [180]. Spectra taken after annealing to 570 K and up to 920 K are identical. The layers on top of the first physical monolayer do not - or only weakly - interact with the substrate and are already completely desorbed at these temperatures. Annealing to about 950 K and 1000 K leads to stepwise losses of C_{60} bound in the first physical monolayer. Finally, upon annealing to 1050 K, only a small amount of carbon remains on the surface. The multilayer peak is centered at $E_{\mathrm{kin}} = 969.8$ eV with a FWHM of 0.8 eV, the monolayer peaks are shifted by 0.4 eV to 970.2 eV with a FWHM of 1.1 eV and an asymmetric line shape towards higher binding energies. Similar results have been reported, e.g., for C_{60} on Au(110), Ag(111) [176] and on Pt(111) [173]. One origin for the different C1s peak positions might be the C_{60} charge state, since for a negatively charged molecule the photoemission line shows a chemical shift towards lower binding energies [173]. On the other hand a so called relaxation shift, reflecting the metal-substrate screening of the core-hole created in the photoabsorption process, is typical for molecules interacting

---

[1] The XPS/XPD experiments have been performed in the group of Prof J. Osterwalder at the university Zürich in collaboration with Dr C. Cepek, Dr R. Fasel and Dr T. Greber.

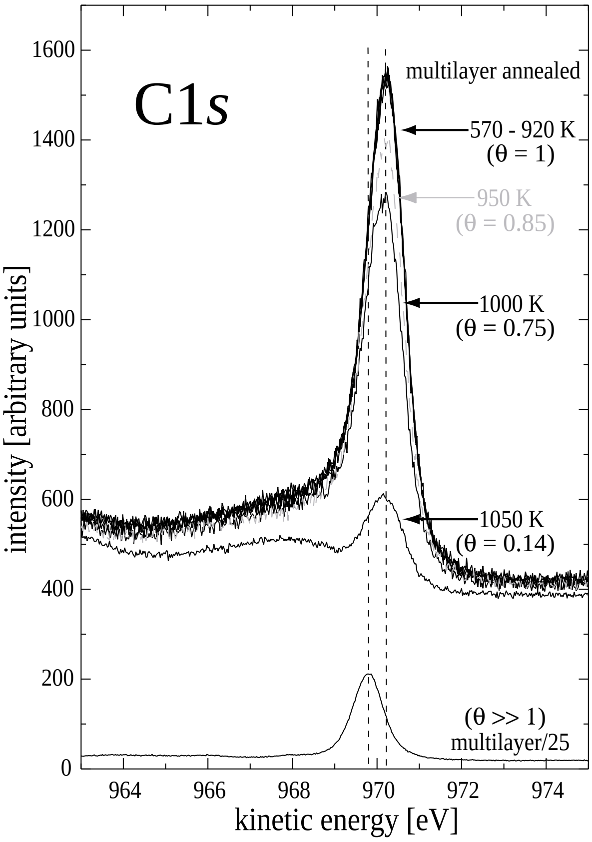

Figure 7.9: XPS C1*s* peaks (MgK_α, $\hbar\omega = 1253.6$ eV) of a multilayer C_{60} annealed to different temperatures normalized to photon flux (unannealed multilayer peak is divided by 25 for comparison). The multilayer is desorbed at 570 K; the saturated monolayer (defined as $\theta = 1$) is stable up to about 920 K. Further annealing leads to stepwise losses at approximately 950 K ($\theta = 0.85$) (measurements have been performed with a different pass energy, here a simulated spectrum (dashed gray) is included for illustration) and at 1000 K ($\theta = 0.75$). At 1050 K most molecules are desorbed. Note as well the characteristic shift between multilayer and monolayer peak position [173].

with metal surfaces [188]. For n-hexatriacontane, a saturated hydrocarbon, adsorbed on Cu(111) the shift of 0.8 eV is much larger, but in this case all C atoms are in the proximity of the substrate [189]. The broadening of the C_{60} monolayer peaks is thus associated with non-equivalent carbon sites on the molecule and/or creation of electron-hole pairs. For a detailed analysis of C_{60} C1*s* peak positions and line shapes see [173]. Defining the coverage of the films annealed to 570–920 K as 100% (saturated monolayer), the coverage of the films annealed to 950 K and 1000 K can be determined from the integrated peak intensities to be 85% and 75%, respectively. Upon annealing to 1050 K a coverage of 14% remains.

Annealing a multilayer C_{60} film to temperatures between 570 K and <920 K always results in monolayer films of identical coverage, but exhibiting no long-range order (cf. Fig. 7.7). At 920 K annealing temperature, still with the same saturated monolayer coverage, a well-ordered structure is formed, consisting of alternating dark and bright rows which are rotated by ±22.0° with respect to the close-packed $[1\bar{1}0]$ surface direction (cf. Fig. 7.10). Locally, the C_{60} molecules form a close-packed quasihexagonal arrangement. Due to the twofold symmetry of the Pd(110) surface two domains exist. As can be seen in the inset, neighboring rows are shifted by half a molecular width and snap in. The height difference between dark and bright rows is (1.3 ± 0.2) Å, which is about the height of a monatomic step on the Pd(110) surface (1.38 Å). This height variation is independent of the tunneling parameters and is thus interpreted as topographic height. In Fig. 7.10(b) the corresponding LEED pattern is presented. It is taken with an electron energy of 38.1 eV and the surface at room-temperature. The LEED structure reflects the two domains visible in STM data. The structure is determined to be a $\left(\begin{smallmatrix} 7 & -1 \\ \mp 2 & \pm 5 \end{smallmatrix}\right)$-structure, where ± 5 and ∓ 2 correspond to the two possible domain orientations. The simulated spots for this unit cell are overlaid in Fig. 7.10(b), spots from the two domains are indicated in black and grey, respectively. With the combination of STM and LEED images a preliminary model as sketched in Fig. 7.10(c) is developed. Each C_{60} molecule is represented by a circle, the inner diameter corresponds to the diameter of C_{60} (all nuclei are on a sphere with 7.1 Å diameter) and the outer to the C_{60} bulk nearest neighbor distance of 10.04 Å [190]. The 353.0 $Å^2$ large unit cell contains 4 C_{60} molecules, giving 88.2 $Å^2$ per C_{60} molecule. C_{60} forms a close-packed quasihexagonal overlayer which is expanded by 1% with respect to the bulk C_{60} close-packed plane. The intermolecular distances are 10.38 Å along $[7\bar{7}\bar{2}]$ (3% expansion), 9.89 Å along $[\bar{1}15]$ (1% compression) and 10.17 Å along $[2\bar{2}1]$ (1% expansion) (taking the STM height difference of 1.3 Å into account). Similar behavior has been reported for other single crystal metal surfaces and is attributed to C_{60}–C_{60} interactions dominating over C_{60}–substrate interactions [174, 191–193]. Subtle variations in the hexagonal overlayer structure have often been observed, but the bulk C_{60} NN distance is in most cases closely retained. In the case of C_{60} on Cu(110) the C_{60} intermolecular distances vary from 9.6 Å to 11.1 Å depending on which neighboring pairs are considered [168, 169].

In our model, the angle between the C_{60} rows and $[1\bar{1}0]$ is 22.0°, which fits well with the measured angle between the domains of ~45° in the STM images. This model is consistent with the lateral structures as seen in STM and with the LEED data, but it does not explain the measured height difference of dark and bright rows. In the model C_{60} molecules occupy all four different high symmetry adsorption sites on the

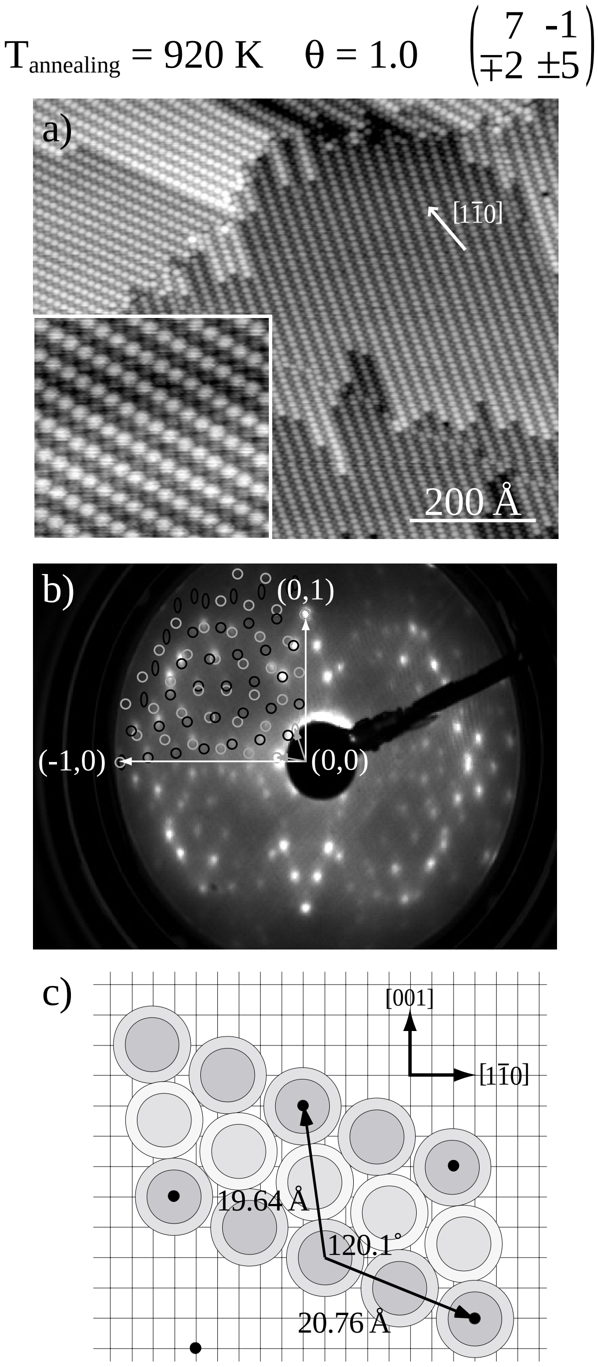

Figure 7.10: **(a)** STM image of the saturated monolayer showing two domains rotated by ~45°. Alternating bright and dark rows which are shifted by half a molecular width are clearly discernible in the inset. **(b)** Corresponding LEED image with simulated spots of the $\begin{pmatrix} 7 & -1 \\ \mp 2 & \pm 5 \end{pmatrix}$-structure (2 domains) overlaid. **(c)** Schematic real space model on fcc(110)(1 × 1) substrate: The unit cell contains 4 C_{60} molecules, the area per C_{60} molecule amounts to 88.2 Å^2.

Pd(110)(1×1) surface, namely the on-top, short-bridge, long-bridge and fourfold hollow site. In a hard sphere model the respective height difference between these different adsorption sites is calculated to be 0.2 Å and should thus be comparable within a row and between dark and bright rows.

As already pointed out in the description of the growth scenario (Section 7.1) the rearrangement of Pd substrate atoms plays a crucial role in the film evolution. We therefore suggest that the different heights of bright and dark rows are due to a surface reconstruction as it was proposed for C_{60} on Ni(110). Murray *et al.* reported significant interfacial restructuring of the substrate via the addition/removal of Ni [001] rows [168], which increases the C_{60} coordination to the substrate. They reported that the energetic proximity of the C_{60} LUMO and metal *d*-states leads to strong hybridization. In view of the similar electronic structures of nickel and palladium, especially the almost full *d*-band, and the comparable work functions of 5.04 eV and 5.13 eV [194], a similar scenario could be expected for Pd(110). Even on chemically inert surfaces like Au(110), substrate reconstruction and substantial Au mass transport has been reported [176]. Other possibilities would be electronic effects, possibly related to different orientations of the C_{60} cages. This has been proposed by Guidice *et al.* for C_{60} adsorbed on Ag(001) where bright and dim C_{60} molecules were observed in STM images as well [187]. In order to clarify whether differently oriented C_{60} molecules are present in the dark and bright C_{60} rows on Pd(110) the orientational ordering was investigated with XPD and will be discussed below.

The monolayer structures were prepared by slowly heating a C_{60} multilayer on Pd(110) in front of the LEED optics until sharp spots evolved. During this procedure we recognized that the LEED spots are sharper at high temperature than after cooling down to room-temperature. Normally the intensity of LEED spots is expected to decrease with increasing temperature due to the Debye Waller factor. We have not performed extensive temperature dependent I-V-analysis but the ordering seems to be improved at higher temperatures.

Between the saturated monolayer and the single-domain triple-stripe phase at about $T = 950$ K another structure evolves showing sharp LEED spots. During the STM study of the growth scenario alternating dark and bright rows along $[1\bar{1}0]$ have been found on small areas below monolayer coverage. This structure can be associated with the LEED pattern and an STM image is shown in Fig. 7.11(a). Regions of alternating bright and dark rows, two dark rows in between bright ones and bare Pd substrate coexist. The LEED pattern (cf. Fig. 7.11(b)) is taken with an electron energy of 38.1 eV and the surface at room-temperature. The structure is easily determined to be a (4×5)-

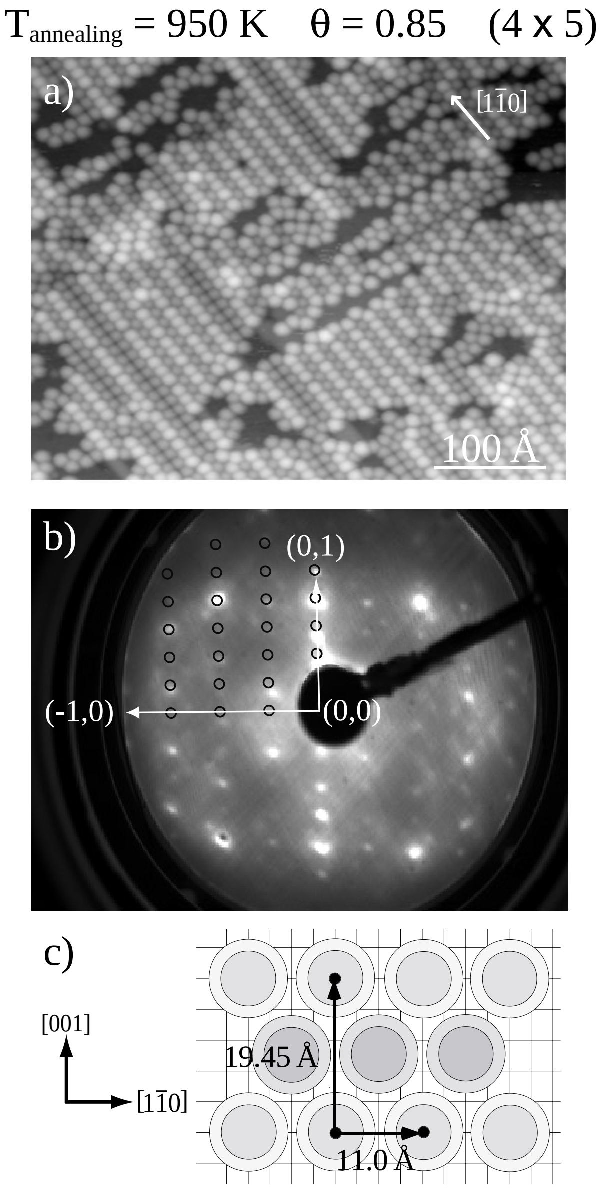

Figure 7.11: (a) STM image showing domains of alternating bright and dark rows along $[1\bar{1}0]$ prepared by submonolayer C_{60} deposition at 720 K. This structure can be prepared over the entire surface by annealing a multilayer C_{60} to $T = 950$ K. **(b)** Corresponding LEED image with simulated (4×5)- spots overlaid. **(c)** Schematic real space model on fcc(110)(1×1) substrate: The unit cell contains 2 C_{60} molecules, the area per C_{60} molecule amounts to 107.0 Å^2 fitting well to the measured C1s-intensity of 85% with respect to the saturated monolayer.

structure (simulated spots are overlaid). In Fig. 7.11(c) a preliminary model compatible with STM and LEED observations is sketched. 2 C_{60} molecules are in the 214.0 Å^2 large unit cell giving 107.0 Å^2 per C_{60} molecule. The calculated relative coverage of 82% is in good agreement with the value of 85% determined by means of XPS. Whereas in the case of the saturated monolayer the molecular rows are rotated by ±22.0° with respect to $[1\bar{1}0]$, in the (4×5)-structure the rows are aligned along the close-packed Pd rows and thus only one domain exists on the Pd(110) surface. The C_{60} molecules are centered in a local quasihexagonal structure with intermolecular distances of 11.0 Å along $[1\bar{1}0]$ (10% expansion), and 11.3 Å along $[4\bar{4}5]$ and $[\bar{4}45]$ (12% expansion) (taking the STM height difference of 1.5 Å into account). In this model only two different adsorption sites on the Pd(110)(1×1) surface would be occupied by C_{60} molecules, we have chosen the on-top site for the bright rows and the long-bridge for the dark rows. Not only the lateral ordering but also the rows seen in STM images are explained qualitatively. Quantitatively, the height difference between dark and bright C_{60} rows of 0.4 Å from the hard sphere model is significantly lower than the measured value.

Fig. 7.12(a) shows an STM image of the single-domain triple-stripe phase which evolves upon annealing to 1000 K. The coverage determined by means of XPS amounts to 75% relative to the saturated monolayer. Whereas in the case of the saturated monolayer and the (4×5)-structure there are alternating dark and bright rows, this structure consists of *two* dark rows in between bright ones. Similar to the (4×5)-structure the rows run along $[1\bar{1}0]$, resulting in only one domain on the Pd(110) surface. Neighboring dark and bright rows are shifted by half a molecular width and snap in, whereas neighboring dark rows are in phase. The height difference between dark and bright rows is $(1.5 \pm 0.2$ Å) which is approximately the height of a monatomic step on the Pd(110) surface. In Fig. 7.12(b) the corresponding LEED image is shown. It is taken with an electron energy of 38.1 eV and the surface at room-temperature. The structure is easily determined to be a rectangular (4×8)-structure (simulated spots are overlaid), confirming that the C_{60} rows are aligned parallel to the close-packed Pd rows along $[1\bar{1}0]$. The area of the unit cell amounts to 342.3 Å^2. With the combination of STM and LEED images the preliminary model sketched in Fig. 7.12(c) is developed. The unit cell contains 3 C_{60} molecules giving 114.1 Å^2 per C_{60} molecule. The relative coverage of 77% is in good agreement with the measured XPS value of 75%. The bright C_{60} molecules are centered in a local quasihexagonal structure with the same intermolecular distances as in the (4×5)-structure. The distance between neighboring dark rows is 11.7 Å. As in the (4×5)-structure, only two different adsorption sites of the Pd(110)(1×1) surface would be occupied by C_{60} molecules.

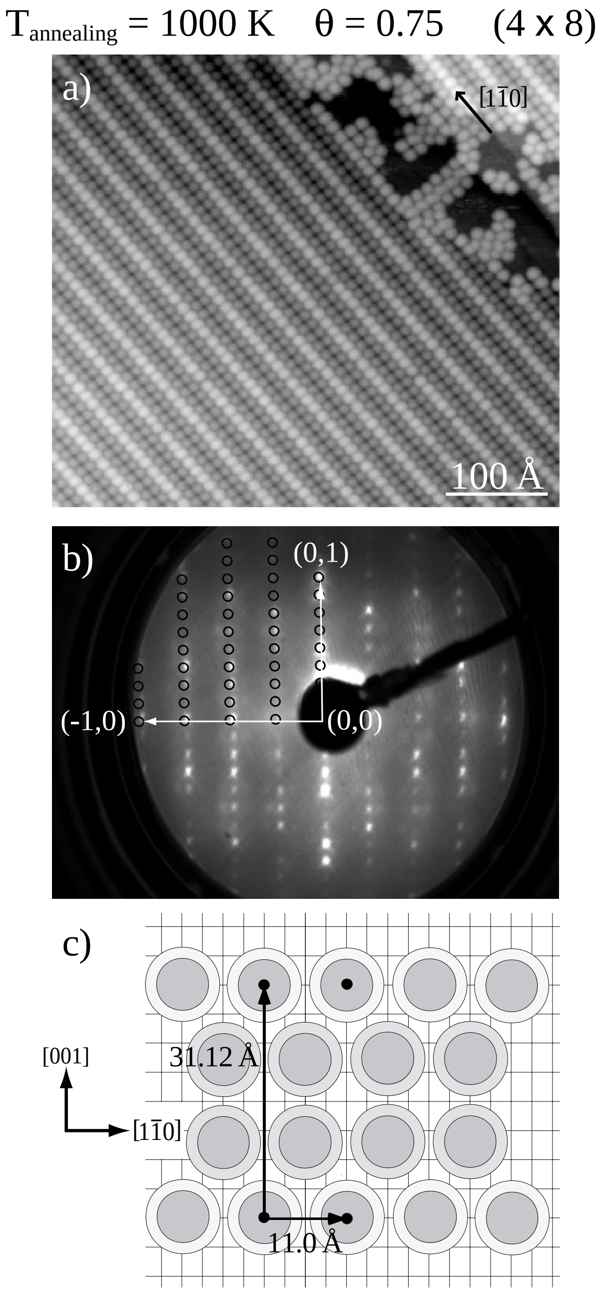

Figure 7.12: **(a)** STM image of single-domain triple stripe phase consisting of alternating bright and two dark rows oriented along [1$\bar{1}$0]. **(b)** Corresponding LEED image with simulated spots of 4 × 8-structure overlaid. **(c)** Schematic real space model on fcc(110)(1 × 1) substrate: The unit cell contains 3 C_{60} molecules, the area per C_{60} molecule amounts to 77.3 Å^2 fitting well to the measured C1s-intensity of 75% with respect to saturated monolayer.

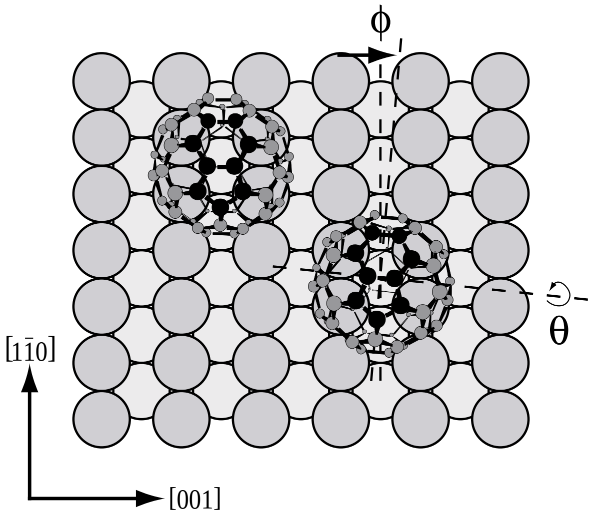

Figure 7.13: Model of the typical 5-6 bonding configuration of C_{60} on a fcc(110) surface. The upper left C_{60} molecule is centered on a bond between a five- and a six-membered ring (drawn in black); the 5-6 bond is aligned along [001]. The bottom right C_{60} molecule is slightly tilted away from this high symmetric bonding configuration by an azimuthal angle ϕ and a polar tilt θ.

In the models developed so far, C_{60} has been regarded as ball shaped neglecting the exact molecular shape consisting of 5-membered and 6-membered rings. In recent work it has been suggested that the internal molecular structure in STM images can be used to determine the molecular orientation of adsorbed C_{60} on Au(111), Ag(111) [174], Cu(111) [192] and Si(111)(7 × 7) [195]. But this is a quite delicate procedure, strongly depending on the nature of the STM tip and the quality of model calculations. A more reliable way to determine the molecular orientation of adsorbed C_{60} with high precision is x-ray photoelectron diffraction (XPD). XPD patterns are a real space “fingerprint” of the molecular orientation, by symmetry arguments alone, restrictions of the possible molecular orientations can immediately be made. A variety of molecular orientations has been observed on different single crystal metal surfaces. On Cu(111) and Al(111) C_{60} is adsorbed on a six-membered ring, on Al(001) on a C edge atom and on Cu(110) and Ni(110) [196] on a 5-6 bond [166,169]. In the 5-6 bonding configuration the molecule is adsorbed on a bond between a five- and a six-membered ring of the C_{60} cage. This is illustrated in Fig. 7.13; the 5-6 bond is aligned along the [001]-direction of the fcc(110) surface.

XPD measurements of two well-ordered structures, i.e., the saturated monolayer and single-domain triple-stripe phase, have been performed (cf. Figs. 7.14 and 7.15). The saturated monolayer consists of alternating dark and bright rows, whereas in the single-domain triple-stripe phase there are *two* dark rows in between bright ones. As already mentioned above, Guidice *et al.* speculated that different molecular orientations are responsible for dark and bright rows seen in the STM images of C_{60} on Ag(001) [187]. The different ratios of these two species of 1:1 in the saturated monolayer and 2:1 in the single-domain triple-stripe phase of C_{60} on Pd(110) allows to directly check this hypothesis. As the XPD patterns are related in a straightforward way to the molecular orientation of the C_{60} molecules within the monolayer film, it immediately follows that they should be different for the two films if the molecules within dark and bright rows were oriented differently. In Fig. 7.14(a) and Fig. 7.15(a) the respective XPD patterns of the saturated monolayer and the single-domain triple-stripe phase are shown. The XPD patterns are identical which unambiguously demonstrates that *the orientation of the C_{60} cages in the dark and bright rows is identical.*

Single-scattering cluster (SSC) calculations performed for different high symmetry orientations on a twofold substrate [72] reveal that the XPD patterns are typical for a 5-6 bonding configuration (cf. Fig. 7.13). In order to exactly determine the molecular orientation, we have performed an extensive R-factor analysis comparing the experimental C1s diffraction patterns to SSC calculations, allowing the C_{60} molecules to rotate away from the ideal 5-6 orientation. The SSC calculations for the optimized molecular orientation and the resulting R-factors for the saturated monolayer and the single-domain triple-stripe phase are shown in Figs. 7.14(b), (c) and Figs. 7.15(b), (c), respectively. The SSC calculations nicely reproduce the experimental data. As can be seen from the R-factor plots (Fig. 7.14(c) and Fig. 7.15(c)), obtained by azimuthal rotation and polar tilt of the C_{60} molecules away from the symmetric 5-6 orientation, the best agreement for both films is achieved at an azimuthal rotation $\phi = \pm(5 \pm 2)^\circ$ ($\phi = 0^\circ$ corresponds to an orientation of the 5-6 bond along [001]). An identical azimuthal rotation is reported for C_{60} adsorbed on Cu(110) [169]. The polar tilt θ is basically 0° for the present case whereas on Cu(110) the C_{60} molecules are tilted by $+4.5^\circ$ [169]. An interpretation of the molecular orientations is given below.

$$T_{\text{annealing}} = 920\text{ K} \quad \theta = 1.0 \quad \begin{pmatrix} 7 & -1 \\ \mp 2 & \pm 5 \end{pmatrix}$$

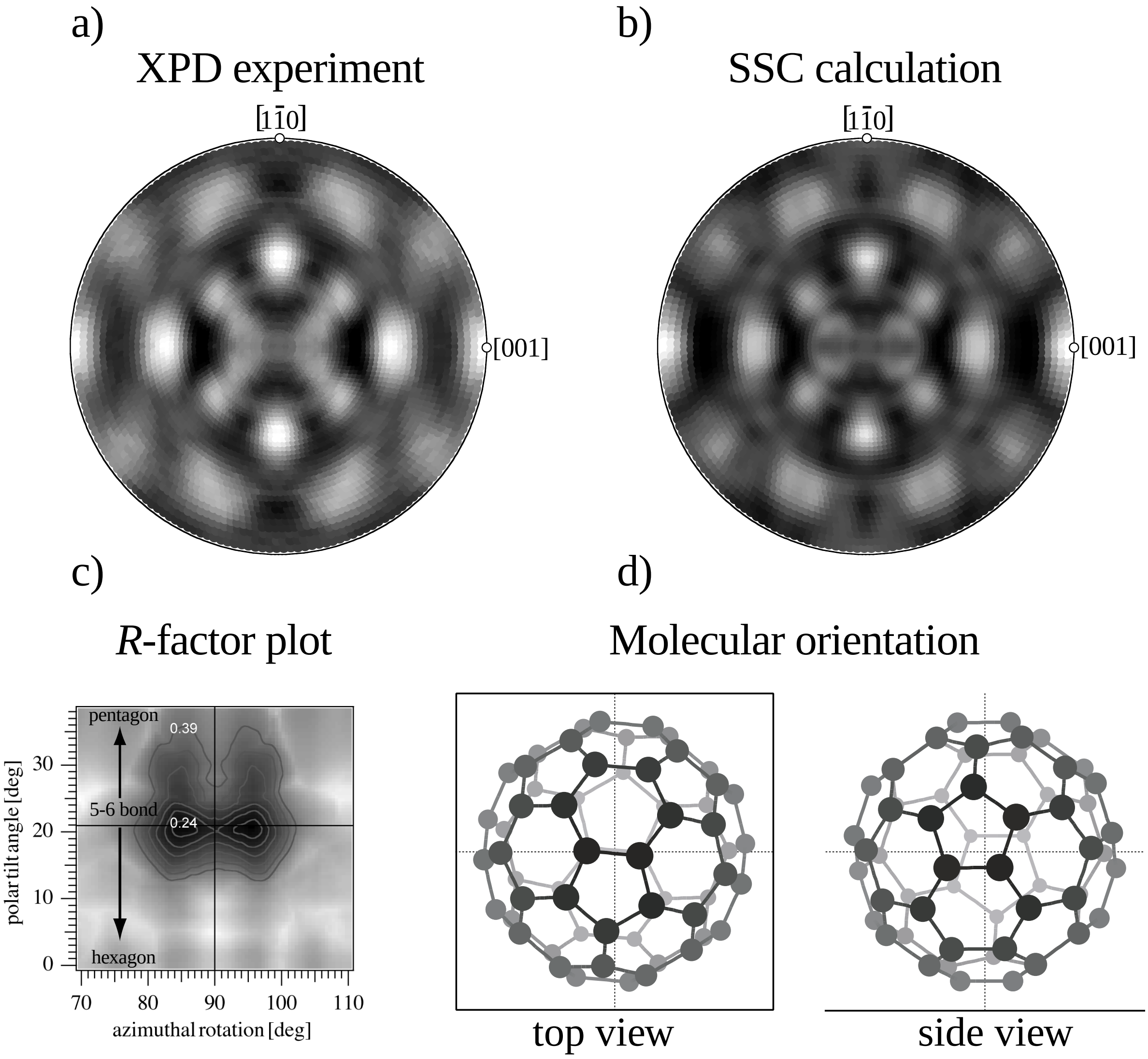

Figure 7.14: **(a)** Experimental C1*s* XPD pattern ($E_{\text{kin}} = 970$ eV) from the saturated C_{60} monolayer. **(b)** SSC calculation for the optimized molecular orientation which fits the experimental data in (a). **(c)** R-factor plot obtained by azimuthal rotation and polar tilt of the C_{60} molecules away from the symmetric 5-6 orientation, as schematically shown in Fig. 7.13. The symmetric 5-6 bond corresponds to $\theta = 20.9°$ and $\phi = 90°$. **(d)** Corresponding molecular orientation for $\Delta\phi = +5°$.

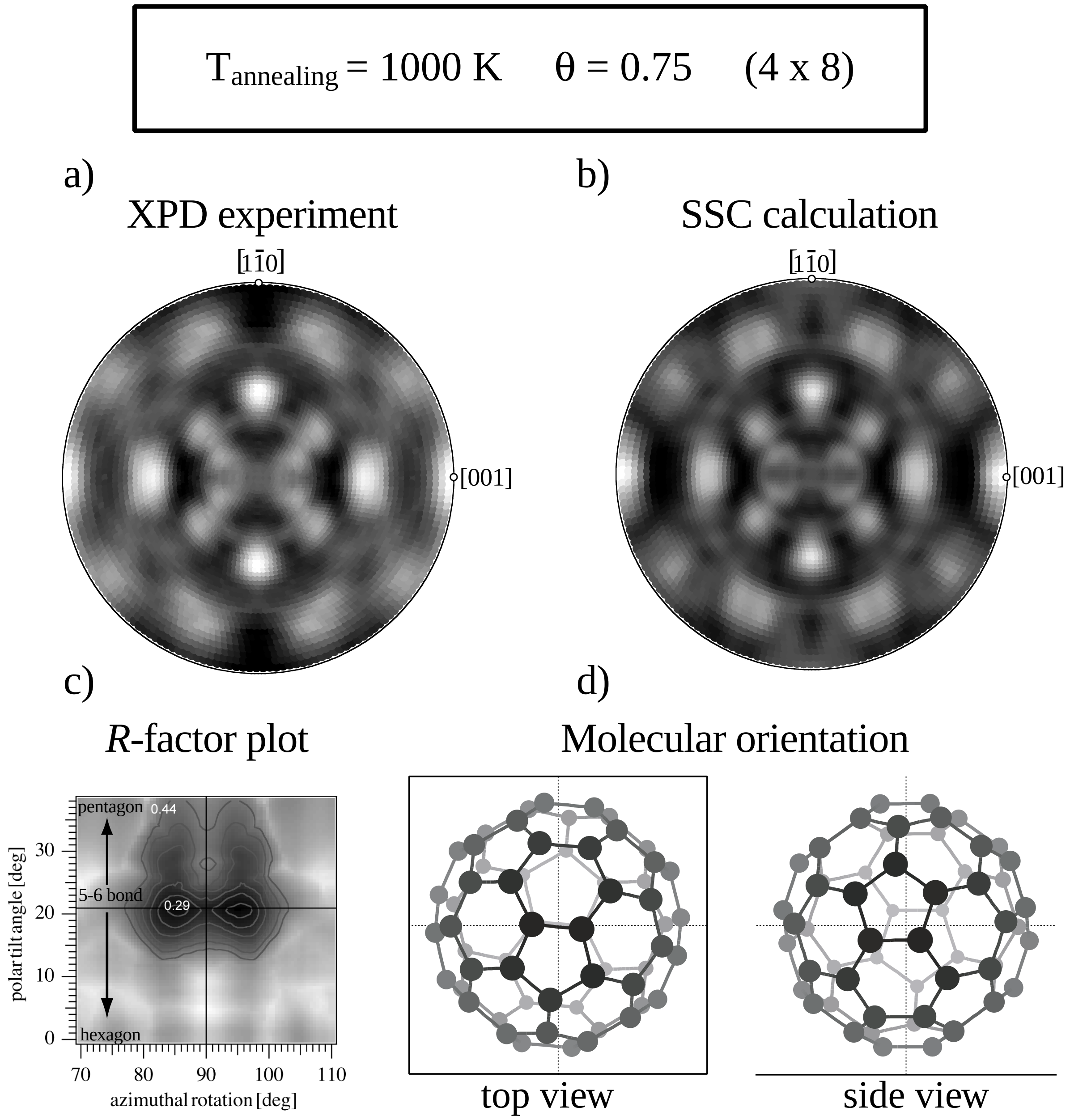

Figure 7.15: **(a)** Experimental C1s XPD pattern ($E_{\text{kin}} = 970$eV) from single-domain triple-stripe phase. **(b)** SSC calculation for the optimized molecular orientation which fits the experimental data in (a). **(c)** R-factor plot obtained by azimuthal rotation and polar tilt of the C_{60} molecules away from the symmetric 5-6 orientation, as schematically shown in Fig. 7.13. The symmetric 5-6 bond corresponds to $\theta = 20.9°$ and $\phi = 90°$. **(d)** Corresponding molecular orientation for $\Delta\phi = +5°$. The XPD data are nearly identical with the ones for the saturated monolayer represented in Fig. 7.14.

With the real space models presented now all aspects of STM, LEED and XPD data are rationalized comprehensively. In Fig. 7.16 and Fig. 7.17 the real space models of the (4×5)- and (4×8)-structure are presented, respectively. Whereas the bright molecular rows are composed of C_{60} molecules adsorbed in a vacancy formed by released Pd atoms of the first layer, the dark molecular rows consist of C_{60} molecules adsorbed in a vacancy formed by Pd atoms released out of the first *two* layers. On the right side the C_{60} molecules are omitted to illustrate the different vacancies. As inferred from the growth study of C_{60} in Section 7.1 the reconstruction is always local and thus isolated vacancies are used in the real space model and no extended troughs along $[1\bar{1}0]$. The alternating dark and bright rows are clearly discernible in the side view along [001]. The height difference between the rows corresponding to a monatomic step (1.38 Å) is in agreement with the observed height difference of (1.5 ± 0.2) Å in STM images. The C_{60} molecules in the dark rows are identically bound as the stable C_{60} species at low coverage (cf. Fig. 7.5) explaining the similar observed height of (3.1 ± 0.2) Å. Apparently this geometry allows for strong bonding due to high C_{60}–Pd coordination. The C_{60} molecular height in the bright rows is (4.6 ± 0.2) Å, i.e., in between the one of the stable and of the metastable C_{60} species found at low coverage. This is apparent from the proposed model: C_{60} molecules in the dark rows are adsorbed in a two layer deep vacancy (as the stable C_{60} species), C_{60} molecules in the bright rows in a one layer deep vacancy, and the metastable C_{60} species on top of the unreconstructed Pd surface. The other side views demonstrate the coordination of the C_{60} cage to the nearest Pd atoms of the different layers in the two bonding configurations. All C_{60} molecules are facing with a 5-6 bond to the surface which is rotated by $\phi = \pm(5 \pm 2)^\circ$ away from the [001] direction as determined by XPD.

In Fig. 7.18 a model is depicted explaining the molecular stripes of the rotated $\left(\begin{smallmatrix} 7 & -1 \\ \mp 2 & \pm 5 \end{smallmatrix}\right)$-structure with an analogue surface restructuring. Whereas the bonding sites within a molecular row are identical in the (4×5)- and (4×8)-structure, two different bonding sites, shifted by half a lattice constant in $[1\bar{1}0]$ have to be assumed in the $\left(\begin{smallmatrix} 7 & -1 \\ \mp 2 & \pm 5 \end{smallmatrix}\right)$- structure. The height difference between adsorption in fourfold hollow and long-bridge sites is about 0.2 Å in a hard sphere model, which is small compared to the height difference of (1.3 ± 0.2) Å between dark and bright molecular rows. Pedersen *et al.* report of C_{60} on Cu(110) [167]. They find a height difference of about 0.1 Å between adsorption in fourfold hollow and long-bridge sites only in high resolution STM images. In our STM data this feature was not observed.

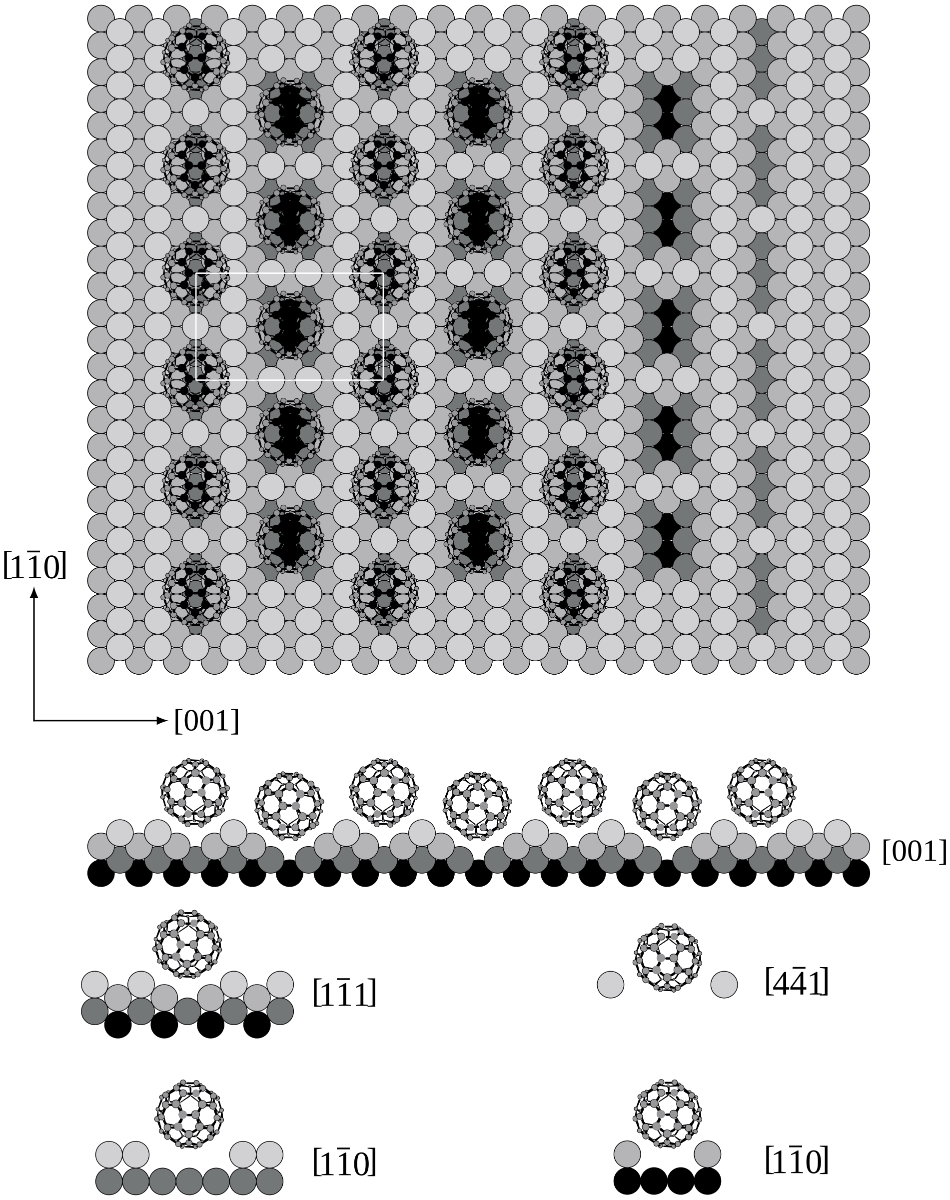

Figure 7.16: Real space model of the (4 × 5)-structure. The bright molecular rows seen in STM correspond to C_{60} molecules adsorbed in a vacancy formed by Pd atoms released out of the first layer. The dark molecular rows correspond to C_{60} molecules adsorbed in a vacancy formed by Pd atoms released out of the first *two* layers. On the right side the C_{60} molecules are omitted to illustrate these vacancies. In the side view along [001] the alternating dark and bright rows are clearly discernible. The other side views demonstrate the coordination of the C_{60} cage to the nearest Pd atoms of the different layers in the two bonding configurations along indicated directions. All C_{60} molecules are facing with a 5-6 bond to the surface which is rotated by $\phi = \pm(5 \pm 2)^\circ$ away from the [001] direction.

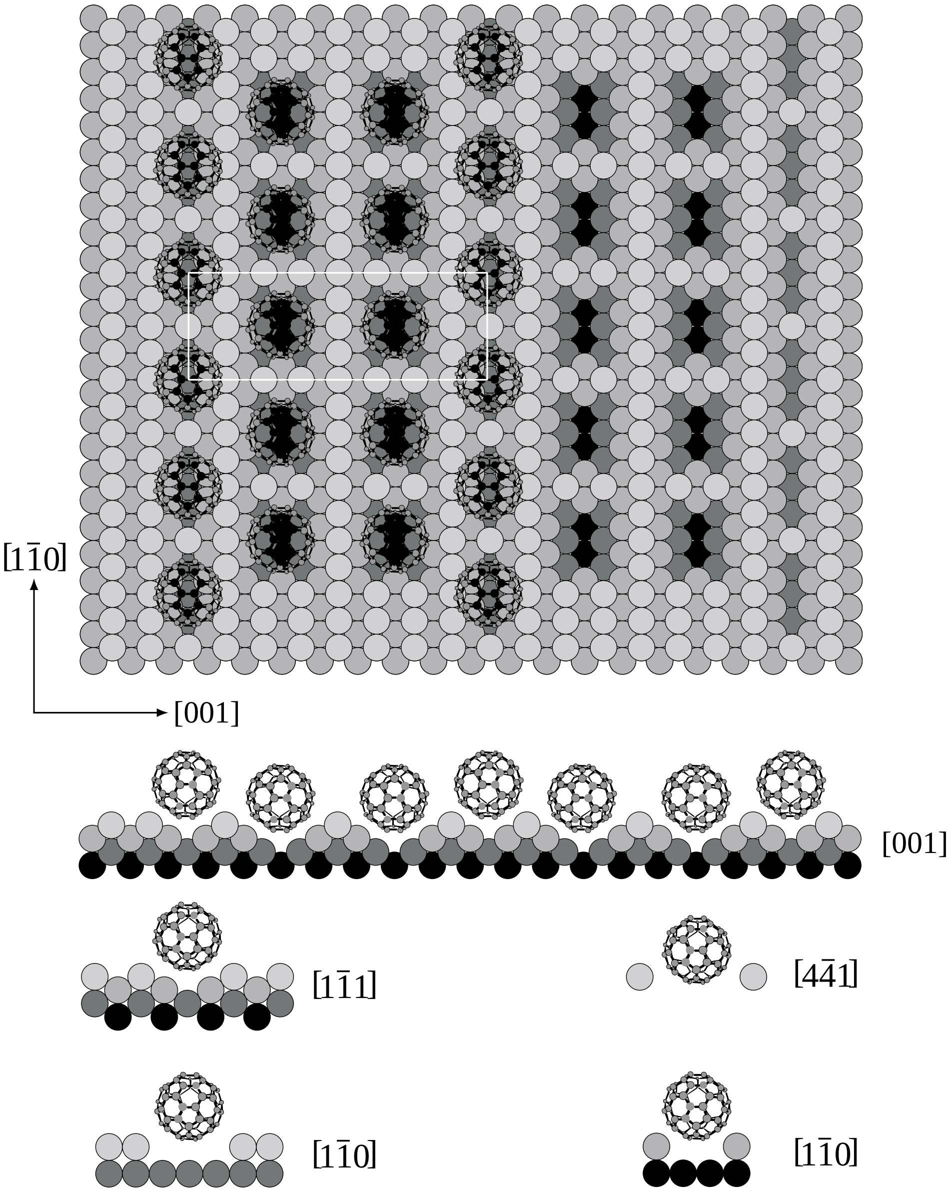

Figure 7.17: Real space model of the (4 × 8)-structure. Dark and bright C_{60} rows can be similarly explained as in the (4 × 5)-structure. For a detailed description see the figure caption of Fig. 7.16.

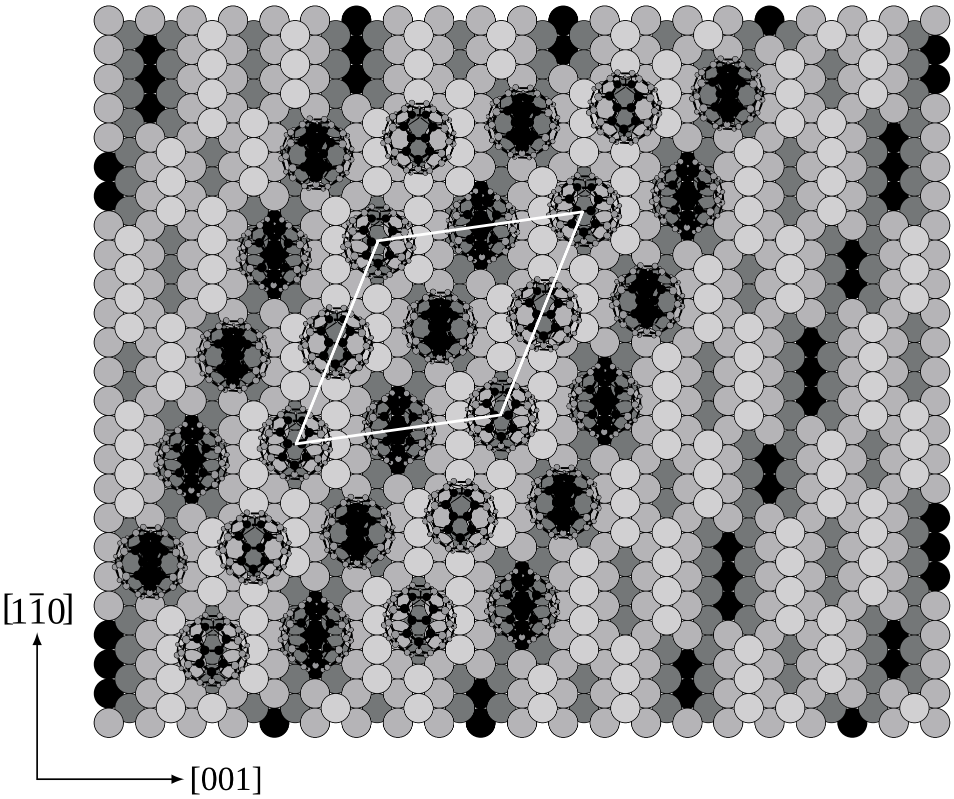

Figure 7.18: Real space model of the $\begin{pmatrix} 7 & -1 \\ \mp 2 & \pm 5 \end{pmatrix}$-structure. Dark and bright C_{60} rows can be similarly explained as in the (4 × 5) and (4 × 8)-structure. For a detailed description see the figure caption of Fig. 7.16.

As discussed in Section 7.1, room-temperature deposited C_{60} molecules on Pd(110) at low coverage are metastable. They are bound on top of the unreconstructed Pd(110) surface and are imaged as (5.5 ± 0.2) Å high protrusions. Upon annealing Pd atoms are released out of the first two layers and the C_{60} molecules sink into the formed vacancy leading to an height of (3.1 ± 0.2) Å in STM. This bonding is identical to the bonding of C_{60} molecules in the dark rows of the monolayer structures. Reorientation of the C_{60} cage might be involved in the thermally activated transition from the metastable to the stable C_{60} species. Thus XPD for a small coverage ($\theta = 0.4$) *room-temperature* deposited C_{60} on Pd(110) was performed. The resulting XPD pattern is reproduced in Fig. 7.19(a). Whereas the overall symmetry is unchanged, the relative intensities of the prominent peaks are inverted. For the two monolayer phases (Figs. 7.14 and 7.15) the spots along [1$\bar{1}$0] are the most prominent. In contrast, the spots along [001] dominate for the room-temperature deposited C_{60} molecules. From the unchanged symmetry it can be immediately concluded that the metastable C_{60} species are also adsorbed on a 5-6 bond. SSC calculations have been performed which reproduce the experimental XPD pattern (cf. Fig. 7.19(b)). They reveal that the 5-6 bonds are rotated away from

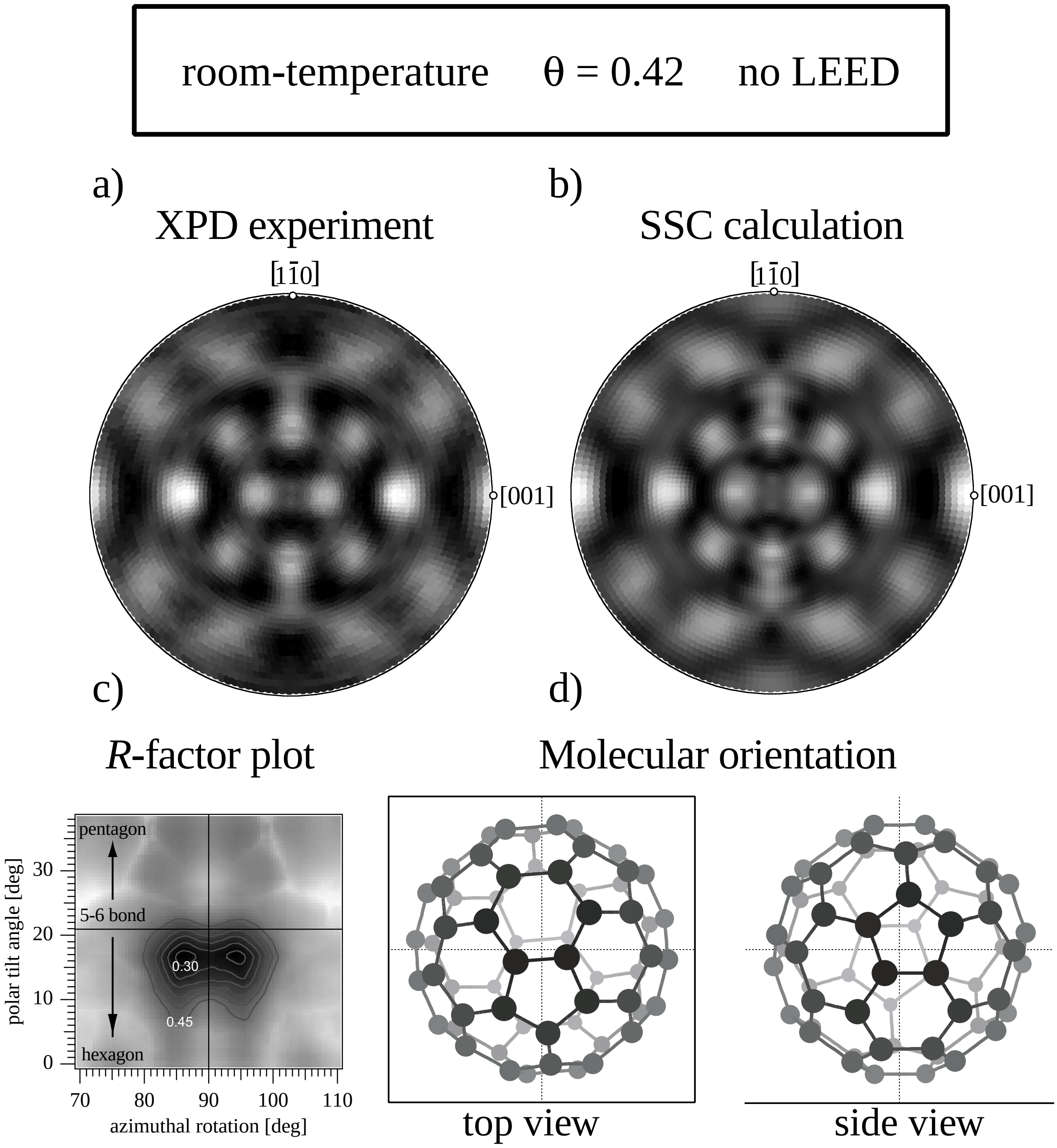

Figure 7.19: **(a)** Experimental C1*s* XPD pattern ($E_{\mathrm{kin}} = 970$eV) from a low coverage C_{60} on Pd(110) evaporated at *room-temperature*. Whereas the symmetry is identical to the well-ordered phases shown in Fig. 7.14 and Fig. 7.15 the relative intensities of the prominent peaks are inverted. **(b)** SSC calculation for the optimized molecular orientation which fits the experimental data in (a). **(c)** R-factor plot obtained by azimuthal rotation and polar tilt of the C_{60} molecules away from the symmetric 5-6 orientation, as schematically shown in Fig. 7.13. The symmetric 5-6 bond corresponds to $\theta = 20.9°$ and $\phi = 90°$. **(d)** Corresponding molecular orientation for $\Delta\phi = +5°$ and $\Delta\theta = -5°$.

the [001] direction by $\phi = \pm(5 \pm 2)^\circ$ and the metastable C_{60} species are tilted by $\theta = -(5 \pm 1)^\circ$ (cf. Figs. 7.19(c) and (d)).

The results for the different phases are best visualized by comparing the R-factor plots and the corresponding molecular orientations. In Fig. 7.20 the data of the $\left(\begin{smallmatrix} 7 & -1 \\ \mp 2 & \pm 5 \end{smallmatrix}\right)$-structure (a) (same molecular orientation as in the (4×8)-structure) and of the room-temperature deposited metastable C_{60} molecules on Pd(110) (b) are assembled together with data of a monolayer C_{60} on Cu(110), which has been studied recently [169]. For all systems the azimuthal angle is identical and amounts to $\phi = \pm(5 \pm 2)^\circ$ meaning a rotation of the 5-6 bond away from the $[1\bar{1}0]$ direction. The polar tilt is systematically different for these three systems: Basically $\theta = (0 \pm 1)^\circ$ for the high-temperature annealed well-ordered structures on Pd(110), $\theta = -(5 \pm 1)^\circ$ for metastable C_{60} on Pd(110) and $\theta = +(4.5 \pm 1)^\circ$ for a monolayer C_{60} on Cu(110) (annealed to 720 K). Whereas a polar tilt of $\theta = 0^\circ$ corresponds to bonding on a high symmetric 5-6 bond, positive polar tilts incline the molecule towards the bottommost pentagon and negative tilts towards the bottommost hexagon of the C_{60} cage.

The significant different polar tilt might be interpreted as follows: In the high-temperature annealed well-ordered C_{60} structures on Pd(110) molecules are bound in vacancies which configuration allows for efficient lateral interaction to Pd atoms without tilting. The room-temperature deposited metastable C_{60} molecules adsorb on top of the unreconstructed Pd(110) substrate. Presumably the polar tilt towards the bottommost hexagonal ring increases the bonding to the substrate. Similarly, the polar tilt towards the bottommost pentagon in the case of C_{60} on Cu(110) has been interpreted to result in a better-balanced C–Cu bond distance distribution which increases the bond strength with substrate atoms. Apparently the slight difference between the lattice constants of Cu(110) and Pd(110) (3.61 Å compared to 3.89 Å) is the decisive factor for tilting towards the bottommost pentagon and hexagon, respectively. In the case of the C_{60} monolayer on Cu(110) the azimuthal rotation has been assigned to a maximization of intermolecular C–C distances [169]. However, with the present system we find exactly the same azimuthal rotation for the metastable C_{60} molecules at low coverage. C_{60} on Pd(110) is immobile at room-temperature (cf. Section 7.1) and no close-packed layer is formed (cluster formation is observed but the intermolecular distances within the clusters are ~12 Å, much larger than in the close-packed layer.). Therefore the same strength of molecular reorientation in the different phases cannot be explained with the tendency to optimize intermolecular distances, but seems to be related to the details of the bonding interaction with the substrate.

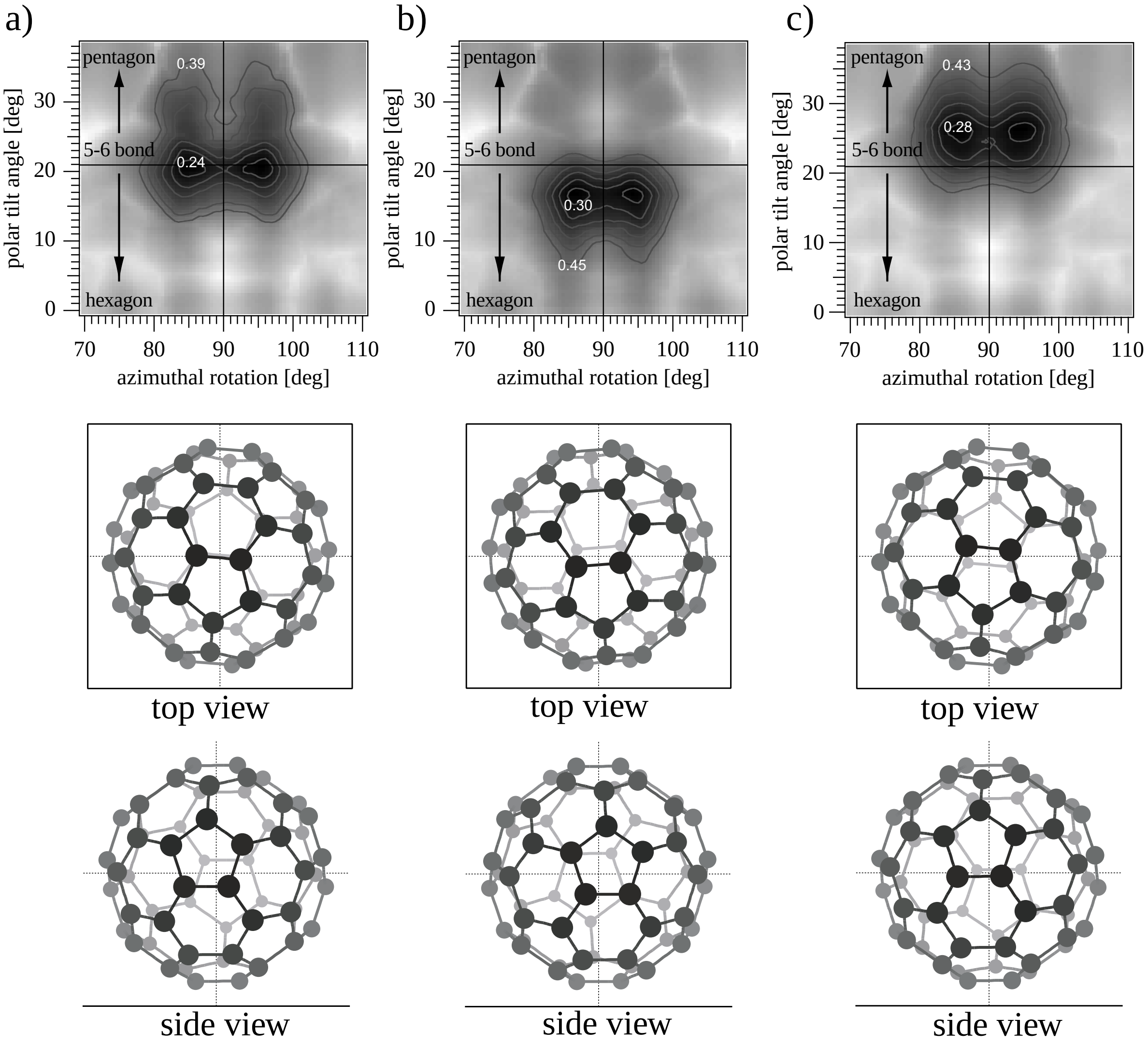

Figure 7.20: Comparison of R-factor plots obtained by azimuthal rotation and polar tilt of the C_{60} molecules away from symmetric 5-6 orientation and corresponding molecular orientations of **(a)** $\begin{pmatrix} 7 & -1 \\ \mp 2 & \pm 5 \end{pmatrix}$-structure (molecular orientation identical to (4 × 8)-structure) and **(b)** room-temperature deposited metastable C_{60} on Pd(110), **(c)** monolayer C_{60} on Cu(110) annealed to 720 K (Figure from Ref. [169].). The symmetric 5-6 bond corresponds to $\theta = 20.9°$ and $\phi = 90°$.

In conclusion three highly ordered phases consisting of alternating dark and bright C_{60} rows are found on the Pd(110) surface. The saturated monolayer with a $\begin{pmatrix} 7 & -1 \\ \mp 2 & \pm 5 \end{pmatrix}$-unit cell consists of two domains rotated by ±22.0° with respect to the close-packed Pd rows. C_{60} arranges in a quasihexagonal overlayer which is slightly expanded (1%) with respect to the van der Waals bound solid C_{60} close-packed plane. A rectangular (4×5)-structure evolves after partial desorption of C_{60}. Alternating dark and bright rows are aligned along $[1\bar{1}0]$, the direction of close-packed Pd-rows. At lower coverage the single-domain triple-stripe phase maintains the hexagonal C_{60} bulk structure only locally and forms a rectangular (4×8)-structure. The XPD analysis reveals that the C_{60} molecules in the highly ordered phases are identically oriented. They are facing with a 5-6 bond to the surface, which is slightly rotated away from the $[1\bar{1}0]$ high symmetry direction. Their different height in STM is attributed to Pd surface reconstructions. Whereas the C_{60} molecules of the bright molecular rows are adsorbed in *one* layer deep vacancies, the dark molecular rows are formed of C_{60} adsorbed in *two* layer deep vacancies. Room-temperature deposited C_{60} molecules adsorb on top of the unreconstructed surface. They are also facing with a 5-6 bond to the surface which is slightly rotated away from $[1\bar{1}0]$. Furthermore they are tilted by 5° towards the bottommost hexagonal ring of the C_{60} cage.

Chapter 8

Outlook

The present thesis deals with the behavior of large organic molecules at well-defined metal surfaces under ultrahigh-vacuum conditions. Their surface diffusion is characterized at the atomic scale and their bonding geometries, reflecting the interaction of molecular subunits with the substrate lattice, are directly determined. The nature of supramolecular self-assembly in two dimensions is elucidated. It is governed by the subtle balance between intermolecular and molecule-surface interactions, which can be tuned via the appropriate choice of substrate material and symmetry. Employing specifically designed molecular building blocks well-ordered superstructures, e.g., a one-dimensional supramolecular nanograting, can be fabricated. Our work represents a step towards supramolecular engineering at surfaces, where the self-assembly of properly designed molecules via noncovalent bonding is believed to open novel avenues for the deliberate positioning of nanometer functional units in supramolecular architectures. In supramolecular chemistry a multitude of building blocks is employed generating intricate assemblies in three dimensions, which represents an enormous fund for this objective.

Synergetic cooperations between surface scientists, organic chemists and theoreticians are indispensable in this interdisciplinary field of research. *Ab initio* calculations and molecular dynamics simulations elucidating the energetics and nature of noncovalent bonding at metal surfaces will provide valuable input for the design of novel materials. Mandatory close cooperations with organic chemistry and theory groups have been established during this thesis and will be continued. The long term vision is to formulate a comprehensive rationale for supramolecular design at surfaces.

For future applications, not only structural aspects but also the functionality of supramolecular nanostructures and films need to be addressed, e.g., optical properties or electrical transport through molecular wires. Studies employing semiconductor or dielectric substrates will be thus of great interest. The electronic, magnetic and optical behavior is not only determined by the properties of the single molecular building block, rather it strongly depends on the supramolecular assembly. By correlating structure and functionality, principles of supramolecular engineering for molecular electronics might be extracted.

For structure analysis scanning tunneling microscopy has been proven to be an eminently powerful tool. In order to complement the local topographic data, it is furthermore desirable to obtain chemical information of the systems under consideration. Wilson Ho and coworkers have recently succeeded in probing *single bonds* within a molecule by scanning tunneling inelastic spectroscopy (STIS) [197–199]. The results suggest that by application of STIS to large molecules and supramolecular assemblies local aspects in the underlying chemistry can be elucidated at the atomic scale. A high stability low-temperature STM especially dedicated to the study of large organic molecules is currently under construction in the group.

Appendix A

PVBA structure from DFT-calculations

Molecular geometry and point charges used for MD-simulations of PVBA species α as determined by DFT-calculations:

element	x $[a_0]^*$	y $[a_0]^*$	charge [e]
C_1	2.55863285	0.07223374	0.46664152
C_2	3.73386455	-2.46573234	0.28227913
C_3	6.38852167	-2.63777161	-0.33504617
C_4	7.55734682	-4.98020935	-0.10210907
C_5	6.11205626	-7.22641134	0.24239951
C_6	7.23367071	-9.72890854	-0.12448767
C_7	9.73262978	-10.24199390	-0.56814218
C_8	10.83666706	-12.75343609	1.07925701
C_9	13.48064518	-13.00665665	-0.89851308
C_{10}	14.55354309	-15.41131401	0.61201614
C_{11}	10.65213680	-17.31157112	0.61735374
C_{12}	9.40645218	-14.99929428	-0.90744263
C_{13}	3.45606589	-7.02636385	-0.20160571
C_{14}	2.27526593	-4.68157816	-0.30118266
N	13.19570923	-17.56839752	-0.75716686
O_1	-0.06165131	-0.03073225	-0.55587190
O_2	3.69501686	2.09774613	-0.48241568
H_1	7.34882164	-14.96071053	0.25806984
H_2	9.57366753	-19.07150650	0.01894831
H_3	16.60559082	-15.63619804	0.02093417
H_4	14.68147087	-11.33120823	0.24371213
H_5	11.09134960	-8.68871403	0.19484957
H_6	5.88480616	-11.29130936	0.11195221
H_7	0.22438364	-4.54802942	0.19950525
H_8	2.32255292	-8.74781990	0.14838950
H_9	9.61273670	-5.07250357	0.13246705
H_{10}	7.48797941	-0.89810860	0.18907151
H_{11}	-0.60413080	1.76486421	0.41613695

* a_0 Bohr radius, $a_0 = 0.529$ Å

Molecular geometry and point charges used for MD-simulations of PVBA species β as determined by DFT-calculations:

element	x [a_0]*	y [a_0]*	charge [e]
C_1	2.31499028	0.04788345	0.46280414
C_2	3.74334693	2.45080733	0.27981409
C_3	6.39458847	2.62008667	-0.39188507
C_4	7.55672741	4.97297287	-0.05643609
C_5	6.11432886	7.21889544	0.23646568
C_6	7.23713875	9.72395706	-0.09243020
C_7	9.73587799	10.24427414	-0.61976755
C_8	10.84177589	12.75764084	1.11158001
C_9	13.48646641	13.01494217	-0.90354478
C_{10}	14.55864811	15.42072201	0.61282623
C_{11}	10.65766239	17.31816864	0.61293107
C_{12}	9.41294098	15.00479507	-0.91746521
C_{13}	3.45604777	7.01588440	-0.25584918
C_{14}	2.28762150	4.67158508	-0.23407902
N	13.20075130	17.57858849	-0.75929034
O_1	3.78669763	-2.12172532	-0.53519726
O_2	-0.00660040	-0.03486985	-0.49544621
H_1	7.35519457	14.96593761	0.25792685
H_2	9.57669449	19.07675934	0.02083744
H_3	16.61063385	15.64553642	0.02163664
H_4	14.69005966	11.34147453	0.24524936
H_5	11.09686089	8.69264793	0.20435363
H_6	5.88496256	11.28387833	0.11197724
H_7	0.23851095	4.49695539	0.18296726
H_8	2.31795454	8.73437595	0.15887704
H_9	9.61215878	5.06729317	0.12133868
H_{10}	7.52582121	0.90201515	0.20628536
H_{11}	2.55030727	-3.53312659	0.41352022

* a_0 Bohr radius, $a_0 = 0.529$ Å

Appendix B

PEBA structure

Molecular geometry of PEBA as simulated with AM1, implemented in the MOPAC program packet Cerius 2, BIOSYM/Molecular Simulations:

element	x [Å]	y [Å]	z [Å]
C_1	0.6861	-0.0182	-0.0030
C_2	-0.7201	-0.0091	-0.0053
C_3	1.3848	-1.2386	0.0004
C_4	2.7758	-1.2432	0.0007
C_5	3.4832	-0.0328	0.0006
C_6	2.7929	1.1844	-0.0018
C_7	1.4011	1.1926	-0.0054
C_8	-5.4615	-1.1339	-0.0073
C_9	-4.0570	-1.1999	-0.0035
C_{10}	-3.3230	-0.0030	0.0033
C_{11}	-1.9179	-0.0117	0.0020
C_{12}	-4.0346	1.2115	0.0082
C_{13}	-5.4370	1.1649	0.0069
C_{14}	4.9496	-0.0758	0.0019
N	-6.1508	0.0214	-0.0012
O_1	5.6934	-1.0634	0.0101
O_2	5.5658	1.1440	-0.0069
H_1	0.8296	-2.1890	0.0023
H_2	3.3341	-2.1948	0.0020
H_3	3.3550	2.1328	-0.0030
H_4	0.8615	2.1512	-0.0120
H_5	-6.0700	-2.0563	-0.0130
H_6	-3.5460	-2.1715	-0.0066
H_7	-3.5070	2.1738	0.0131
H_8	-6.0294	2.0967	0.0140
H_9	6.6295	1.0156	-0.0052

Bibliography

[1] M. Schulz, Nature **399**, 729 (1999).

[2] D. A. Muller, T. Sorsch, S. Moccio, F. H. Baumann, K. Evans-Lutterodt, and G. Timp, Nature **399**, 758 (1999).

[3] *Molecular Electronics*, *Chemistry for the 21st Century*, edited by J. Jortner and M. Ratner (Blackwell, Oxford, 1997).

[4] A. Aviram and M. A. Ratner, Chemical Physics Letters **29**, 277 (1974).

[5] S. J. Tans, R. M. Verschueren, and C. Dekker, Nature **393**, 49 (1998).

[6] R. Martel, T. Schmidt, H. R. Shea, T. Hertel, and P. Avouris, Applied Physics Letters **73**, 2447 (1998).

[7] S. J. Tans, M. H. Devoret, H. Dai, A. Thess, R. E. Smalley, L. J. Geerligs, and C. Dekker, Nature **386**, 474 (1997).

[8] H.-W. Fink and C. Schönenberger, Nature **398**, 407 (1999).

[9] J.-M. Lehn, Science **227**, 849 (1985).

[10] F. Vögtle, *Supramolecular Chemistry* (Wiley, New York, 1991), Vol. 227.

[11] J.-M. Lehn, *Supramolecular Chemistry* (VCH, Weinheim, 1995), Vol. 227.

[12] *Comprehensive Supramolecular Chemistry*, edited by J. L. Atwood, J. E. D. Davies, D. D. MacNicol, F. Vögtle, and J.-M. Lehn (Pergamon, New York, 1996).

[13] G. A. Jeffrey and W. Saenger, *Hydrogen bonding in biological systems* (Springer, Berlin, 1991).

[14] J.-M. Lehn, Angewandte Chemie Int. Ed. **102**, 1347 (1990).

[15] G. M. Whitesides, J. P. Mathias, and C. T. Seto, Science **154**, 1312 (1991).

[16] J. S. Lindsey, New Journal of Chemistry **15**, 153 (1991).

[17] D. Philp and J. F. Stoddart, Angewandte Chemie Int. Ed. **35**, 1154 (1996).

[18] J. R. Fredericks and A. D. Hamilton, in *Comprehensive Supramolecular Chemistry vol. 9*, edited by J. L. Atwood, J. E. D. Davies, D. D. MacNicol, and J.-M. Lehn (Pergamon, New York, 1996), Vol. 9, pp. 565–594.

[19] J. Veciana, J. Cirujeda, C. Rovira, E. Molins, and J. J. Novoa, J. Phys. I France **6**, 1967 (1996).

[20] S. C. Zimmermann, F. Zeng, D. E. C. Reichert, and S. V. Kolutchin, Science **271**, 1095 (1996).

[21] R. P. Sijbesma, F. H. Beijer, L. Brunsveld, B. J. B. Folmer, J. H. K. K. Hirschberg, R. F. M. Lange, J. K. L. Lowe, and E. W. Meijer, Science **278**, 1601 (1997).

[22] K. A. Jolliffe, P. Timmermann, and D. N. Reinhoudt, Angewandte Chemie Int. Ed. **38**, 933 (1999).

[23] T. Kawai, H. Tanaka, and T. Nakagawa, Surface Science **386**, 124 (1997).

[24] J. K. Gimzewski and C. Joachim, Science **283**, 1683 (1999).

[25] M. Böhringer, K. Morgenstern, W.-D. Schneider, R. Berndt, F. Mauri, A. De Vita, and R. Car, Physical Review Letters **83**, 324 (1999).

[26] P. Samori, V. Francke, K. Müllen, and J. P. Rabe, Chemistry - A European Journal **5**, 2312 (1999).

[27] S. Chiang, in *Scanning Tunneling Microscopy I*, edited by H.-J. Güntherodt and R. Wiesendanger (Springer, New York, 1992), p. 181.

[28] *Growth and Properties of Ultrathin Epitaxial Layers*, edited by D. A. King and D. P. Woodruff (Elsevier, Amsterdam, 1997).

[29] H. Ohtani, R. J. Wilson, S. Chiang, and C. M. Mate, Physical Review Letters **60**, 2398 (1988).

[30] J. K. Gimzewski, E. Stoll, and R. R. Schlittler, Surface Science **181**, 267 (1987).

[31] P. H. Lippel, R. J. Wilson, M. D. Miller, Ch. Wöll, and S. Chiang, Physical Review Letters **62**, 171 (1989).

[32] E. Umbach, M. Sokolowski, and R. Fink, Applied Physics A **63**, 565 (1996).

[33] S. R. Forrest, Chemical Reviews **97**, 1793 (1997).

[34] C. Seidel, A. Soukopp, R. Li, P. Bäuerle, and E. Umbach, Surface Science **374**, 17 (1997).

[35] M. T. Cuberes, R. R. Schlittler, T. A. Jung, K. Schaumburg, and J. K. Gimzewski, Surface Science **383**, 37 (1997).

[36] E. Umbach, K. Glöckler, and M. Sokolowski, Surface Science **402-4**, 20 (1998).

[37] K. Glöckler, C. Seidel, A. Soukopp, M. Sokolowski, E. Umbach, M. Böhringer, R. Berndt, and W.-D. Schneider, Surface Science **405**, 1 (1998).

[38] C. Cai *et al.*, Advanced Materials **11**, 745 (1999).

[39] B. Müller, C. Cai, M. M. Bösch, M. Jäger, C. Bosshard, P. Günter, J. V. Barth, J. Weckesser, and K. Kern, Thin Solid Films **343-344**, 165 (1999).

[40] Y. Wang, Nature **356**, 585 (1992).

[41] *Progress in Fullerene Research, International Winterschool on Electronic Properties of Novel Materials*, edited by H. Kuzmany, J. Fink, M. Mehring, and S. Roth (World Scientific, Singapore, 1994).

[42] C. J. Chen, *Introduction to Scanning Tunneling Microscopy*, . (Oxford University Press, New York, 1993).

[43] G. Binnig, H. Rohrer, C. Gerber, and E. Weibel, Physical Review Letters **49**, 57 (1982).

[44] G. Binnig and H. Rohrer, Helvetica Physica Acta **55**, 726 (1982).

[45] J. Bardeen, Physical Review Letters **6**, 57 (1961).

[46] E. L. Wolf, *Principles of Electron Tunneling Spectroscopy* (Oxford University Press, New York, 1985).

[47] J. Tersoff and D. R. Hamann, Physical Review Letters **50**, 1998 (1983).

[48] A. Selloni, P. Carnevali, E. Tosatti, and C. D. Chen, Physical Review B **31**, 2602 (1985).

[49] N. D. Lang, Physical Review B **34**, 5947 (1986).

[50] S. Park and R. C. Barrett, in *Scanning Tunneling Microscopy.*, edited by J. Stroscio and W. Kaiser (Academic Press, San Diego, 1993).

[51] T. Zambelli, J. V. Barth, J. Wintterlin, and G. Ertl, Nature **390**, 495 (1997).

[52] D. M. Eigler, P. S. Weiss, E. K. Schweizer, and N. D. Lang, Physical Review Letters **66**, 1189 (1991).

[53] N. D. Lang, Physical Review Letters **56**, 1164 (1986).

[54] N. D. Lang, Physical Review Letters **58**, 45 (1987).

[55] C. J. Chen, Journal of Vacuum Science & Technology A **9**, 44 (1991).

[56] M. Tsukada, K. Kobayashi, N. Isshiki, H. Kageshima, T. Uchiyama, S. Watanabe, and T. Schimizu, Surface Science Reports **13**, 265 (1991).

[57] M. Tsukada, H. Kageshima, N. Isshiki, and K. Kobayashi, Surface Science **266**, 253 (1992).

[58] G. Doyen, D. Drakova, J. V. Barth, R. Schuster, T. Gritsch, R. J. Behm, and G. Ertl, Physical Review B **48**, 1738 (1993).

[59] P. Sautet and C. Joachim, Physical Review B **38**, 12238 (1988).

[60] J. A. Stroscio and D. M. Eigler, Science **254**, 1319 (1991).

[61] P. Zeppenfeld, C. P. Lutz, and D. M. Eigler, Ultramicroscopy **42-44**, 128 (1992).

[62] M.-L. Bocquet and P. Sautet, Surface Science **360**, 128 (1996).

[63] R. F. Lin, G. S. Blackmann, M. A. V. Hove, and G. A. Samorjai, ACTA Crystallographica B **43**, 368 (1987).

[64] P. Sautet and C. Joachim, Chemical Physics Letters **185**, 23 (1991).

[65] P. Sautet, Chemical Reviews **97**, 1097 (1997).

[66] S. Hüfner, *Photoelectron Spectroscopy* (Springer, Berlin, 1995).

[67] K. Siegbahn, U. Gelius, H. Siegbahn, and E. Olson, Physics Letters A **32A**, 221 (1970).

[68] C. S. Fadley and S. Å. L. Bergström, Physics Letters A **35A**, 375 (1971).

[69] A. Liebsch, Physical Review Letters **32**, 1203 (1974).

[70] S. Kono, C. S. Fadley, N. F. T. Hall, and Z. Hussain, Physical Review Letters **41**, 117 (1978).

[71] D. Woodruff, D. Norman, B. W. Holland, N. V. Smith, H. H. Farrell, and M. M. Traum, Physical Review Letters **41**, 1130 (1978).

[72] R. Fasel, Ph.D. thesis, Universität Freiburg (Schweiz), 1996.

[73] P. A. Lee, Physical Review B **13**, 5261 (1976).

[74] J. Mustre de Leon, J. J. Rehr, C. R. Natoli, C. S. Fadley, and J. Osterwalder, Physical Review B **39**, 5632 (1989).

[75] J. Osterwalder, P. Aebi, R. Fasel, D. Naumovic, P. Schwaller, T. Kreutz, L. Schlapbach, T. Abukawa, and S. Kono, Surface Science **331-333**, 1002 (1995).

[76] *Angle-resolved photoemission*, edited by S. D. Kevan (Elsevier, Amsterdam, 1992).

[77] H. Brune, H. Röder, K. Bromann, and K. Kern, Thin Solid Films **264**, 230 (1995).

[78] B. Fischer, Ph.D. thesis, EPF Lausanne, 1998.

[79] A. Hirstein, Ph.D. thesis, EPF Lausanne, 1998.

[80] L. Bürgi, Ph.D. thesis, EPF Lausanne, 1999.

[81] C. Cai, M. Bösch, Y. Tao, B. Müller, Z. Gan, A. Kündig, C. Bosshard, I. Liakatas, M. Jäger, and P. Günter, Journal of the Chemical Society **120**, 8563 (1998).

[82] B. Müller, M. Jäger, Y. Tao, A. Kündig, C. Cai, C. Bosshard, and P. Günter, Optical Materials **12**, 345 (1999).

[83] *Atomic and Molecular Wires, NATO Advanced Research Series*, edited by C. Joachim and S. Roth (Kluwer, Dordrecht, 1997).

[84] D. Cohen and Y. Zeiri, J. Chem. Phys **97**, 1531 (1992).

[85] M. Silverberg, J. Chem. Phys **99**, 9255 (1993).

[86] D. Huang, Y. Chen, and K. A. Fichthorn, J. Chem. Phys **101**, 11021 (1994).

[87] J. S. Raut and K. A. Fichthorn, J. Chem. Phys **108**, 1626 (1998).

[88] J. L. Brand, M. V. Arena, A. A. Deckert, and S. M. George, Journal of Chemical Physics **92**, 5136 (1990).

[89] J. Yoshinubo, H. Tanaka, T. Kawai, and M. Kawai, Physical Review B **53**, 7492 (1996).

[90] M. Doering, H.-P. Rust, B. G. Briner, and A. M. Bradshaw, Surface Science **410**, L736 (1998).

[91] A. Ikai, Surface Science Reports **26**, 261 (1996).

[92] F. P. Netzer, G. Rangelov, and G. Rosina, Journal of Chemical Physics **89**, 3331 (1988).

[93] J. Stöhr, *NEXAFS Spectroscopy*, Vol. 25 of *Springer Series in Surface Sciences* (Springer, Heidelberg, 1991).

[94] *Comprehensive organometallic chemistry II : a review of the literature 1982-1994*, edited by E. W. Abel, F. G. A. Stone, and G. Wilkinson (Pergamon, New York, 1995).

[95] R. I. Masel, *Principles of Adsorption and Reaction on Solid Surfaces*, *Wiley Series in chemical engineering* (John Wiley & Sons, New York, 1996).

[96] J. L. Morrison and J. K. Roberts, Proceedings of the Royal Society of London **A173**, 13 (1939).

[97] M. A. Morris, M. Bowker, and D. A. King, in *Simple Processes at the Gas-Solid Interface*, Vol. 19 of *Comprehensive Chemical Kinetics*, edited by C. H. Bamford, C. F. H. Tipper, and R. G. Compton (Elsevier, Amsterdam, 1984), p. 1.

[98] C. R. Arumainayagam and R. J. Madix, Progress in Surface Science **38**, 1 (1991).

[99] E. Kampshoff, N. Waelchli, A. Menck, and K. Kern, Surface Science **360**, 55 (1996).

[100] J. V. Barth, T. Zambelli, J. Wintterlin, R. Schuster, and G. Ertl, Physical Review B **55**, 12902 (1997).

[101] B. G. Briner, M. Döring, K. Rust, and A. M. Bradshaw, Science **278**, 257 (1997).

[102] J. V. Barth, Surface Science Reports in press (2000).

[103] M. Fujisawa, T. Sekitani, Y. Morikawa, and M. Nishijima, Journal of Physical Chemistry **95**, 7415 (1991).

[104] G. Witte, H. Range, J. P. Toennies, and Ch. Wöll, Journal of Electron Spectroscopy and Related Phenomena **64/65**, 715 (1993).

[105] L. J. Lauhon and W. Ho, Journal of Chemical Physics **111**, 5633 (1999).

[106] A. Soukopp, K. Glöckler, P. Kraft, S. Schmitt, M. Sokolowski, E. Umbach, E. Mena-Osteritz, P. Bäuerle, and E. Hädicke, Physical Review B **58**, 13882 (1998).

[107] L. Bürgi, O. Jeandupeux, A. Hirstein, H. Brune, and K. Kern, Physical Review Letters **81**, 5370 (1998).

[108] O. Jeandupeux, L. Bürgi, A. Hirstein, H. Brune, and K. Kern, Physical Review B **59**, 15926 (1999).

[109] G. A. Jeffrey, in *Landolt-Börnstein Series VII:1b*, edited by W. Saenger (Springer, Berlin, 1989), pp. 277 – 348.

[110] F. Takusagawa and A. Shimada, ACTA Crystallographica **B32**, 1925 (1976).

[111] G. A. Jeffrey, *An Introduction to Hydrogen Bonding* (Oxford Univ. Press, New York, 1997).

[112] G. R. Desiraju, Accounts of Chemical Research **29**, 441 (1996).

[113] J. V. Barth, H. Brune, R. J. Behm, and G. Ertl, Physical Review B **42**, 9307 (1990).

[114] K. Kern, H. Niehus, A. Schatz, P. Zeppenfeld, J. George, and G. Comsa, Physical Review Letters **67**, 855 (1991).

[115] D. Vanderbilt, Surface Science **268**, L300 (1992).

[116] D. Vanderbilt, in *Computations for the Nanoscale*, edited by P. Blöchl (Kluwer, Amsterdam, 1993), pp. 1–11.

[117] V. I. Marchenko, JETP Lett. **33**, 381 (1981).

[118] O. L. Alerhand, D. Vanderbilt, R. D. Meade, and J. D. Joannopoulos, Physical Review Letters **61**, 1973 (1988).

[119] O. L. Alerhand, D. Vanderbilt, R. D. Meade, and J. D. Joannopoulos, Physical Review Letters **62**, 166 (1989).

[120] D. Vanderbilt, O. L. Alerhand, R. D. Meade, and J. D. Joannopoulos, Journal of Vacuum Science and Technology B **7**, 1013 (1989).

[121] B. G. Briner, Physikalische Blätter **5**, 419 (1998).

[122] R. S. Cox and D. E. Williams, Journal of Computational Chemistry **2**, 304 (1981).

[123] A. J. Stone, A. D. Buckingham, and P. W. Fowler, Journal of Chemical Physics **107**, 1030 (1997).

[124] L. Pasteur, C.R. Hebd. Seances Acad. Sci **26**, 535 (1848).

[125] M. Böhringer, K. Morgenstern, W.-D. Schneider, and R. Berndt, Angewandte Chemie Int. Ed. **38**, 821 (1999).

[126] M. V. Stewart and E. M. Arnett, in *Topics in Stereochemistry*, edited by N. Allinger, E. Eliel, and S. Wilen (Wiley, New York, 1982), pp. 195–262.

[127] R. N. Weis and H. M. McConnell, Nature **310**, 47 (1984).

[128] C. J. Eckhardt, N. M. Peachey, D. R. Swanson, J. M. Takacs, M. A. Khan, X. Gong, J. H. Kim, J. Wang, and R. A. Uphaus, Nature **362**, 614 (1993).

[129] P. Nassoy, M. Goldmann, O. Bouloussa, and F. Rondelez, Physical Review Letters **75**, 457 (1995).

[130] F. Stevens, D. J. Dyer, and D. M. Walba, Angewandte Chemie Int. Ed. **35**, 900 (1996).

[131] S. De Feyter, P. C. M. Grim, M. Rücker, P. Vanoppen, C. Meiners, M. Sieffert, S. Valiyaveettil, K. Müllen, and F. C. de Schryver, Angewandte Chemie Int. Ed. **37**, 1223 (1998).

[132] M. Böhringer, W.-D. Schneider, and R. Berndt, Angewandte Chemie Int. Ed. **39**, 792 (2000).

[133] D. Marx, M. E. Tuckerman, J. Hutter, and M. Parrinello, Nature **397**, 601 (1999).

[134] M. Ortega Lorenzo, C. J. Baddeley, C. Muryn, and R. Raval, Nature **404**, 376 (2000).

[135] J. A. Stroscio, D. T. Pierce, R. A. Dragoset, and P. N. First, Journal of Vacuum Science and Technology A **10**, 1981 (1992).

[136] B. Voigtländer, G. Meyer, and N. M. Amer, Physical Review B **44**, 10354 (1991).

[137] J. Wollschläger and N. M. Amer, Surface Science **277**, 1 (1992).

[138] D. D. Chambliss, R. J. Wilson, and S. Chiang, Journal of Vacuum Science and Technology **9**, 933 (1991).

[139] D. D. Chambliss, R. J. Wilson, and S. Chiang, Physical Review Letters **66**, 1721 (1991).

[140] J. A. Meyer, I. D. Baikie, E. Kopatzki, and R. J. Behm, Surface Science **365**, L647 (1996).

[141] M. Böhringer, K. Morgenstern, W.-D. Schneider, M. Wühn, Ch. Wöll, and R. Berndt, Surface Science **444**, 199 (2000).

[142] H. Brune and K. Kern, in *Growth and Properties of Ultrathin Epitaxial Layers*, edited by D. A. King and D. P. Woodruff (Elsevier, Amsterdam, 1997), Vol. 8, p. 149.

[143] H. Brune, M. Giovannini, K. Bromann, and K. Kern, Nature **394**, 451 (1998).

[144] H. Brune, Surface Science Reports **31**, 121 (1998).

[145] H. Brune, H. Röder, K. Bromann, K. Kern, J. Jacobsen, P. Stoltze, K. Jacobsen, and J. Nørskov, Surface Science **349**, L115 (1996).

[146] M. Hohage, M. Bott, M. Morgenstern, Z. Zhang, T. Michely, and G. Comsa, Physical Review Letters **76**, 2366 (1996).

[147] B. G. Frederick, F. M. Leibsle, S. Haq, and N. V. Richardson, Surface Review and Letters **3**, 1523 (1996).

[148] C. C. Perry, S. Haq, B. G. Frederick, and N. V. Richardson, Surface Science **409**, 512 (1998).

[149] M. Giesen, Surface Science **442**, 543 (1999).

[150] H. Röder, E. Hahn, H. Brune, J.-P. Bucher, and K. Kern, Nature **366**, 141 (1993).

[151] K. Morgenstern, G. Rosenfeld, and G. Comsa, Physical Review Letters **76**, 2113 (1996).

[152] W. Theis, N. C. Bartelt, and R. M. Tromp, Physical Review Letters **75**, 3328 (1995).

[153] R. Smoluchowski, Physical Review **60**, 661 (1941).

[154] P. Avouris, I.-W. Lyo, and P. Molinas-Mata, Chemical Physics Letters **240**, 423 (1995).

[155] M. M. Kamna, T. M. Graham, J. C. Love, and P. S. Weiss, Surface Science **419**, 12.23 (1998).

[156] S. J. Sowerby, W. M. Heckl, and G. B. Petersen, Journal of Molecular Evolution **43**, 419 (1996).

[157] R. Viswanathan, J. A. Zasadzinski, and D. K. Schwartz, Nature **368**, 440 (1994).

[158] F. Charra and J. Cousty, Physical Review Letters **80**, 1682 (1998).

[159] R. C. Haddon, L. E. Brus, and K. Raghavacchari, Chemical Physics Letters **125**, 459 (1986).

[160] H. W. Kroto, J. R. Heath, S. C. O'Brien, R. F. Curl, and R. E. Sunally, Nature **318**, 162 (1985).

[161] W. Krätschmer, L. D. Lamb, K. Fostiropoulos, and D. R. Huffman, Nature. **347**, 354 (1990).

[162] G. Gensterblum *et al.*, Physical Review B **50**, 11981 (1994).

[163] A. V. Hamza and M. Balooch, Chemical Physics Letters **201**, 404 (1993).

[164] P. A. Brühwiler, A. J. Maxwell, P. Baltzer, S. Andersson, D. Arvanitis, L. Karlsson, and N. Martensson, Chemical Physics Letters **279**, 85 (1997).

[165] A. J. Maxwell, P. A. Brühwiler, S. Andersson, N. Martensson, and P. Rudolf, Chemical Physics Letters **247**, 257 (1995).

[166] R. Fasel, P. Aebi, R. G. Agostino, D. Naumovic, J. Osterwalder, A. Santaniello, and L. Schlapbach, Physical Review Letters **76**, 4733 (1996).

[167] M. Ø. Pedersen, P. W. Murray, E. Laegsgaard, I. Stensgaard, and F. Besenbacher, Surface Science **389**, 300 (1997).

[168] P. W. Murray, M. Ø. Pedersen, E. Laegsgaard, I. Stensgaard, and F. Besenbacher, Physical Review B **55**, 9360 (1997).

[169] R. Fasel, R. G. Agostino, P. Aebi, and L. Schlapbach, Physical Review B **60**, 4517 (1999).

[170] M. T. Cuberes, R. R. Schlittler, and J. K. Gimzewski, Applied Physics A **66**, 669 (1998).

[171] M. R. C. Hunt, S. Modesti, P. Rudolf, and R. E. Palmer, Physical Review B **51**, 10039 (1995).

[172] C. Cepek, A. Goldoni, and S. Modesti, Physical Review B **53**, 7466 (1996).

[173] M. Pedio, K. Hevesi, N. Zema, M. Capozi, P. Perfetti, R. Gouttebaron, J. J. Pireaux, R. Caudano, and P. Rudolf, Surface Science **437**, 249 (1999).

[174] E. I. Altman and R. J. Colton, Physical Review B **48**, 18244 (1993).

[175] T. David, J. K. Gimzewski, D. Purdie, L. B. Reihl, and R. R. Schlittler, Physical Review B **50**, 5810 (1994).

[176] J. K. Gimzewski, S. Modesti, and R. R. Schlittler, Physical Review Letters **72**, 1036 (1994).

[177] E. I. Altman and R. J. Colton, Surface Science **279**, 49 (1992).

[178] M. K.-J. Johansson, A. J. Maxwell, S. M. Gray, P. A. Brühwiler, D. C. Mancini, L. S. O. Johansson, and N. Mårtensson, Physical Review B **54**, 13472 (1996).

[179] P. Rudolf, *Proceedings of the International Winterschool on Electronic Properties of Novel Materials. Fullerenes and Fullerene Nanostructures* (World Scientific, Singapore, 1996), pp. 263–75.

[180] L. H. Tjeng, R. Hesper, A. C. L. Heessels, A. Heeres, H. T. Jonkman, and G. A. Sawatzky, Solid State Communications **103**, 31 (1997).

[181] M. R. Sørensen, K. W. Jacobsen, and H. Jónsson, Physical Review Letters **77**, 5067 (1996).

[182] R. Schuster, J. V. Barth, G. Ertl, and R. J. Behm, Surface Science **247**, L229 (1991).

[183] J. V. Barth, T. Zambelli, J. Wintterlin, and G. Ertl, in preparation .

[184] R. J. Behm, in *Physics and Chemistry of Alkali Metal Adsorption*, edited by H. Bonzel, A. Bradshaw, and G. Ertl (Elsevier, Amsterdam, 1989), pp. 111–28.

[185] X. Yao, R. K. Workman, C. A. Peterson, D. Chen, and D. Sarid, Applied Physics A **66**, 107 (1998).

[186] M. R. C. Hunt, P. Rudolf, and S. Modesti, Physical Review B **55**, 7889 (1997).

[187] E. Giudice, E. Magnano, S. Rusponi, C. Boragno, and U. Valbusa, Surface Science **405**, L561 (1998).

[188] G. Witte and Ch. Wöll, Journal of Chemical Physics **103**, 5860 (1995).

[189] K. Weiss, J. Weckesser, and Ch. Wöll, Journal of Molecular Structure (Theochem) **458**, 143 (1999).

[190] P. A. Heiney, J. E. Fischer, A. R. McGhie, W. J. Romanow, A. M. Denenstein, J. P. McCauley Jr., A. B. Smith, and D. E. Cox, Physical Review Letters **66**, 2911 (1991).

[191] Y. Kuk, D. K. Kim, Y. D. Suh, K. H. Park, H. P. Noh, S. J. Oh, and S. K. Kim, Physical Review Letters **70**, 1948 (1993).

[192] T. Hashizume *et al.*, Physical Review Letters **71**, 2959 (1993).

[193] J. K. Gimzewski, S. Modesti, C. Gerber, and R. R. Schlittler, Chemical Physics Letters **213**, 401 (1993).

[194] K. Yagi, K. Higashiyama, S. Yamazaki, H. Yanashima, H. Ohnuki, H. Fukutani, and H. Kato, Surface Science **231**, 397 (1990).

[195] J. G. Hou, Y. Jinlong, W. Haiqian, L. Qunxiang, Z. Changgan, L. Hai, B. Wang, D. M. Chen, and Z. Qingshi, Physical Review Letters **83**, 3001 (1999).

[196] R. Fasel, in preparation .

[197] B. C. Stipe, M. A. Rezai, and W. Ho, Science **280**, 1732 (1998).

[198] B. C. Stipe, M. A. Rezai, and W. Ho, Physical Review Letters **82**, 1724 (1999).

[199] J. Lee and W. Ho, Science **286**, 1719 (1999).

Acknowledgments

I thank Professor Klaus Kern, the director of my thesis, for giving me the opportunity to work in his group and for guiding me throughout the entire thesis.

I am especially grateful to Johannes Barth who supervised this work. He was involved in the planning, the realization to the analysis and interpretation of the experiments and has contributed a lot to the success of this thesis. His engagement and interest in innumerable discussions have been a major source of motivation for me. Furthermore his careful reading of the manuscript is gratefully acknowledged.

I want to thank Bjørn Fischer for introducing me into the business of scanning tunneling microscopy. Although being in the hectic final period of his thesis he spent a lot of time in explaining the mysteries of the experimental set-up.

The fruitful cooperation with Chengzhi Cai, now assistant professor at the university of Houston (Texas), who provided the PVBA and PEBA sample is gratefully acknowledged.

I would like to thank Alessandro De Vita of the Institut Romand de Recherche Numérique en Physique des Matériaux, who has carried out the computer simulations of chapter 4. Our intensive discussions have been very stimulating and greatly improved the understanding of the PVBA/Ag(111) system.

During this work I had the opportunity to perform XPD measurements in the group of Jürg Osterwalder at the university of Zürich. I want to thank Cinzia Cepek for her indispensable help in the laboratory, it was a pleasure to work with her. Furthermore I gratefully acknowledge Roman Fasel, *the* expert of XPD on C_{60}, for carrying out the SSC calculations presented in chapter 7. The enthusiasm of Thomas Greber has largely contributed to the success of the project.

I also want to thank the members of the jury: Prof. W.-D. Schneider, Prof. N.V. Richardson and Prof. H. Vogel for judging this thesis.

All people working at the Institut de Physique Expérimentale, both the scientific and the technical staff, I would like to thank. The atmosphere at the institute was always friendly and pleasant and the cooperation among each other very efficient. It has been

a pleasure to work here!

During my time in Lausanne I have not only found good colleagues at the IPE but some real friends. Unfortunately the time of a Ph.D. thesis is quite limited and so Lukas Bürgi and Hannes Kind, with whom I spent my spare time in the beginning of my thesis, already left Lausanne. In Dietrich Peterka, Renald Schaub and Nik Knorr I found new friends. I hope I will keep in touch with them all!

Mein ganz besonderer Dank gilt meiner Familie und meinen Freunden. Ihre Unterstützung ist einfach unbeschreiblich!

Curriculum vitae

Name:	Jens Weckesser
Date of Birth:	February 19, 1970
Nationality	German

1980–1989	High School at the Bunsen-Gymnasium in Heidelberg, Germany
1990–1996	Diploma studies in physics at the Ruprecht-Karls university, Heidelberg
March 1995–June 1996	Diploma thesis in the group of Prof M. Grunze under the supervision of Prof Ch. Wöll at the Institute of Physical Chemistry of the Ruprecht-Karls university in Heidelberg: "Röntgenabsorptionsspektroskopie an ultradünnen Schichten aus langkettigen Carbonsäuren"
August 1996–March 1997	Research assistant in the group of Prof J.P. Toennies at the Max-Planck Institut für Strömungsforschung in Göttingen, Germany
1997–2000	Research and teaching assistant in the group of Prof K. Kern at the Institute for Experimental Physics of the Swiss Federal Institute of Technology in Lausanne, Switzerland
2000	PhD thesis: "Atomic Scale Observations of Large Organic Molecules at Metal Surfaces: Bonding, Ordering and Supramolecular Self-Assembly"

Publications

J. Weckesser, D. Fuhrmann, K. Weiss, Ch. Wöll and N.V. Richardson, "Photoemission from long chain alkanes adsorbed on a metal surface and the electronic structure of trans-polyethylene (-CH2-)$_n$", Surface Review and Letters **4**, 209 (1997).

J. Braun, J. Weckesser, J. Ahner, D. Mocuta, J.T. Yates Jr., Ch. Wöll, "The frustrated translational mode of CO on Cu(110): Azimuthal anisotropy studied by helium atom scattering - A comparison with time-of-flight electron stimulated desorption of ion angular distribution measurements", J. Chem. Phys. **108**, 5161 (1998).

K. Weiss, J. Weckesser, Ch. Wöll, "An X-ray absorption study of hydrocarbons physisorbed on metal surfaces", J. of Molecular Structure (TheoChem) **458**, 143 (1999).

J. Weckesser, J.V. Barth and K. Kern, "Direct observation of surface diffusion of large organic molecules at metal surfaces : PVBA on Pd(110)", J. Chem. Phys. **110**, 5351 (1999).

B. Müller, Ch. Cai, M. Bösch, M. Jäger, Ch. Bosshard, P. Günter, J.V. Barth, J. Weckesser, and K. Kern, "Ordering of 4-trans-2-(pyrid-4-yl-vinyl) benzoic acid on amorphous SiO2 and Pd(110)", Proc. IVC 98, Thin Sol. Films **343-344**, 171 (1999).

C. Cai, J. Weckesser, J.V. Barth, B. Müller, Y. Tao, M.M. Bösch, Ch. Bosshard and P. Günter, "Growth mechanism and in plane directional order of organic thin films prepared by oblique organic molecular beam deposition" , Adv. Mat. **11**, 750 (1999).

J. Weckesser, J.V. Barth, Ch. Cai, B. Müller and K. Kern, "Binding and ordering of large organic molecules on an anisotropic metal surface: PVBA on Pd(110)", Surf. Sci. **431**, 168 (1999).

J.V. Barth, H. Brune, B. Fischer, J. Weckesser and K. Kern, “On the dynamics of surface diffusion in the weak corrugation limit”, Phys. Rev. Lett. **84**, 1732 (2000).

J.V. Barth, J. Weckesser, C. Cai, P. Günter, L. Bürgi, O. Jeandupeux, K. Kern, “Building supramolecular nanostructures at surfaces by hydrogen bonding”, Angew. Chem. Int. Ed. **39**, 1230 (2000).

C. Cai, M. Bösch, Ch. Bosshard , B. Müller, Y. Tao, A. Kündig, M. Kiy, I. Biaggio, I. Liakatas, P. Günter, J. Weckesser, J.V. Barth, L. Bürgi, O. Jeandupeux, K. Kern, “Self-assembly growth of organic thin films and nanostructures by molecular beam deposition. An interesting and unexpected story”, Anisotropic Materials - Approaches to Polar Order, Eds. R. Glaser and P. Kaszynski, ACS Symposium Series, in press (2000).